May 2021

Uncovering the Nonlinear Dynamics of Origami Folding

Sahand Sadeghi
Clemson University, sahand72@gmail.com

Uncovering the Nonlinear Dynamics of Origami Folding

A Dissertation
Presented to
the Graduate School of
Clemson University

In Partial Fulfillment
of the Requirements for the Degree
Doctor of Philosophy
Mechanical Engineering

by
Sahand Sadeghi
May 2021

Accepted by:
Dr. Suyi Li, Committee Chair
Dr. Ardalan Vahidi
Dr. Phanindra Tallapragada
Dr. Umesh Vaidya

Abstract

Origami, the ancient art of paper folding, has found lots of different applications in various branches of science, including engineering. However, most of the studies on engineering applications of origami have been limited to static or quasi-static applications. Origami folding, on the other hand, could be a dynamic process. The intricate nonlinear elastic properties of origami structures can lead to interesting dynamic characteristics and applications. Nevertheless, studying the dynamics of folding is still a nascent field. In this dissertation, we try to expand our knowledge of fundamentals of origami folding dynamics. We look at the problem of origami folding dynamics from two different perspectives: 1) How can we utilize folding-induced mechanical properties for dynamic applications? and 2) How can we fold origami structures using dynamic excitations? In order to answer these questions, we conduct three different projects. Regarding the first perpective, we study a unique asymmetric quasi-zero stiffness (QZS) property from the pressurized fluidic origami cellular structure, and examine the feasibility and efficiency of using this nonlinear property for low-frequency vibration isolation. In another project, we analyze the feasibility of utilizing origami folding techniques to create an optimized jumping mechanism. And finally, regarding the second perspective, we examine a rapid and reversible origami folding method by exploiting a combination of resonance excitation, asymmetric multi-stability, and active control. In addition to these studies, Witnessing the

rich and nonlinear dynamic characteristics of origami structures, in this dissertation we introduce the idea of using origami structures as physical reservoir computing systems and investigate their potentials in sensing and signal processing tasks without relying on external digital components and signal processing units.

Dedication

To my parents and my sister,

for all of their sacrifices and support.

Acknowledgements

I would first like to thank my advisor Dr. Suyi Li for his constant guidance and help throughout the projects. Dr. Li provided the necessary equipment, funding, and background knowledge in origami engineering to make these projects possible. He taught me how to approach a problem, think about the big picture and ask the right questions; skills that will be great assets in my future career as well.

I would also like to thank Dr. Phanindra Tallapragada. I had the chance to attend his courses on nonlinear dynamics, which encouraged me to learn more about this field. He also provided the inspiration for studying dynamics of jumping mechanisms that use elastic energy storage as their means of actuation, specifically those exhibiting non-linear force-displacement profiles.

In addition, I would also like to extend my thanks to Dr. Ardalan Vahidi and Dr. Umesh Vaidya for serving on my committee and teaching me a lot about controls.

Finally, I would like to thank my friends and family. Without their love and support, this journey would not have been possible.

Table of Contents

List of Tables

List of Figures

Chapter 1

Introduction

Origami — the ancient art of paper folding — first emerged in East Asia over four centuries ago [1]. Nowadays, origami is no longer solely treated as a pastime artistic activity. In fact, it has received a surge of interest over the past decade from many research communities, such as mathematicians [2], material scientists, architects [3], physicists [4], biotic researchers [5] and engineers [6–8]. For example, plant biologists used origami folding to explain the deploying mechanisms of tree leaves, flowers, and seed capsules [9, 10], and mathematicians developed algorithmic and computational tools to design complex crease patterns and analyze their folding and unfolding behaviors [11–13]. Architects and engineers, inspired by the vast variations of folding a 2D flat sheet into complex 3D shape, have built various foldable strcutrues of different sizes: from small-scale nano- [14–16] and DNA origamis to meso-scale self-folding robots [17–20] and biomedical devices [21, 22] to large-scale deployable spacecraft [23, 24] and civil infrastructures [25].

Many of these origami-inspired applications have exploited the kinematics of folding. Folding can offer sophisticated shape transformations that are yet programmable which are served as guidelines for many design innovations [26]. In addition, origami structures have tremendous unique advantages including infinite design space, excellent deformability and shape reconfigurability, flat-foldability and single-degree-of-freedom (SDOF) folding mechanism [26]. In this perspective, origami structures have been essentially treated as a structure consisted of rigid panels connected by ideal hinges (a.k.a rigid-foldable origami) [27]. This means that, the elastic deformation of the constituent sheets or the dynamics of folding are often neglected [27].

However, the increasingly diverse and vastly expanding applications of origami have encouraged researchers to study the mechanical properties of folded structures as well, over the past decade. The combination of elastic energy in the deformed facets and creases, and their complex spacial distributions, impart the architected origami materials with various programmable and even unorthodox mechanical properties [27]. For example, recently it has been shown that folding can tailor the structural stiffness [28–31] or generate auxextic effects [32–34]. It can embed bistability and multistability in the structures [33, 35] and create structures with programmable locking and stiffness jump [34]. These findings have led to emergence of a new category of metamaterials and meta-structures called *architected origami materials* [27].

Despite the significant research progress, most of the previous studies on Origami have mainly focused on kinematics or static/quasi-static characteristics of origami folding. Origami folding, on the other hand, could be a dynamic process [26]. The intricate nonlinear elastic properties of origami structures can lead to interesting dynamic characteristics and applications. Nevertheless, studying the dynamics of folding is still a nascent field and there are only a few researches conducted in this area [27].

Dynamics of reciprocal origami folding can be viewed from two different perspectives (figure 1.1). In the first perspective, the main objective is to program or create desired mechanical properties in the structure, by introducing appropriate folds, for a specific dynamic application. For example, Yasuda et al [36] investigated the nonlinear elastic wave propagation in a multiple degree-of-freedom (MDOF) origami metamaterial consisting of Tachi-Miura polyhedron (TMP) cells. They demonstrated that, via utilizing the geometry-induced nonlinearity and the structure periodicity, such TMP-based tubular metamaterials can be developed into vibration and impact mitigating structures with tunable characteristics. In another study, Ishida et al. [37] developed an origami-based cylindrical structure with quasi-zero stiffness characteristics and experimentally demonstrated that it can effectively isolate base excitations at low frequencies. In another study, a cylindrical truss structure inspired by the Kresling folding pattern were investigated for vibration isolation both numerically and experimentally [37, 38]. This vibration isolation function stemmed from a quasi-zero stiffness (QZS) property obtained by integrating a linear spring with the bistable Kresling pattern.

The second perspective on the other hand, focuses on studying the behavior of the origami structure under different dynamic excitations and investigating whether these nonlinear dynamic behaviors might be potentially used for a specific application. For example, Fang et al. [26] conducted a comprehensive experimental and analytical study on the dynamics of origami folding through investigating a stacked Miura-Ori (SMO) structure with intrinsic bistability. They showed that under harmonic base excitation, the SMO exhibits both intrawell and interwell oscillations. In addition, using spectrum analyses, they observed that the dominant nonlinearities of SMO are quadratic and cubic, which generate rich dynamics including subharmonic and chaotic oscillations. In another study, Kidambi and Wang [39] investigated the deployment dynamics of Kresling structures with various system geometries and operating strategies. The axial and off-axis dynamic responses were studied, revealing that the variation of key geometric parameters may lead to regions with qualitatively

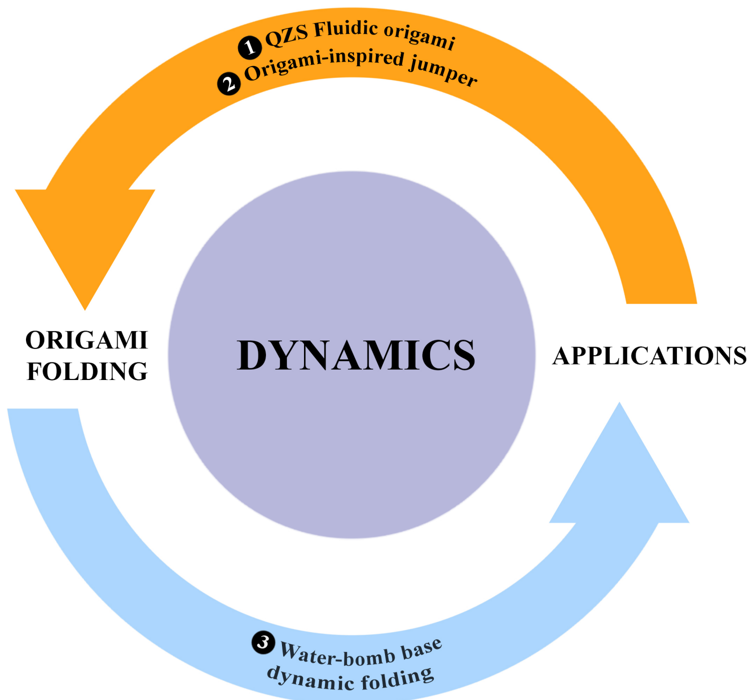

Figure 1.1: Two perspectives of studying dynamics of origami folding and the corresponding studies conducted in this dissertation.

distinct mechanical responses. The sensitivity of dynamic deployment to changes in initial condition and small variations in geometric design were also demonstrated. In another relevant study, Wu et al. [40] explored the transient dynamics of Miura-origami tube under free deployment. They performed a preliminary free deployment test, which indicates that the transient oscillation in the transverse direction is non-negligible and the tube deployment is no longer a single-degree-of-freedom (SDOF) mechanism. The results show that the relationships between the transient dynamic behaviors and the examined parameters are sometimes contradictory in the deploying and the transverse directions, suggesting the necessity of a compromise in design. Unlike these studies, which assume that the origami crease pattern is already folded into the desired shape and the mountain and valley creases are assigned appropriately, Liu and Felton, in another study [41], identified and validated a model to predict configuration switching in mechanical origami systems, even at the flat-unfolded state. They applied this model to design a branching origami structure with 17 distinct configurations controlled by a single actuator and demonstrate reliable switching between these configurations with tailored dynamic inputs.

This research proposal sets out to expand our knowledge of the fundamentals of origami folding dynamics by conducting three different studies.

In Chapter 2, we introduce a novel dynamic application for the previously studied *fluidic origami* structure [42]. In this sense, this study is relevant to the first perspective of analyzing dynamics of origami folding. This study investigates a unique asymmetric quasi-zero stiffness (QZS) property from the pressurized fluidic origami cellular structure, and examines the feasibility and efficiency of using this nonlinear property for low-frequency vibration isolation. We show that the QZS property of fluidic origami stems from the nonlinear geometric relationships between folding and internal volume change, and it can be programmed by tailoring the constituent Miura-Ori crease design. In addition, we show how the unique characteristic of achieving QZS in our study, i.e. pressurization, makes the fluidic origami structure a tunable QZS vibration isolater and distinguishes it from its counterparts. Outcome of this research can lay the foundation for new origami-inspired multi-functional metamaterials and meta-structures with embedded dynamic functionalities. Moreover, the investigations into the asymmetry in force–displacement relationship provide valuable insights for many other QZS structures with similar properties.

Chapter 3 and 4 are are related to each other and the first perspective of understabding origami folding dynamics. In Chapter 3, we investigate the potential effects of utilizing nonlinear springs on the performance of robotic jumping mechanisms. As a theoretical example, we study dynamic characteristics of a jumping mechanism consisting of two masses connected by a generic nonlinear spring, which is characterized by a piecewise linear function. The goal of this study is to understand how the nonlinearity in spring stiffness can impact the jumping performance. To this end, non-dimensional equations of motion of the jumping mechanism are derived and then used extensively for both analytical and numerical investigations. It is found that compression section of the nonlinear spring can significantly increase energy storage and thus enhance the jumping capabilities dramatically. Results of this study is then used extensively in Chapter 4, to investigate the feasibility of utilizing origami folding techniques to create an optimized jumping mechanism. In this chapter, as a theoretical example, we study the dynamic characteristics of a jumping mechanism consisting of two masses connected by a Tachi-Miura Polyhedron (TMP) origami structure with nonlinear stiffness characteristics. We show how the desired *"strain-softening"* effects of the TMP structure can lead to design of jumping mechanisms with optimized performance. Results of this study can lead to emergence of a new generation of more efficient jumping mechanisms with optimized performance in the future.

Chapter 5 on the other hand, focuses on the second perspective of studying origami folding dynamics. In this chapter, we uncover the underlying dynamic characteristics of a bi-stable origami structure and show that how dynamic excitations can be used to fold the structure between its stable states. In particlear, we examine a rapid and reversible origami folding method by exploiting a combination of resonance excitation, asymmetric multi-stability, and active control. The underlying idea is that, by harmonically exciting a multi-stable origami at its resonance frequencies, one can induce rapid folding between its different stable equilibria without the need for using responsive materials. To this end, we use a bi-stable water-bomb base as an archetypal example. Via numerical simulation based on a new dynamic model and experimental testing, we show that the inherent asymmetry of water-bomb base bi-stability can enable dynamic folding with relatively low actuation requirements. In addition, we develop an active feedback control strategy to achieve robust and uni-directional folding from the strong stable state to the weak one, even when the structure is prone to exhibit inter-well oscillations. The results of this study can apply to many different kinds of origami and create a new approach for rapid and reversible (self-)folding, thus advancing the application of origami in shape morphing systems, adaptive structures, and reconfigurable robotics.

Finally, some suggested future work is discussed in Chapter 6.

Chapter 2

Fluidic Origami Cellular Structure with Asymmetric Quasi-Zero Stiffness for Low-Frequency Vibration Isolation

2.1 Abstract

This study investigates a unique asymmetric quasi-zero stiffness (QZS) property from the pressurized fluidic origami cellular structure, and examines the feasibility and efficiency of using this nonlinear property for low-frequency vibration isolation. This QZS property of fluidic origami stems from the nonlinear geometric relationships between folding and internal volume change, and it can be programmed by tailoring the constituent Miura-Ori crease design. Different fluidic origami cellular structure designs are introduced and examined to obtain a guideline for achieving QZS property. A proof-of-concept prototype is fabricated to experimentally vali-

date the feasibility of acquiring QZS. Moreover, a comprehensive dynamic analysis is conducted based on numerical simulation and harmonic balance method (HBM) approximation. The results suggest that the QZS property of fluidic origami can successfully isolate base excitation at low frequencies. In particular, this study carefully examines the effects of an inherent asymmetry in the force-displacement curve of pressurized fluidic origami. It is found that such asymmetry could significantly increase the transmissibility index with certain combinations of excitation amplitude and frequency, and it could also induce a drift response. Outcome of this research can lay the foundation for new origami-inspired multi-functional metamaterial and meta-structure with embedded dynamic functionalities. Moreover, the investigations into the asymmetry in force-displacement relation-ship provide valuable insights for many other QZS structures with similar properties.

2.2 Introduction

The ancient Japanese art of Origami is essentially a technique of developing topologically intricate three-dimensional shapes by folding. Its beauty and simplicity have fostered a surge of interest from the science, mathematics, architecture, and engineering communities. For example, molecular biologists used origami method to fold single-stranded DNA molecules into predetermined shapes, which can be used to form complex self-assembled nanostructures [43–46]. Plant biologists examined the deployment of seed capsules, leaves, and flowers based on origami folding principles [9,47,48]. Mathematicians developed computational tools that can design the appropriate crease patterns for achieving desired shape reconfigurations by folding [11–13]. Engineers also investigated the feasibility of utilizing origami for a wide variety of applications. For example, it is possible to fold flat sheet into stiff and lightweight structures such as sandwich panels with fold cores [32], folded plate shell structures [49], and cellular solids [50]. Moreover, it can be advantageous to leverage the kinematics (aka. shape reconfiguration) of origami folding to advance the deployable aerospace structures [23, 24, 51], self-folding robots [7, 17, 52], medical stents [53], and flexible electronics [54]. Recently, there has been a paradigm shift from harnessing the kinematics of origami to utilizing the mechanics of folding for engineering purposes. As a result, we are witnessing the rapid emergence of origami mechanical metamaterials. These metamaterials are typically made of multiple stacked origami sheets with carefully designed crease patterns [32, 55–57], and the intricate relationships between folding and constituent sheet deformations can impart the origami metamaterials with unique and even unorthodox mechanical properties. For example, it has been demonstrated that origami-based metamaterials and meta-structures can exhibit negative and flipping Poisson's ratio [32–34, 58], self-locking and discrete stiffness jumps [50, 59], and elastic multi-stability [13, 26, 60]. In addition, the stacked origami topology features naturally embedded tubular channels, which can be pressurized to generate adaptive functions. This is the idea behind the so-called pressurized fluidic origami cellular structure (referred simply as "fluidic origami" hereafter), which arises from combining the physical principles behind the plant nastic movements and the design variety of the origami art (Figure 1). By utilizing the relation between folding motion and the enclosed internal fluid volume, fluidic origami is able to exhibit many interesting characteristics. For example it has been studied for its capabilities to achieve shape transformation, stiffness control, and recoverable collapse [42, 61].

Despite these remarkable developments, current state-of-the-art mainly focuses on the kinematics and quasi-static applications of origami folding. However, origami-inspired structures and materials could also show interesting dynamic characteristics under excitations due to the richness of folding geometry. Nevertheless, studying the

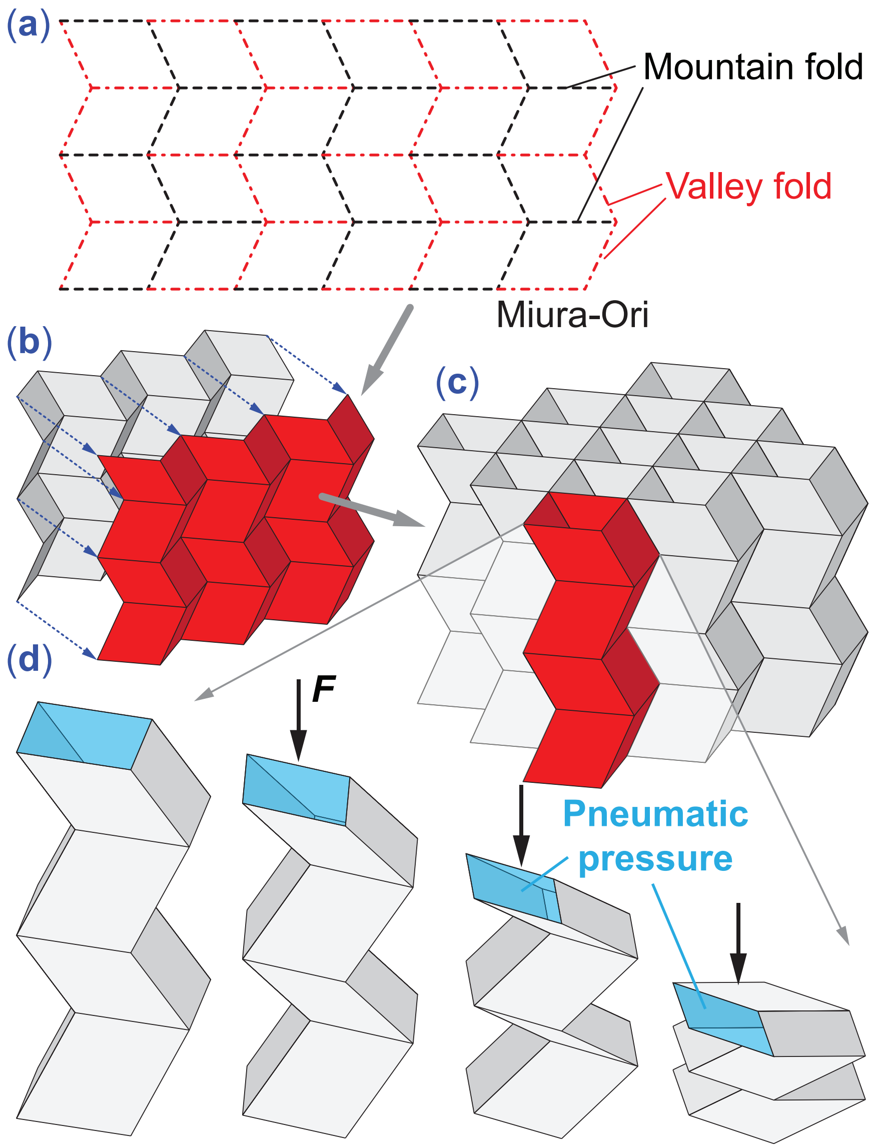

Figure 2.1: The concept of pressurized fluidic origami cellular structure. (a) Crease pattern of the underlying Miura-Ori. (b) Folded Miura-Ori sheets with compatible designs can be stacked and connected to form a space-filling cellular architecture shown in (c). (d) The fluidic origami features naturally embedded tubular channels, which can be pressurized pneumatically. Such pressurization induces the desired quasi-zero stiffness property.

dynamic characteristics of origami-based structures is still a nascent field and there are only a few researches conducted in this area hitherto. Yasuda et al. studied the nonlinear elastic wave propagation in a multiple degree-of-freedom origami metamaterial consisting of Tachi-Miura polyhedron (TMP) cells [36]. They investigated the feasibility of harnessing the geometry-induced nonlinearity of the TMP-based tubular metamaterials for tunable vibration and impact mitigation. Fang, et al. studied the dynamic characteristics of a bi-stable stacked Miura-Ori (SMO) structure and investigated its application in vibration isolation at certain frequencies [26]. Ishida et al. proposed a cylindrical truss structure, inspired by the Kresling folding pattern, for vibration isolation and investigated its performance numerically and experimentally [38,62]. This vibration isolation function stems from a quasi-zero stiffness property obtained by combining the bi-stability of the Kresling pattern and a linear spring. Other than these studies, there are no other literatures on the dynamics induced by origami folding. Therefore, the foremost vision of this research is to expand our knowledge and understand on how to harness the folding-induced mechanical properties to foster a new family of multi-functional origami structures and material systems with dynamic applications. To this end, we introduced a unique quasi-zero stiffness (QZS) characteristics from the pressurized fluidic origami and investigated the feasibility of using this mechanical property for low-frequency vibration isolation [63]. Unlike the cylindrical truss structure studied by Ishida et al., the QZS property of the fluidic origami does not arise from mechanical springs but rather stems from interaction between internal pressure and folding. This provides a unique mechanism for developing an adaptive QZS vibration isolator.

Exploiting quasi-zero-stiffness has been an important topic in low-frequency vibration isolation for decades. For a passive vibration isolator consisting of a mass (m) supported by a linear spring (k), vibration isolation occurs in frequencies over $\sqrt{2k/m}$ [64]. Consequently, one would prefer a smaller stiffness (k) to increase the usable frequency bandwidth; however, this would result in a very small static load carrying capacity. Implementing nonlinear springs with QZS property can be an advantageous solution for this problem. Using the QZS property, the dynamic stiffness of the system would be close to or ideally zero at the equilibrium position, while the static stiffness remains large. Therefore, the system can minimize the vibrations transmission at very low frequencies without sacrificing the static load carrying capacity. Several methods of creating and harnessing the QZS property have be proposed, such as combining vertical and oblique linear springs [65–67], and using structural buckling [68, 69]. In the authors' previous publication, it was shown that QZS property could arise from combining the pressure-induced stiffness and the nonlinear geometric relationships between folding and internal volume [63]. The QZS property is naturally embedded in the structure without the need of any additional springs like in other devices; furthermore, it is feasible to obtain a wide range of appropriate Miura-Ori designs to reach QZS.

The previous study by the authors, however, mainly focused on the design principles of obtaining the QZS property in fluidic origami without any experimental validation, and a comprehensive investigation on its dynamic responses from a low-frequency base excitation is lacking. Such dynamics study is indeed crucial for understanding its performance potentials and limitations as a vibration isolator. Moreover, the reaction force-displacement relationship of the fluidic origami exhibits a strong asymmetry, which is an inherent property stemming from the folding kinematics. The influence of such asymmetry on the base excitation isolation is not fully understood, but can be significant at certain input frequencies and magnitudes. Indeed, there is no comprehensive studies on the influence of inherent asymmetry in the force-displacement relationship of QZS vibration isolator. The only relevant study dealt with asymmetries rising from equilibrium offset based on systems with otherwise symmetric force-displacement curves [70]. Therefore, the objective of this study is to conduct a thorough analytical and experimental investigation on obtaining QZS property in fluidic origami, and then elucidate the influences of asymmetry in its QZS property for low-frequency vibration isolation. Results of this study can lay the foundation for the emergence of a new category of multi-functional, origami-based metamaterials and meta-structures with adaptive dynamic functionalities.

The remaining sections of this paper are organized as follows. Section 3 recapitulates the nonlinear geometrical relationships between origami folding and the desired QZS characteristics. A design criterion for obtaining the QZS property is also presented. Section 4 discusses the experimental verification of the existence of QZS property in a proof-of-concept fluidic origami prototype. Section 5 details the dynamic analysis of utilizing the investigated asymmetric QZS property for base excitation isolation. The behavior of the fluidic origami is analyzed numerically, and harmonic balance method (HBM) is also used to provide deeper insights into the fundamental dynamic characteristics. Section 6 concludes this paper with summary and discussion.

2.3 Folding Kinematics and the Origin of QZS Property

In this section, we briefly discuss the physical principles underpinning the QZS property in fluidic origami, which lays the foundation for the further dynamic investigations. The concept of fluidic origami is based on the idea that connecting Miura-Ori folded sheets along their zig-zag crease lines can create a space-filling cellular topology with naturally embedded tubular features (Figure 2.1) [35]. Miura-Ori is a periodic tessellation, thus one can concentrate on studying the unit cell shown in Figure 2.2(a) as a representative of the whole structure. Three geometric parameters, which remain unchanged regardless of folding, determine the design of Miura-Ori folding pattern. They are the length of two adjacent crease lines (a, b), and the sector angle (γ) between these two lines. Miura-Ori folding pattern is rigid foldable, therefore the facet material can be assumed rigid and the creases can be treated as ideal hinges. With these assumptions, the folding motion of Miura-Ori has one degree-of-freedom that can be described by the dihedral folding angle (θ) defined between the x-y reference plane and the constituent facets (Figure 2.2(a)). To ensure kinematic compatibility so that Miura-Ori sheets do not separate from each other during folding, one needs to apply two geometric constraints: $b_I = b_{II} = b$, and $a_I \cos\gamma_I = a_{II} \cos\gamma_{II}$, where the sub-index I and II represents to the two Miura-Ori sheets in a unit cell [32]. In this way, the folding angles of the two Miura-Ori sheets are directly related so that $\cos\theta_I \tan\gamma_I = \cos\theta_{II} \tan\gamma_{II}$ and the rigid folding of the fluidic origami retains one degree of freedom.

In this study, we choose the folding angle θ_I as the independent variable to describe the folding motion so that the unit cell length can be calculated as follows [35]:

$$L = \frac{2b\cos\theta_I}{\sqrt{1+\cos^2\theta_I \tan^2\gamma_I}}, \tag{2.1}$$

Based on these governing geometric relationships, the enclosed volume of the unit cell can be derived as follows:

$$V = 2a_I^2 b \sin^2\gamma_I \cos\theta_I \left(\sqrt{\frac{\tan^2\gamma_{II}}{\tan^2\gamma_I} - \cos^2\theta_I} + \sin\theta_I\right). \tag{2.2}$$

Equations 2.1 and 2.2 describe the kinematic connections between the external geometries and internal volume change of fluidic origami. Based on these relationships, one can predict that the fluidic origami will fold to a configuration with maximum

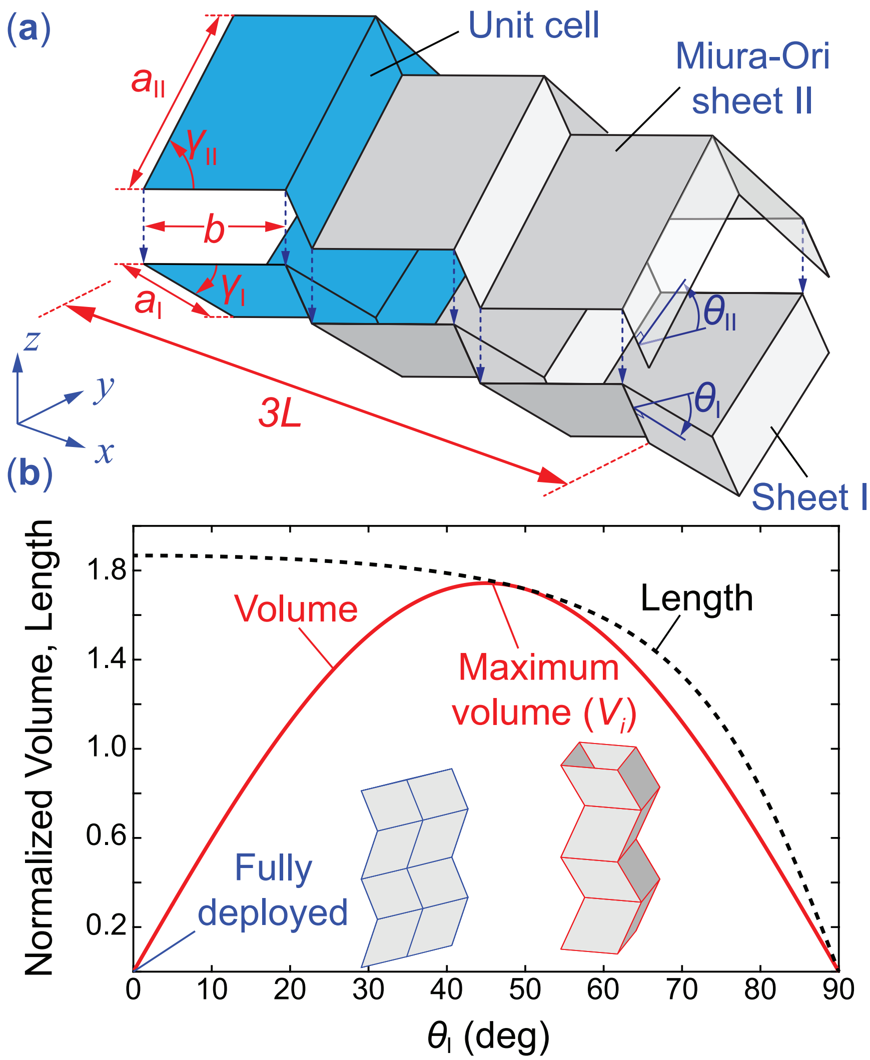

Figure 2.2: The design and kinematics of fluidic origami. (a) The geometry of a tubular channel in fluidic origami, showing the definition of a, b, γ, and θ of the two Miura-Ori sheets. The unit cell is highlighted, and in this plot, the tubular channel has three unit cells (aka. N=3). (b) The strongly nonlinear relationships between geometric quantities and folding angle. In this plot, $a_I = a_{II} = b$, and $\gamma = 70°$. The normalized volume $\hat{V} = V/Na_I^3$ and normalized length $\hat{L} = L/Na_I$.

enclosed volume when it is subject to internal pressure [61]. This is due to the entropy increase from inner energy reduction by volume expansion [71]. Pressurization also imparts nonlinear stiffness to the structure (aka. pressure-induced stiffness [61]. If the fluidic origami structure is subject to external mechanical loads along the x direction (defined in Figure 2.2(a)), the reaction force due to internal pressure can be calculated as follows based on virtual work principle:

$$F_L = -P\frac{dV}{dL} = -P\frac{dV}{d\theta_I}\left(\frac{dL}{d\theta_I}\right)^{-1}, \tag{2.3}$$

where dL is the change in origami length along the external force exertion direction. The pressure-induced stiffness can be defined as the variation of the reaction force with respect to the infinitesimal deformation so that [61]:

$$k_L = \frac{dF}{dL}. \tag{2.4}$$

By observing the force-displacement relationship in Equation 2.3 or the corresponding pressure-induced stiffness, we can investigate the feasibility of obtaining quasi-zero stiffness (QZS) in fluidic origami. To this end, we consider the following scenario of pressurization. The fluidic origami is pressurized with an ideal gas at an initial pressure (P_i) until it folds and settles at the configuration with maximum possible internal volume (V_i). Then the structure is sealed so that the total amount of pressurized gas inside is kept constant. After this, if the fluidic origami deforms via folding due to an external force, its internal pressure (P) and enclosed volume (V) will change accordingly. The ideal gas law states that $PV = nRT$, where n is the amount of substance of gas (in moles),R is the universal gas constant, and T is the absolute temperature of the gas. We assume that the change in internal volume due to folding occurs slowly so the gas temperature (T) is constant. Moreover, n is constant due to the sealing of fluidic origami. Therefore, we can conclude that:

$$PV = P_iV_i = const, \tag{2.5}$$

and the reaction force equation (Equation 2.3) can be updated as follows:

$$F_L = -\frac{P_i V_i}{V}\frac{dV}{d\theta_I}\left(\frac{dL}{d\theta_I}\right)^{-1}. \tag{2.6}$$

Based on equation 2.6, it can be seen that the reaction force and pressure-induced stiffness of the fluidic origami are functions of the internal volume (V) and the length (L) of the unit cell. Figure 2.2(b) shows that these two geometric variables are strongly nonlinear functions of the folding angle (θ_I). Therefore, we can also expect the pressure-induced reaction force and stiffness are strongly nonlinear with respect to the overall folding deformation. It is possible to prescribe the behavior of the force-displacement curve and obtain the desired quasi-zero stiffness (QZS) characteristic for vibration isolation by choosing the appropriate design for the Miura-Ori pattern. In the following subsections, two different design cases are presented, the first case is identical stacked Miura-Ori sheets (ISMO) and the second one is non-identical stacked Miura-Ori sheets (NISMO).

2.3.1 Case 1: Identical Stacked Miura-Ori Sheets (ISMO)

With two identical Miura-Ori sheets, the previously discussed relationships can be simplified because $\gamma_I = \gamma_{II} = \gamma$ and $a_I = a_{II} = a$. Figure 2.3(a, b) shows the force-deformation curves of different ISMO tubes with 2 unit cells based on the same crease lengths ($a = b = 38mm$) but different γ angles. Initial pressure (P_i) is the same at 6.9kPa. It can be seen that when the sector angle γ is less than 69°, the reaction force increases monotonically with deformation, implying a nonlinear positive stiffness. When $\gamma > 69°$, the reaction force curve has a segment of negative stiffness. The critical, quasi-zero-stiffness can be achieved when the sector angle equals to 69°. At this particular sector angle, the length of the negative stiffness segment in the reaction force curve converges to zero. In other words, the tangent stiffness of the fluidic origami is positive throughout its deformation range except for the QZS configuration, where the tangent stiffness equals to zero.

There are several interesting properties from the ISMO fluidic origami of $\gamma = 69°$. First of all, the QZS characteristics is achievable regardless of the initial pressure (P_i). Secondly, the magnitude of reaction force at the QZS point (F_{cr}) is linearly proportional to the magnitude of initial pressure. Finally, the deformation at the QZS point is only a function of origami geometry and does not depend on the initial pressure (Figure 2.3(c)). In Section 2.5, we will detail the benefits of these properties in vibration isolation. In order to find a comprehensive design criterion to obtain the QZS characteristics, we introduce a non-dimensional parameter w as follows:

$$w = \frac{\Delta l}{Na}, \tag{2.7}$$

where Δl is the deformation range with negative stiffness in the reaction force-displacement curve (Figure 2.3(b)), and N is the number of unit cells in a tubular channel. Δl needs to be zero in order to achieve the QZS property in the force-displacement curve. Figure 4(a) illustrates the result of the parametric study on the correlation between w and the Miura-Ori design. It can be seen that for identical Miura-Ori sheets, w is independent of the creases length ratio $k(= a/b)$ and is only a function of sector angle (γ). Based on the aforementioned governing equations and results presented in the Figure 4(a), we can conclude that QZS is reachable only when $\gamma = 69°$ regardless of the crease lengths (a and b).

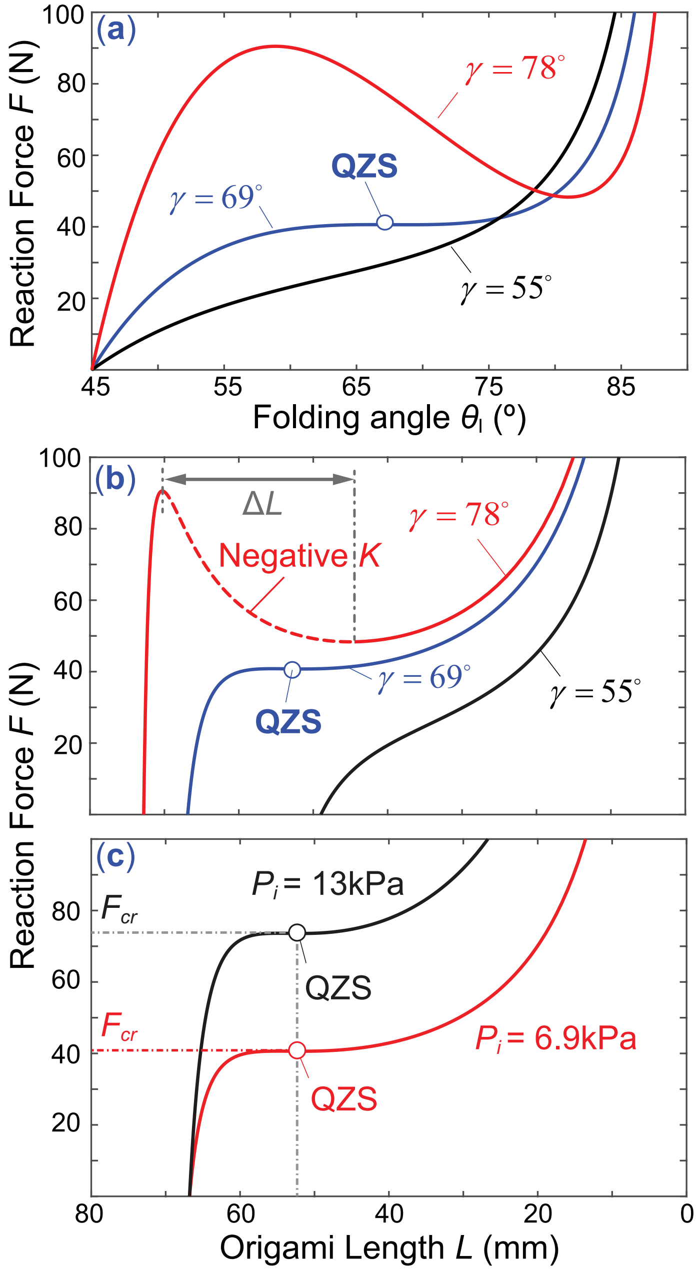

Figure 2.3: Pressure-induced stiffness of the fluidic origami unit cell based on $PV = const$. (a) The reaction force-folding angle relationship, showing the influence of sector angle (γ). (b) The influence of γ angle on the force-deformation relationship. (c) Reaction force-deformation curves based on different initial pressures (P_i). In all of these figures: $a = b = 38mm$.

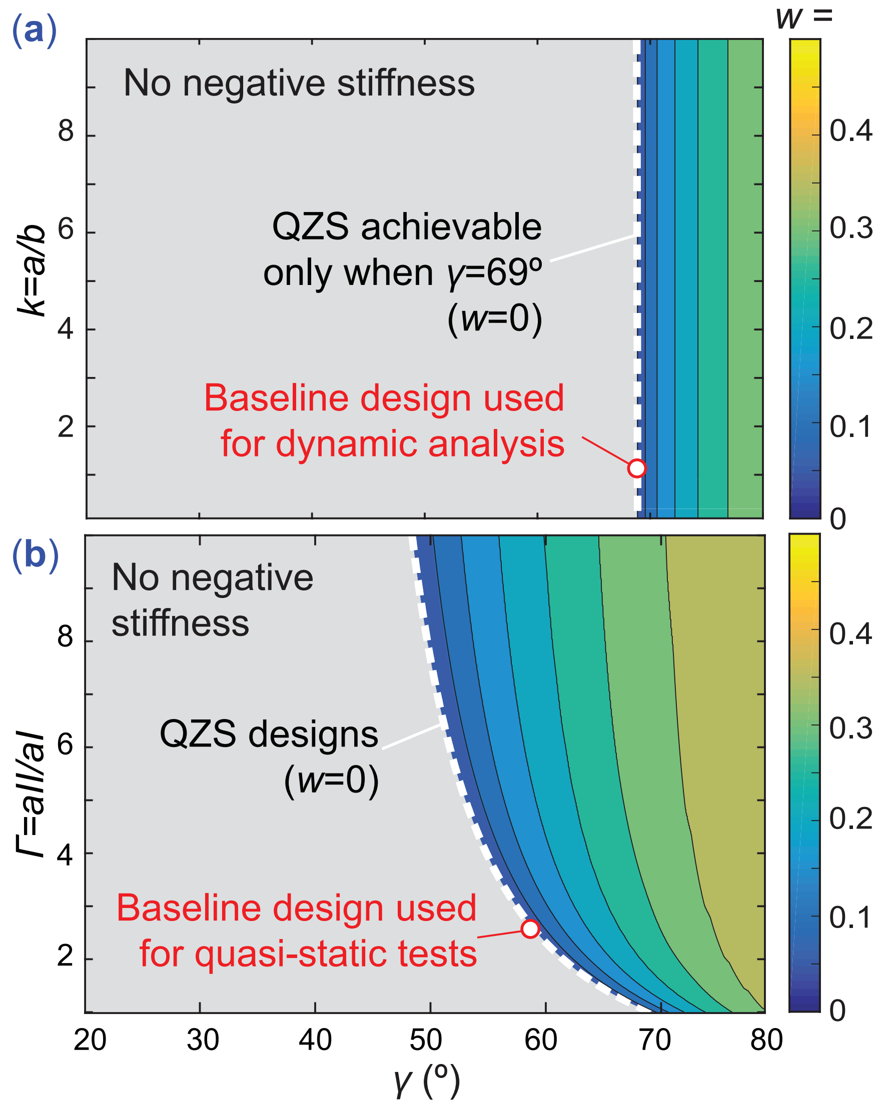

Figure 2.4: Parametric studies for obtaining QZS properties. (a) The relationship between the deformation range with negative stiffness and ISMO design parameters. Grey region represents designs that would not generate any negative stiffness. (b) The relation between the deformation range with negative stiffness and NISMO design parameters. In both cases, Miura-Ori designs that can give QZS property are highlighted. The designs used in the following quasi-static experiment (Section 2.4) and dynamic analysis (Section 2.5) are highlighted.

2.3.2 Case 2: Non-Identical Stacked Miura-Ori Sheets (ISMO)

To study the design criteria for obtaining QZS when the fluidic origami consists of two different Miura-Ori sheets, we introduce a new non-dimensional parameter (Γ) to quantify the design difference between the two sheets:

$$\Gamma = \frac{a_{II}}{a_I}. \tag{2.8}$$

We can follow the same procedure as in the ISMO case to obtain the design criteria for obtaining QZS property in the NISMO case. The results of the parametric study in this case is presented in Figure 2.4(b). In the NISMO case, the designs that can provide QZS depend on both the sector angles and the ratio between crease line lengths. Therefore, the parametric study results in Figure 2.4 can provide the design guidelines to achieve QZS and further dynamic analyses discussed in the section 2.5.

2.4 Proof-of-concept Prototype and the Quasi-static Test

To validate the feasibility of achieving the desired QZS property in fluidic origami, we fabricate and test a proof-of-concept prototype. This prototype is designed to possess the characteristics of an origami structure with rigid facets and hinge-like creases. To this end, facets are first waterjet cut individually from a 0.25 mm thin stainless-steel sheet. Then 0.13 mm thin adhesive-back plastic films (Ultra High Molecular Weight (UHMW) Polyethylene) are used to connect the facets together into a complete origami sheet with hinge-like soft creases. This origami prototype resembles a NISMO structure with four connected tubular channels, each

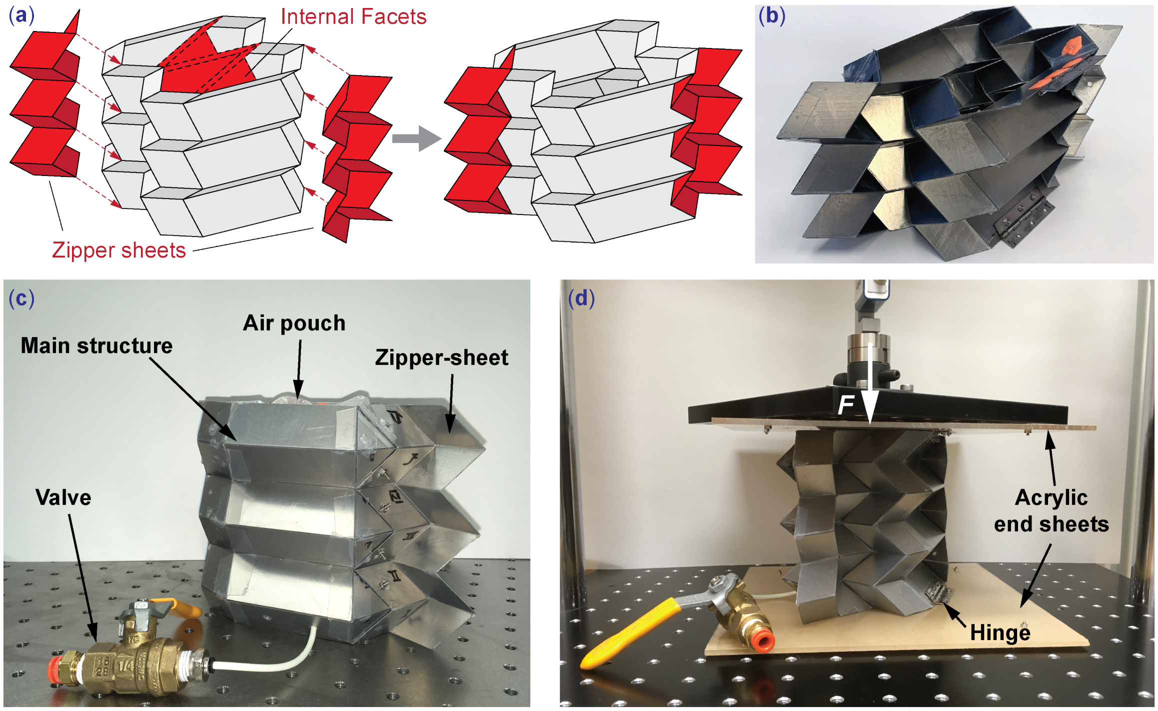

Figure 2.5: Proof-of-concept experimental tests. (a) Schematic drawing showing the design and assembly of the fluidic origami prototype. The zipper-sheets and internal facets are highlighted. (b) Finished prototype made from water-jet cut steel sheets and adhesive plastic films. (c) In this figure, the fluidic origami prototype has been pressurized through a custom-made air pouch to its maximum internal volume configuration. Note that the end valve has been closed and disconnected from the pressure supply to ensure a constant PV according to the governing Equation (6). (d) The experimental set-up for the quasi-static test.

consisting three unit-cells (Figure 2.5(a)). Design parameters used in this prototype are summarized in Table 2.1. The fluidic origami prototype is also equipped with two "zipper sheets" to constraint the overall deformation to rigid-folding only. These zipper-sheets have the same designs as the smaller Miura-Ori sheet I used in the main structure, but they are rotated about the lengthwise x-axis (Figure 2.5(a)). Because of this rotation, the zipper-sheet can drastically increase the eigen-stiffness of undesired deformations (e.g. bending and squeezing) without hindering the rigid-folding deformation [72].

Table 2.1: Design parameters used in the proof-of-concept prototype

a_I	b	a_{II}	γ_I	γ_{II}
30mm	30mm	$2.5a_I$	59°	78°

Furthermore, we remove the internal facets in the fluidic origami prototype so that the four initially separated channels are combined into one (Figure 2.5(a, b)); this makes it much easier to apply a uniform internal pressure. Removing the internal facets, however, does not change the governing relationship between internal pressure and reaction force as defined in Equation 2.6, because it does not alter the kinematic relationships between rigid-folding, total volume, and overall length of the fluidic origami. A custom-made cubic-shaped air pouch is inserted to the fluidic origami to provide internal pressurization. The pouch is made of 0.1-mm thin low-density polyethylene film (LDPE).

The main structure is then connected to two 2.77-mm thick clear cast acrylic end sheets using 0.635-mm thick piano hinges to provide the required contact surface for the quasi-static compression test. It is worth noting that this hinge only anchor one origami facet to the end sheet (Figure 2.5(d)), and other facets in contact with the end sheets are free to move. The compressive force-displacement curve of the pressurized fluidic origami structure is tested on a tensile test machine (ADMET eXpert 5601 with a 250lbf load cell, 3mm/min displacement rate) (Figure 2.5(d)). The structure is pressurized with initial pressure of 1.38kPa until it reaches its maximum volume (Figure 2.5(c)). During testing, the pressurized air is constrained inside the air pouch by closing the connected on/off valve (Figure 2.5 (c)). Five sets of measurements are performed; and Figure 6 depicts the averaged force-displacement curve, the corresponding standard deviation, and the analytical prediction based on Equation 2.6. The quasi-static test on the fluidic origami structure exhibits a good repeatability among the five sets of measurements, and the stand-ard deviation is

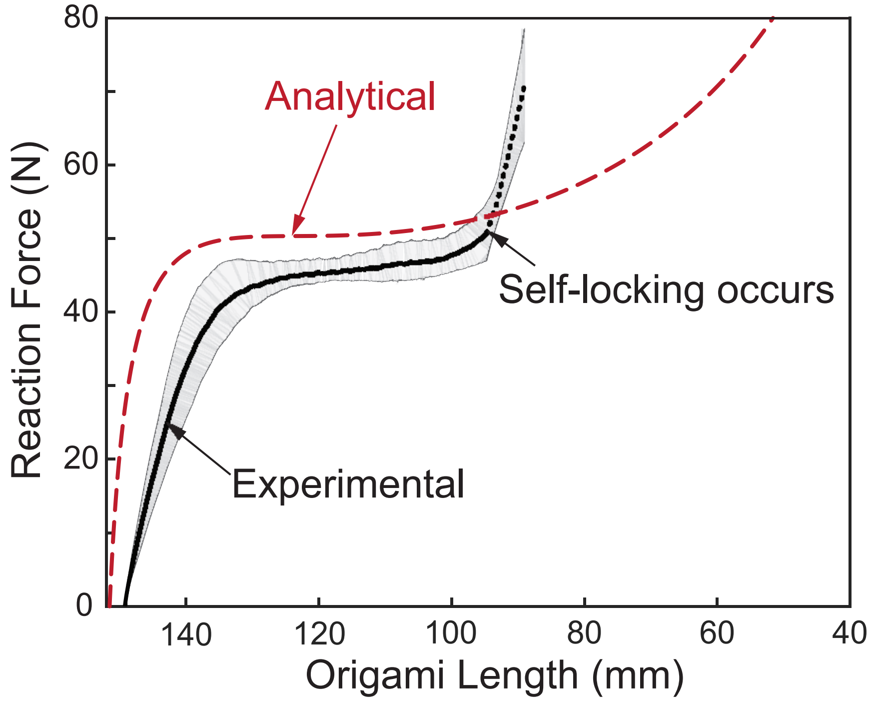

Figure 2.6: The force-displacement relationships. The dashed curve represents the analytical result and the solid and dotted curve shows the averaged experimental result. The shaded grey region represents the standard deviation of the measurements.

about 3 percent of the average value in the QZS region.

2.5 Dynamic Analysis of Fluidic Origami with QZS Properties

In this section, we examine the effectiveness of utilizing the fluidic origami for low-frequency base excitation isolation. To avoid unnecessary complexities, here we use the design parameters obtained in the ISMO case study, that is $a_I = a_{II} = a$, $b = a$, and $\gamma = 69°$. However, the physical principles and design insights obtained in this case study can be applied to any other fluidic origami designs that can exhibit QZS property. Figure 2.7 illustrates the system setup for vibration isolation, where

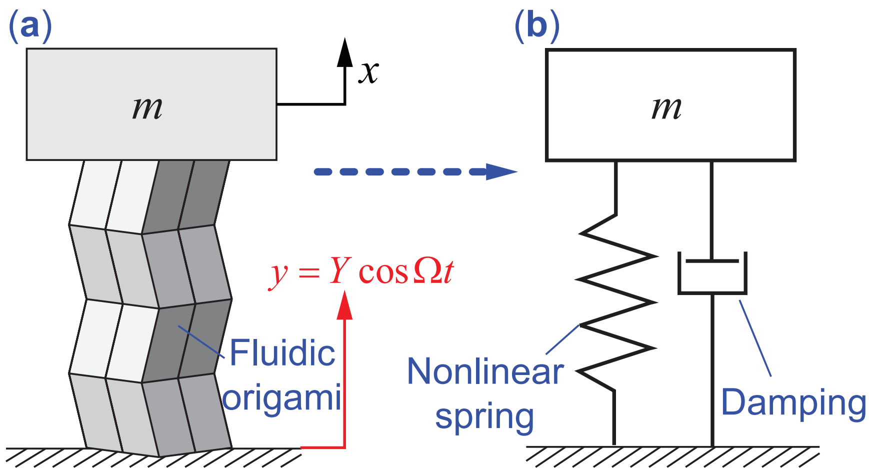

Figure 2.7: Setup of the dynamic analysis. (a) Schematic diagram of using fluidic origami for base vibration isolation. (b) The equivalent discrete system.

the fluidic origami is assumed massless and a lumped mass (m=1kg) is attached at the top. In this way, one can describe the origami structure as a combination of a nonlinear spring and a damping element between the lumped mass and base. It is worth highlighting that utilizing the QZS property for vibration isolation requires that the static equilibrium of the mass-spring-damper system shown in Figure 7 occurs at the QZS configuration. That is, the weight of the lumped mass should be equal to the reaction force at the QZS point ($mg = F_{cr}$). To achieve this, we can use the unique property of pressurized fluidic origami that the magnitude of the reaction force at the QZS configuration is linearly proportional to the magnitude of the initial pressure (Figure 2.3(c)). Therefore, the initial pressure can be adjusted according to the following equation:

$$P_i = mg\left[-\left(\frac{V_i}{V}\right)\frac{dV}{dL}\right]^{-1}\Bigg|_{QZS}. \tag{2.9}$$

We can then write the governing dynamic equation of motion as:

$$\ddot{u} + 2\zeta\dot{u} + F(u) = \Omega^2 Y \cos \Omega t \tag{2.10}$$

where, $u = x - y$ is the relative displacement between the lumped mass and the base. $F(u)$ is the reaction force of the fluidic origami. ζ is the damping ratio, which is assumed be to 0.3 for this study. Ω is the excitation frequency, and Y is the base excitation amplitude. The reaction force (F), which exhibits the desired QZS characteristics, is determined based on the fluidic origami constitutive relationship in Equation 2.6 and appropriate initial pressure according to Equation 2.9. To characterize the performance of the base excitation isolation, we introduce a transmissibility index (TR), defined as the ratio of the root mean squares of mass and base displacements $x(t)$ and $y(t)$ respectively:

$$TR = \frac{RMS(x(t))}{RMS(y(t))}. \tag{2.11}$$

The governing equation of motion (equation 2.10) based on the actual force-displacement curve (Equation 2.6) is solved numerically using MATLAB "ode23s" solver. The steady-state time response (examples shown in Figure 2.8) can be used to calculate the transmissibility index (TR).

Beside numerical simulation, another common method for examining the QZS vibration isolators is to use odd order polynomials to approximate the reaction force-displacement curve around the QZS point, so that the established dynamic analysis methods like harmonic balance (HBM) can be used. For example, a third-order polynomial approximation can be applied to QZS structures and effectively turns the overall system into a classical Duffing oscillator [65, 67, 73–75]. Zhou et al. [76] also used a cubic polynomial by truncating the Taylor series expansion about the

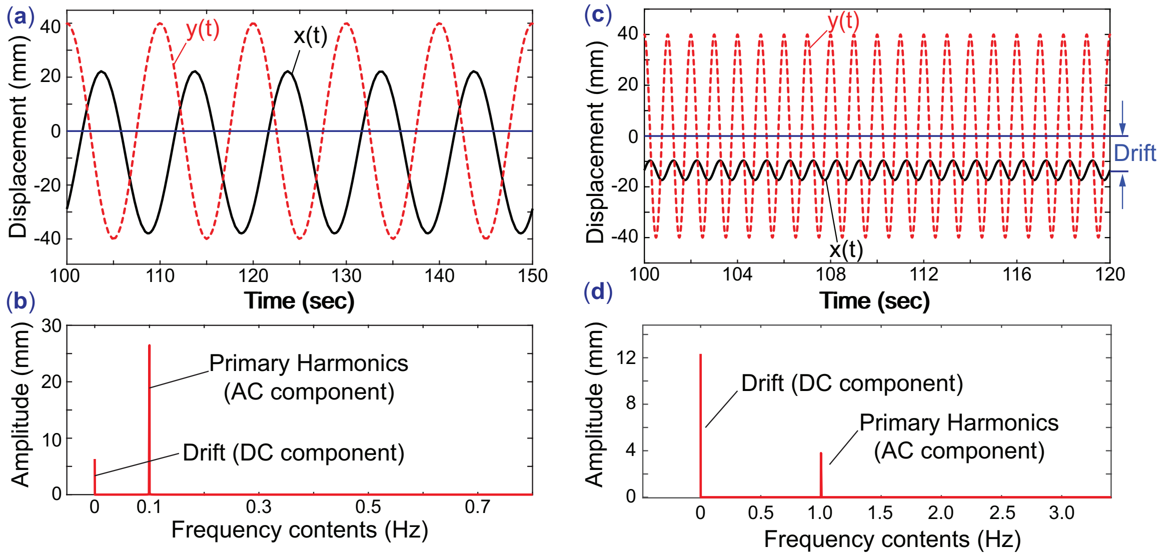

Figure 2.8: Numerical simulation of the fluidic origami isolator based on actual force-displacement curve according to equation 2.6. (a, b) Sample steady-state time response with $\Omega = 0.1Hz$, $Y = a$ and the corresponding FFT result. (c, d) Another sample response with different input ($\Omega = 1Hz$, $Y = a$).

equilibrium to examine a cam-roller-spring QZS isolator. Some other studies even used fifth odd order polynomials [77, 78].

Nonetheless, these odd order polynomial fittings are fundamentally similar in that they produce symmetric force displacement curves with respect to the zero origin. That is, $f(x) = -f(-x)$, where x is an arbitrary displacement from the QZS point and $f(x)$ is the force-displacement relationship. However, the force displacement curve of the fluidic origami shown in Figure 2.3 is strongly asymmetric. To understand how such asymmetry influences the dynamic response and performance of base excitation isolation, we apply both symmetric (Section 2.5.1) and asymmetric (Section 5.5.2) polynomial fitting, and compare the corresponding HBM results to the dynamic response based on the actual force-displacement curve.

2.5.1 Dynamic Analysis based on Symmetric Polynomial Fitting

A simple, symmetric cubic fitting assumes the reaction force $F(u) \simeq \alpha u^3$, where the cubic stiffness coefficient α can be found via the least square method (Figure 2.9(a)). The governing equation of motion (equation 2.10) can be updated accordingly to:

$$\ddot{u} + 2\zeta\dot{u} + \alpha u^3 = \Omega^2 Y \cos \Omega t. \tag{2.12}$$

This essentially represents a Duffing oscillator with a zero linear stiffness term. Assuming a fluidic origami structure consisting of two internally connected unit cells (N=2) and an initial pressure of $P = 13.8KPa$, the cubic stiffness coefficient turns out to be $\alpha = 81020N/m^3$. /par The steady state solution of equation 2.12 can be approximated by harmonic balance method (HBM), which is a powerful method for analyzing the steady-state behavior of strongly nonlinear dynamic systems [74,79,80]. According to HBM, the solution of equation 2.12 can be approximated as:

$$u(t) = U_1 \cos \Omega t + U_2 \sin \Omega t. \tag{2.13}$$

Substituting the assumed $u(t)$ into the simplified dynamic equation (equation 2.12) and discarding higher order harmonic terms give the following nonlinear polynomial equations:

$$\begin{cases} -\Omega^2 U_1 + 2\Omega\zeta U_2 + \frac{3}{4}\alpha {U_1}^3 + \frac{3}{4}\alpha U_1 {U_2}^2 - \Omega^2 Y = 0, \\ -\Omega^2 U_2 - 2\Omega\zeta U_1 + \frac{3}{4}\alpha {U_2}^3 + \frac{3}{4}\alpha U_2 {U_1}^2 = 0, \end{cases} \tag{2.14}$$

which can be solved numerically to obtain the two unknown coefficients (U_1,U_2). Once these two coefficients are determined, equation 2.12 can be updated to provide the

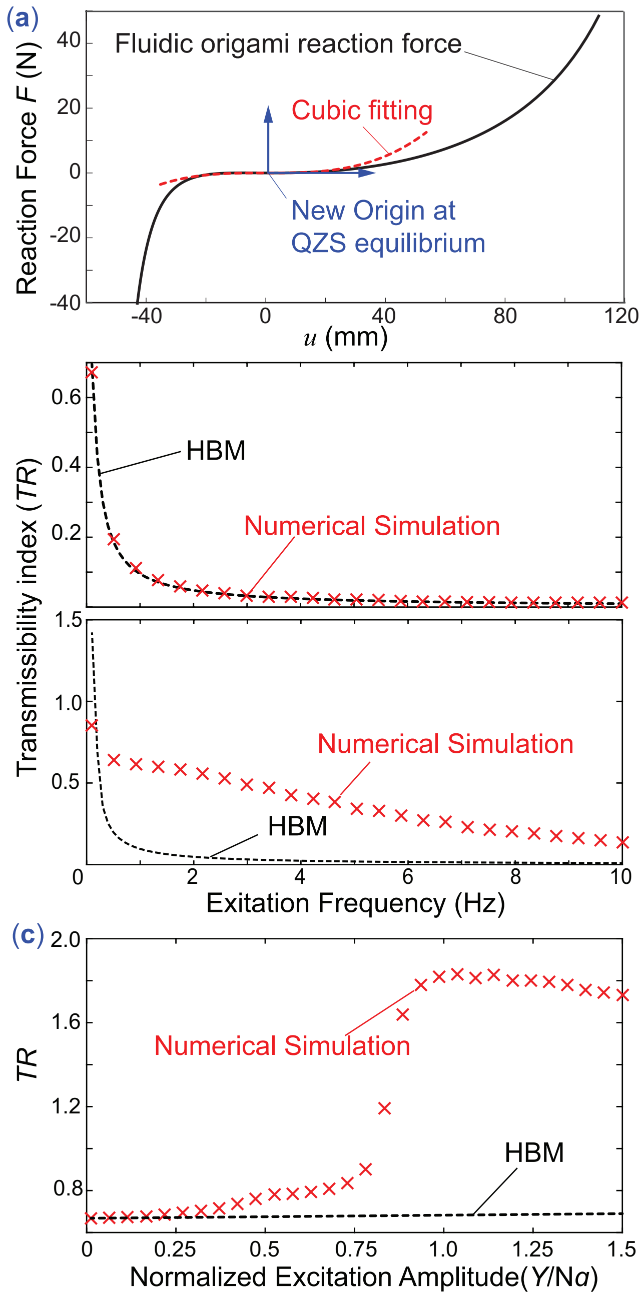

Figure 2.9: Dynamic analysis based on symmetric cubic polynomial fitting. (a) The setup of cubic polynomial fitting. (b, c) Relationships between TR and excitation frequencies at $Y = 0.125Na$ and $0.75Na$, respectively. (d) The relationship between TR and excitation amplitudes ($\Omega = 0.1Hz$).

approximate solution for the relative displacement $u(t)$ and then the TR index. Figure 2.9(b-c) show the transmissibility index obtained by numerical simulation and

HBM corresponding to two different base excitation amplitudes: $Y = 0.125Na$ and $Y = 0.75Na$, where a is the crease line length, and N is the number of cells. For the small excitation amplitude, HBM results based on a cubic fitting agree well with the numerical simulation; however, there are significant discrepancies at the higher excitation amplitude. Such discrepancy in TR magnitude at higher excitation amplitude is also shown in Figure 2.9(d), which depicts the comparison between cubic fitting prediction and numerical simulation for a wide range of excitation amplitudes with a constant frequency ($\Omega = 0.1Hz$). Therefore, the HBM results based on symmetric polynomial fitting cannot accurately predict the qualitative behavior of the base isolation behavior, especially at higher excitation amplitudes.

Besides the discrepancies in transmissibility predictions at higher excitation amplitude, the symmetric cubic fitting also fails to predict the emergence of a drift or zero-frequency "DC component" observed in the numerical simulation based on the actual-force displacement curve (Figure 2.8(b, d)). Such a drift or DC component is especially evident at a higher frequency (Figure 2.8(b)) so that the lumped mass moves to another position rather than the static equilibrium and oscillates around that point. Indeed, it can be proven that for any dynamic system described by a second order differential equation of the form:

$$\ddot{u} + c\dot{u} + f(u) = F\cos(\Omega t), \tag{2.15}$$

where the reaction force $f(u)$ is a summation of odd-order polynomials exhibiting a symmetric behavior around the origin:

$$f(u) = \alpha_{m_1}u^{m_1} + \alpha_{m_2}u^{m_2} + ... + \alpha_{m_n}u^{m_n}, \tag{2.16}$$

and $m_i (i = 1, 2, ..., n)$ are odd and positive integers, the system cannot exhibit any drift or zero frequency response. To prove by contradiction, we assume the solution of equation 2.15 includes a constant drift term U_0 so that:

$$u = U_0 + U_1 \cos \Omega t + U_2 \sin \Omega t. \tag{2.17}$$

Applying HBM and collecting zero-frequency components produces the following equation:

$$\begin{aligned}
&U_0 \sum_{k=0}^{k_{f_1}=\frac{m_1-1}{2}} \sum_{l=0}^{l_{f_1}=\frac{m_1-(2k+1)}{2}} {U_0}^{2k}(\alpha l_1 {U_1}^{m_1-(2k+1)-2l} {U_2}^{2l}) + ... \\
&U_0 \sum_{k=0}^{k_{f_2}=\frac{m_2-1}{2}} \sum_{l=0}^{l_{f_2}=\frac{m_2-(2k+1)}{2}} {U_0}^{2k}(\alpha l_1 {U_1}^{m_2-(2k+1)-2l} {U_2}^{2l}) + ... \\
&U_0 \sum_{k=0}^{k_{fn}=\frac{m_n-1}{2}} \sum_{l=0}^{l_{fn}=\frac{m_n-(2k+1)}{2}} {U_0}^{2k}(\alpha l_1 {U_1}^{m_n-(2k+1)-2l} {U_2}^{2l}) = 0
\end{aligned} \tag{2.18}$$

It is obvious that $2k$, $m_i - (2k + 1) - 2l$, and $2l$ are all positive even integers. Since U_0, U_1, and U_2 are real values, equation 2.18 only has two possible solutions:

$$\begin{cases} U_0 = 0, \\ U_0 = U_1 = U_2 = 0, \end{cases} \tag{2.19}$$

and only the first solution is non-trivial. Therefore, we can conclude that for any dynamic system described by Equation 2.15, which has a symmetric force-displacement reaction, it cannot produce any drift or zero-frequency response as $U_0 = 0$.

Therefore, it can be concluded that a symmetric approximation of the force displacement curve could not fully capture the dynamic behaviors of the fluidic origami. Our results imply that the asymmetry of the fluidic origami force-displacement relationship is crucial in that: 1) it could significantly increase the transmissibility index at higher excitation amplitudes and 2) it could induce a drift response. To validate these observations, we add even-order polynomials to our fitting to introduce an asymmetry around the QZS point, and the corresponding predictions are discussed in the following subsection.

2.5.2 Dynamic Analysis based on Asymmetric Polynomial Fitting

It should be noted that the reaction-force displacement of the fluidic origami is a complex nonlinear function; therefore, it is extremely hard to replicate its exact behavior through polynomial fitting. Obviously, a higher order polynomial fitting can better replicate the force displacement curve of the fluidic origami. Figure 2.10(a) shows the comparison between some polynomial fittings, which indicates that one needs to consider a ninth-order polynomial curve to obtain a quantitatively accurate prediction. However, including a ninth-order polynomials in HBM makes the study extremely arduous and unreasonable. Alternatively, we can concentrate on qualitatively revealing the effects of asymmetry on the overall system dynamics. For this reason, we use the simplest fitting that can preserve the asymmetric behavior of the force-displacement curve, that is, a combination of second and third order polynomials. It is worth noting that there should not be a linear term in the fitting in order to satisfy the zero stiffness at the origin. With these considerations, force-displacement function can be approximated as:

$$F(u) = \alpha_2 u^2 + \alpha_3 u^3, \tag{2.20}$$

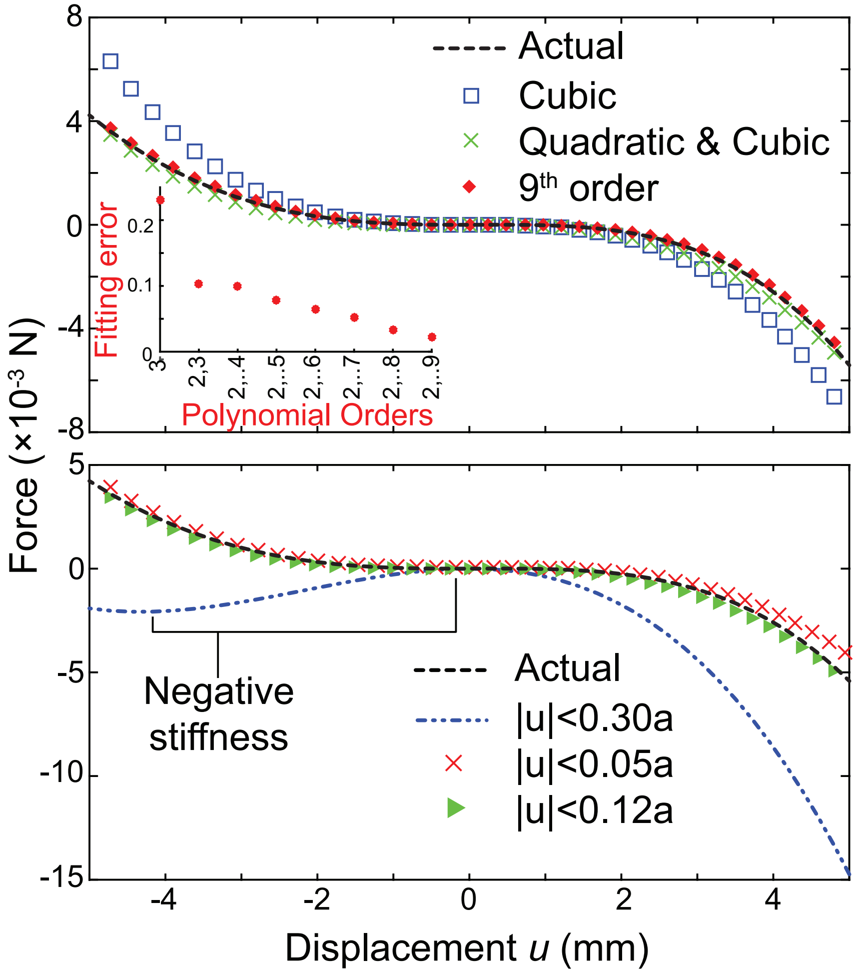

Figure 2.10: Fitting with quadratic and cubit polynomial terms. (a) Comparison between some polynomial fittings with different orders performed for range $|u| < 0.12a$ The insert plot shows the corresponding magnitude of fitting error ($= RMS(u_{actual} - u_{fit})/RMS(u_{actual})$). (b) Actual force-displacement curve and the comparison of three different fitting results based on cubic and quadratic polynomials with different ranges of fitting.

where the quadratic and cubic stiffness term α_2 and α_3 are approximated by the least square method. Estimating the values of these two stiffness terms are not trivial. Figure 2.10(b) shows the actual force-displacement curve according to Equation 2.6 along with three different fitting results. These fittings all include cubic and quadratic terms as in Equation 2.20, but differ in the displacement range where the least square method is applied. It can be clearly seen that if the range is too big, the fitting is not able to replicate the QZS property of the actual force displacement-curve, that is, the sign of stiffness changes to negative near origin. On the other hand, if the range is too small, the fitting deviates significantly from the actual force displacement curve. Therefore, one needs to use the maximum displacement range for fitting as long as the QZS property is qualitatively preserved at the equilibrium point ($|u| < 0.12a$ in this case), which results in: $\alpha_2 = 333004 N/m^2$, $\alpha_2 = 51260 N/m^2$.

By incorporating the quadratic and cubic fitting, the equation of motion (Equation 2.10) can be updated to:

$$\ddot{u} + 2\zeta\dot{u} + \alpha_2 u^2 + \alpha_3 u^3 = \Omega^2 Y \cos\Omega t. \tag{2.21}$$

Now we can use HBM to analyze the transmissibly at large base excitation amplitude as well as the emergence of drift (DC) component in the dynamic response. Substituting the assumed solution in Equation 2.17 into Equation 2.21 produces the following algebraic equations:

$$\begin{cases} \alpha_2({U_0}^2 + \frac{1}{2}({U_1}^2 + {U_2}^2)) + \alpha_3({U_0}^3 + \frac{3}{2}{U_0}^2{U_1}^2 + \frac{3}{2}{U_0}^2{U_2}^2) = 0, \\ -\Omega^2 U_1 + 2\Omega\zeta U_2 + 2\alpha_2 U_0 U_1 + \alpha_3(3{U_0}^2 U_1 + \frac{3}{4}{U_1}^3 + \frac{3}{4}U_1{U_2}^2) = \Omega^2 Y, \\ -\Omega^2 U_2 - 2\Omega\zeta U_1 + 2\alpha_2 U_0 U_2 + \alpha_3(3{U_0}^2 U_2 + \frac{3}{4}{U_2}^3 + \frac{3}{4}{U_1}^2 U_2) = 0. \end{cases} \tag{2.22}$$

We Introduce two new variables, A_1 and θ, so that:

$$\begin{cases} U_1 = A_1 \cos\theta, \\ U_2 = -A_1 \sin\theta. \end{cases} \tag{2.23}$$

The relative displacement (u) can be expressed in terms of the new variables as:

$$u = U_0 + A_1 \cos(\Omega t + \theta), \tag{2.24}$$

where U_0 represent the drift or DC component of the overall dynamic response, and A_1 represents the primary harmonics or AC component. Through some mathematical manipulation, it can be shown that U_0 satisfies the following ninth-order polynomial equation:

$$\begin{aligned}
&(-\tfrac{225}{16}\alpha_3{}^5)U_0{}^9 + (-\tfrac{675}{16}\alpha_2\alpha_3{}^4)U_0{}^8 + (\tfrac{45}{4}\Omega^2\alpha_3{}^4 - \tfrac{795}{16}\alpha_2{}^2\alpha_3{}^3)U_0{}^7 + \\
&(-\tfrac{456}{16}\alpha_2{}^3\alpha_3{}^2 + \tfrac{105}{4}\alpha_2\alpha_3{}^3\Omega^2)U_0{}^6 + (-\tfrac{17}{2}\alpha_2{}^4\alpha_3 + \tfrac{87}{4}\alpha_2{}^2\alpha_3{}^2\Omega^2 - \tfrac{9}{4}\alpha_3{}^3\Omega^4 - 9\alpha_3{}^3\zeta^2\Omega^2)U_0{}^5 + \\
&(-\alpha_2{}^5 + \tfrac{31}{4}\alpha_2{}^3\alpha_3\Omega^2 - \tfrac{15}{4}\alpha_2\alpha_3{}^2\Omega^4 - 15\alpha_2\alpha_3{}^2\zeta^2\Omega^2)U_0{}^4 + \\
&(\alpha_2{}^4\Omega^2 - \tfrac{7}{4}\alpha_2{}^2\alpha_3\Omega^4 - 7\alpha_2{}^2\alpha_3\zeta^2\Omega^2 - \tfrac{27}{8}\alpha_3{}^3\Omega^4Y^2)U_0{}^3 + \\
&(-\alpha_2{}^3\zeta^2\Omega^2 - \tfrac{1}{4}\alpha_2{}^3\Omega^4 - \tfrac{27}{8}\alpha_2\alpha_3{}^2\Omega^4Y^2)U_0{}^2 + (-\tfrac{9}{8}\alpha_2{}^2\alpha_3\Omega^4Y^2)U_0 - \tfrac{1}{8}\alpha_2{}^3\Omega^4Y^2 = 0,
\end{aligned} \tag{2.25}$$

which has a non-trivial real solution, indicating the emergence of drift due to the asymmetry in force-displacement curves. Figure 2.11(a, b) show the system time responses based on numerical simulation and HBM for $Y = 0.25Na$ and $\Omega = 0.1Hz$. HBM based on the asymmetric polynomial fitting successfully predicts the drift (DC component) as well as the primary harmonics (AC component). Moreover, it can also be shown that the following relation holds between U_0 and A_1:

$$A_1{}^2 = -\frac{\alpha_2 U_0{}^2 + \alpha_3 U_0{}^3}{\frac{1}{2}\alpha_2 + \frac{3}{2}\alpha_3 U_0}. \tag{2.26}$$

And θ can be derived by solving the following equation:

$$\tan\theta = -\frac{2\Omega\zeta}{-\Omega^2 + 2\alpha_2 U_0 + 3\alpha_3 U_0{}^2 + \frac{3}{4}\alpha_3 A_1{}^2}. \tag{2.27}$$

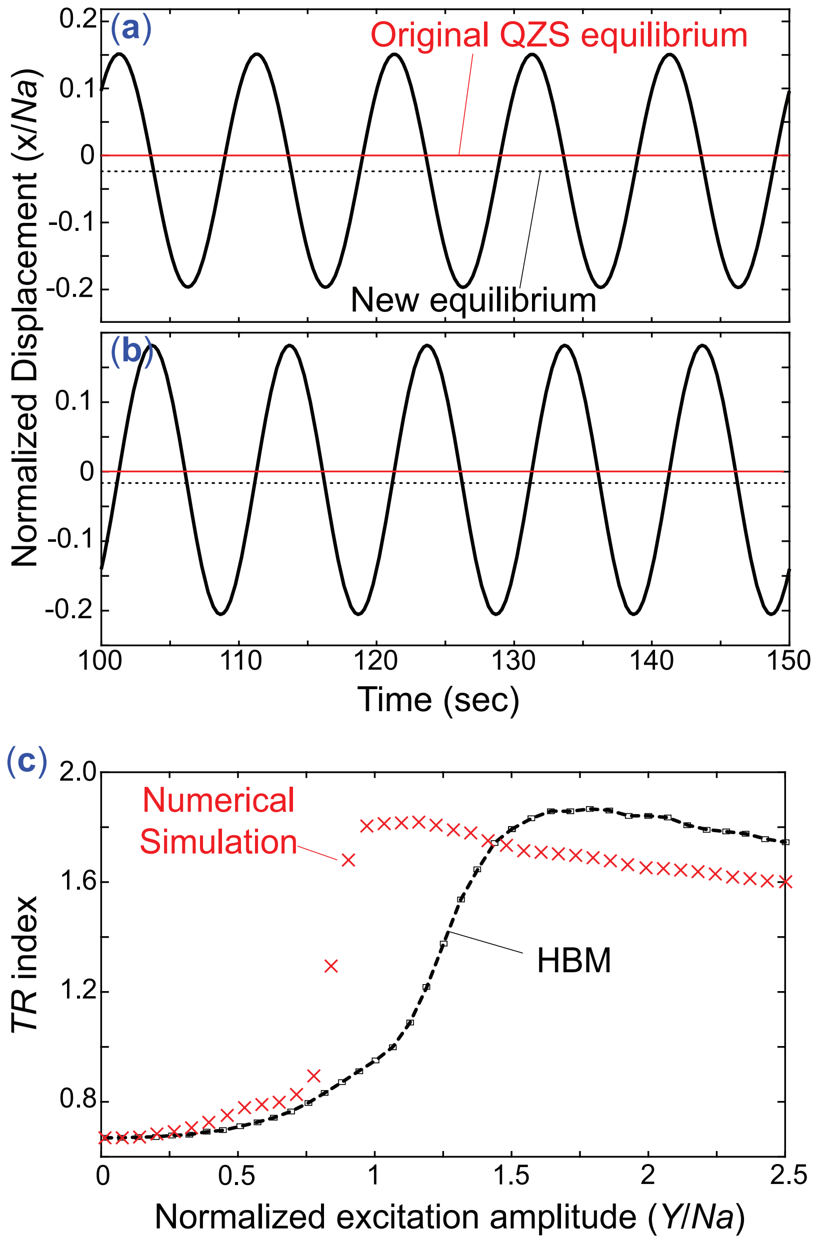

Figure 2.11: Sample steady-state time responses of system based on (a) numerical simulation and (b) HBM for $Y = 0.25Na$ and $\Omega = 0.1Hz$. (c) The TR results derived by numerical simulation based on Equation 2.10 and HBM based on asymmetric fitting. Comparing this result to that in Figure 2.9(c), it is evident that the asymmetry plays a crucial role in the high TR values at high excitation amplitude.

Once U_0, A_1, and $theta$ are solved, they can be substituted in equation 2.24 to approximate the steady-state response. We can then use this approximation to calculate the transmissibility (TR) index. Figure 2.11(c) shows the TR results derived by numerical simulation based on Equation 2.10 and HBM based on asymmetric fitting, respectively. Both results clearly show a significant increase of TR at higher base excitation amplitude. The discrepancy shown in this figure is a result of fitting error from using a relatively low order polynomials. However as mentioned earlier, the purpose of this approximation using HBM is to qualitatively elucidate the effect of asymmetry in force-displacement curves, thus the presented result indeed provides valuable insights into the dynamic behaviors of fluidic origami.

2.5.3 Base Excitation Performance Analysis

Now that we have an understanding on the influence of asymmetry from the force-displacement relationship, in this section, we comprehensively evaluate the based excitation isolation performance of the fluidic origami based on the actual force-displacement curve. Figure 2.12(a) represents the correlations among the transmissibility index, normalized base excitation amplitude, and excitation frequency. Different colors in this figure represent the value of TR index, and the fluidic origami is considered successful in performing its task when $TR < 1$. The TR index is consistently below one except at very small frequencies and high base excitation amplitudes (highlighted region in this figure), therefore, fluidic origami with QZS is indeed an effective isolator.

We further analyze the contribution of drift (DC component) and primary harmonics (AC component) to the overall dynamic response. To this end, FFT analysis is applied to the steady-state time responses corresponding to different excitation frequencies and amplitudes. Figure 2.12(b, c) show the magnitudes of DC (DC/Y) and AC (AC/Y) components, respectively.

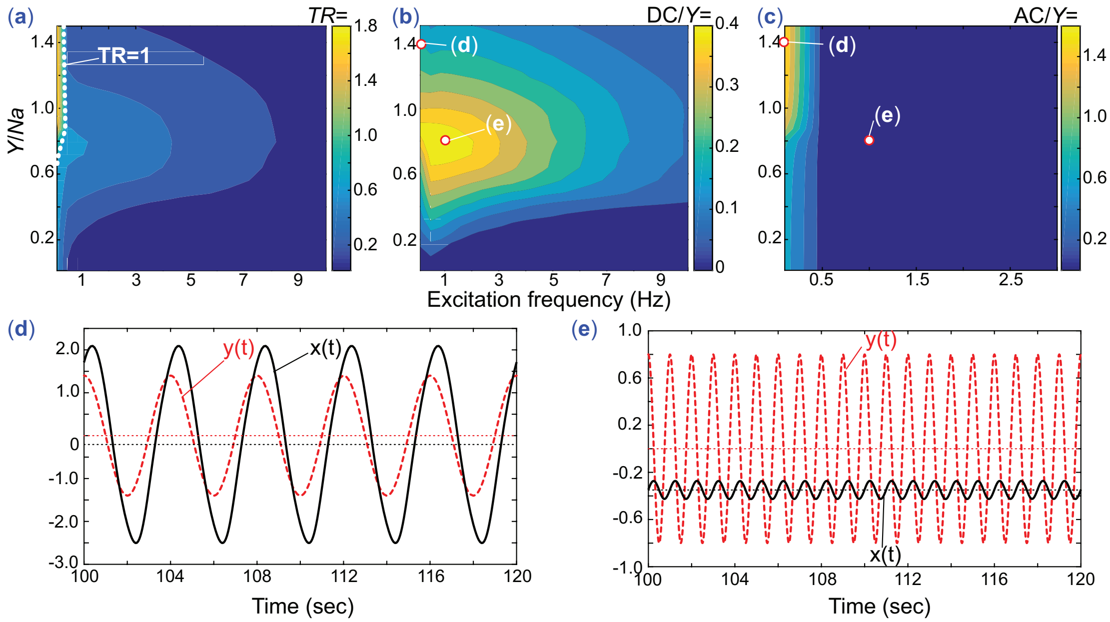

Figure 2.12: Base excitation performance study (a) The relationship among the TR index magnitude, normalized excitation amplitude and normalized excitation frequency. The performance threshold of $TR = 1$ is highlighted. (b) and (c) show the corresponding contribution of DC and AC components in the response, respectively. (d) Sample time-response at $Y/Na = 1.4$ and $\Omega = 0.1Hz$, showing an AC dominated response of AC term. (e) Another Sample time-response at $Y/Na = 0.8$ and $\Omega = 1Hz$, showing a DC dominated response.

It can be seen that at some regions of base excitation frequency and amplitude, the TR index is high and dominated by the AC component. Figure 2.12(d) shows such an example where $Y/Na = 1.4$ and $\Omega = 0.1Hz$. In contrary, there are some combinations of excitation frequencies and amplitudes by which the DC components dominates, and an example corresponding to $Y/Na = 0.8$ and $\Omega = 1Hz$ is shown in Figure 2.12(e). The significant drift in the time response can drive the TR index to near one. Therefore, unlike other QZS vibration isolators with symmetric force-displacement relationships, drift plays a considerable role in the system dynamics. One needs to consider its effect carefully in order to properly explain the base excitation isolation.

Another important factor that needs to be considered is the limit of achievable displacement of the fluidic origami. The length of fluidic origami is restricted by the kinematics of folding, that is, the structure can only be stretched up to the fully deployed state ($\theta_I = 0$ shown in Figure 2.2(b)). Therefore, we have to ensure that the maximum relative displacement $u(t)$ of the end mass does not exceed the maximum length of fluidic origami.

As the first step to understand the effect of such a geometric constraint due to folding, we show that the maximum allowed displacement from the QZS configuration to the fully deployed configuration is linearly related to the number of unit cells in a fluidic origami tubular channel. It can be shown that the folding angle at the QZS configuration (θ_{QZS}) does not depend on the number of cells. Therefore, from Equation 2.1 we can write the maximum possible displacement from QZS to the fully deployed state as:

$$\Delta x = N \left(\frac{2b \tan \gamma_{\mathrm{I}}}{\sqrt{1 + \tan \gamma_{\mathrm{I}}^2}} - \frac{2b \cos \theta_{QZS} \tan \gamma_{\mathrm{I}}}{\sqrt{1 + \cos \theta_{QZS}^2 \tan \gamma_{\mathrm{I}}^2}} \right), \tag{2.28}$$

Based on Equation 2.28(28), the relationship between the maximum possible displacement (Δx) and the number of cells (N) is linear (Figure 13(a)). This result can then be applied to the parametric analysis result shown in Figure 2.12(a) as a constraint. That is, if the maximum end mass displacement is larger than Δx at some frequencies and base excitation magnitudes, the fluidic origami is no longer considered feasible for vibration isolation. Figure 13(b) shows such a region where the end mass displacement exceed the constraint of folding. We can see that based excitation frequency and amplitude combinations that leads to $TR > 1$ is indeed unachievable. In another words, as long as the fluidic origami is not stretched to its maximum length, it can always perform well as a low-frequency base excitation isolator. Moreover, fluidic origami with more unit cells in its tubular channel can isolate base excitation with larger amplitudes.

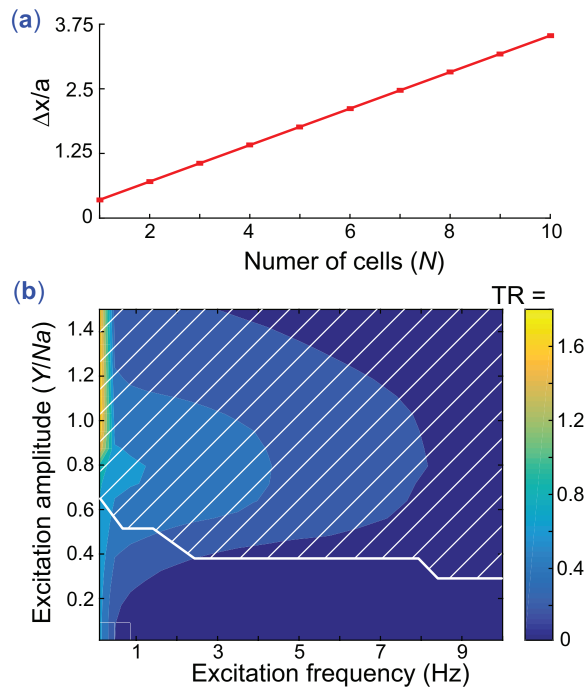

Figure 2.13: (a) The linear relation between the maximum possible displacement Δx and the number of cells (N). (b) The shaded regions show the excitation magnitudes and frequencies at which maximum relative displacement of the end mass exceeds the folding limitation of the fluidic origami.

2.6 Summary and Conclusion

This study analytically and experimentally examines a pressurized origami cellular structure with an asymmetric quasi-zero stiffness (QZS) property, and investigates its use in low-frequency vibration isolation. Fluidic origami consisting of stacked Miura-Ori sheets has been shown to exhibit many unique and interesting mechanical properties related to stiffness. This research demonstrates that by sealing the pressurized structure, it is possible to acquire quasi-zero stiffness (QZS) property due to the intricate and nonlinear relationship between folding and internal volume change.Design guidelines for achieving QZS are presented for two different cases: One is identical stacked Miura-Ori sheets (ISMO) and the other is non-identical stacked Miura-Ori (NISMO). A proof-of-concept prototype was tested to verify the existence of desired QZS property. The appropriate fluidic origami designs are then used for a comprehensive dynamic study of low-frequency base-excitation isolation. In particular, this study closely examines the effects of inherent asymmetry in the force-displacement relationships of fluidic origami. Via comparing the approximation solutions based on harmonic balance method using both symmetric and asymmetric polynomial fittings, we show that the asymmetry in force-displacement curve can 1) induce a significant drift (DC component) in the steady state time response and 2) increase the transmissibility index at high excitation amplitude and low frequency. These phenomena must be carefully considered for evaluating the base excitation isolation performance. Moreover, the kinematic constraint due to folding is also considered to ensure that fluidic origami will not be stretched beyond its maximum possible length. We show that QZS property from fluidic origami can indeed provide effective base ex-citation isolation at low-frequencies. The internal pressure of fluidic origami can be adjusted to accommodate changes in the end mass, making the cellular structure tunable. Results of this study can lay the foundation of origami-inspired metamaterials and meta-structures with embedded dynamic functionalities. Moreover, investigations into the asymmetry in force-displacement relationship provide valuable insights for many other QZS structures with similar properties.

In the next two chapters we investigate another dynamic application of origami folding. In chapter 3, we study the potential effects of using a generic nonlinear spring on the performance of a jumping mechanism. Then in chapter 4, we use our findings from chapter 3 and replace the generic theoretical nonlinear spring with an elastic Tachi-Miura polyhedron (TMP) bellow origami structure and optimize its design to achieve the best jumping performance.

Chapter 3

The effect of Nonlinear Springs in Jumping Mechansims

3.1 Abstract

This research investigates the potential effects of utilizing nonlinear springs on the performance of robotic jumping mechanisms. As a theoretical example, we study dynamic characteristics of a jumping mechanism consisting of two masses connected by a generic nonlinear spring, which is characterized by a piecewise linear function. The goal of this study is to understand how the nonlinearity in spring stiffness can impact the jumping performance. To this end, non-dimensional equations of motion of the jumping mechanism are derived and then used extensively for both analytical and numerical investigations. The nonlinear force-displacement curve of the spring is divided into two sections: compression and tension. We examine the influences of these two sections of spring stiffness on the overall performance of the jumping mechanism. It is found that compression section of the nonlinear spring can significantly increase energy storage and thus enhance the jumping capabilities dramatically. We

also found that the tension section of the nonlinear force-displacement curve does not affect the jumping performance of the center of gravity, however, it has a significant impact on the internal oscillations of the mechanism. Results of this study can unfold the underlying principles of harnessing nonlinear springs in jumping mechanisms and may lead to the emergence of more efficient hopping and jumping systems and robots in the future.

3.2 Introduction

Studying legged robots is a century-old branch of robotic studies [81]. The aspiration of replicating the omnipresent legged animals that are able to overcome the unfavorable environmental conditions have engaged more and more robotic researchers in this field [82, 83]. However, the dynamics of legged robots are quite complicated compared to the stationary and wheeled mobile robots, especially due to the impact with the ground. This, along with several other issues such as complex nonlinear control, has led researchers to focus on single-legged systems that possess a much simpler configuration [84]. The locomotion of single-legged robotic systems is achieved by hopping. Hopping is the process of utilizing stored energy of the system to jump and it can occur repeatedly via storing and then reusing the energy during landing [85]. Despite its relative simplicity, hopping is still a useful means of locomotion especially in terrains that are inaccessible to wheeled or tracked systems [84]. It can also be very advantageous in situations when there is a sudden need for reflex, e.g. frogs or bush-babies take advantage of their innate hopping ability to flee from predators. Recently, there have been plenty of valuable researches on different aspects of jumping locomotion, from proposing novel hopping mechanisms [86–89] to various control strategies for stabilizing the dynamic motion [90–93].

One can discern three pivotal topics of research among the recent investigations on hopping or jumping robots: Actuators, energy storage, and dynamics of hopping. Actuator has always been one of the main concerns of researches in this field. Since the very first hopping mechanism prototype proposed by Matsuoka [94], researchers have been seeking more efficient actuators that can provide a low-cost, lightweight and safe actuation. Several prominent researches in the field of hopping robots have been inspired by the mechanism designed by Raibert [81, 95], which utilizes hydraulic and pneumatic actuators. Other works utilized electric actuators that are cleaner, safer, less expensive, and more appropriate for autonomous robots. Besides actuators, energy storage also plays a significant role in the performance of hopping robots. All of the existing jumping mechanisms rely on the instant release of the stored energy to realize jumping [89], and there are several approaches to achieve the required energy storage. Implementing traditional springs, such as compression, extension, or torsion springs, is probably the most popular method. Compressed air is another method of energy storage [89] that has been used in rescue [96] and patrol robots [97]. Several researchers have also implemented specialized elastic elements or customized springs [89] for storing energy. For example, the MIT microbot utilizes two symmetrical carbon fiber strips with dielectric elastomer actuators [98, 99], Jollbot deforms its spherical shape to store energy [100], and another compact jumping robot takes advantage of an elastic strip to form closed elastica actuated by two revolute joints [101, 102].

The dynamics of hopping robots is another important branch of robotic research for deciphering the underlying principles of hopping. Hopping mechanisms exhibit a nonlinear dynamic behavior, naturally. This is especially due to the impact with the ground and the presence of distinct stance and flight phases with sudden transitions [84]. The governing dynamics of these two main phases are fundamentally different. Researchers have conducted several studies on the nonlinear dynamics of hopping. For example, M'Closkey and Burdick investigated forward running dynamics of a 2-DOF hopper using a Poincare' return map [103]. Koditschek and Buehler modified the Raibert's model and studied two discrete dynamical models of this vertical hopper using linear and nonlinear spring [91]. The nonlinear springs can introduce unique and desirable dynamic characteristics to the hopping mechanisms. They were utilized in several jumping prototypes and their effects on the overall dynamic performances were assessed. For example, Yamada et al. proposed the idea of using snap-through buckling – an archetypical nonlinear stiffness property – of a closed elastica for jumping robots [101, 102]. In another study, Fiorini and Burdick implemented a linear spring in a 6-bar geared mechanism to generate an effective nonlinear spring behavior and investigated its effects on overcoming the pre-mature take-off [104]. In addition, through a preliminary study, Armour investigated the effect of negative stiffness on jumping [100]. However, apart from these experimental case studies, there is a lack of any comprehensive analysis on the potential benefits of utilizing nonlinear springs to improve the performance of the hopping and jumping mechanisms. Such a gap in our knowledge prevents us from building hopping robots that can effectively exploit nonlinear springs. Therefore, the aim of this research is to fill this void by analyzing the performance of a generic jumping mechanism consisting of two identical mass-es connected by a nonlinear spring. To this end, we use a piecewise linear function, as an archetype example, to characterize the force-displacement relationship of the nonlinear springs. The outcome of this research can provide guidelines for robotic researchers and foster more efficient hopping mechanisms and robots in the future.

The rest of this paper is organized as follows. In section 3.3, we introduce the generic jumping mechanism utilizing a nonlinear spring as the energy storage element. Then we derive the non-dimensional equations of motions that govern the jumping phenomenon. In section 3.4, we analyze the potential merits of utilizing a nonlinear spring element through an extensive study based on numerical simulations and analytical reasoning. Finally, section 3.5 concludes the paper with a summary and discussion.

3.3 Jumping Mechansim and its Equations of Motion

The jumping mechanism (figure 3.1) investigated consists of two identical masses connected by an elastic element exhibiting non-linear stiffness characteristics. Energy storage in the system occurs through exerting an input force using an actuator on the top mass to deform the elastic element. The reaction force-displacement relationship of the nonlinear spring can be generally represented by a $C^n(n >= 0)$ continuous curve. However, in order to avoid introducing unnecessary complexities, we focus on a generic piecewise linear C^0 curve to describe the nonlinear stiffness properties. Despite its relative simplicity, the C^0 curve is a useful tool for approximating many nonlinear stiffness properties commonly used for engineering applications, e.g. negative stiffness [69] and quasi-zero stiffness [63] characteristics. Figure 3.2(a) shows the C^0 piecewise linear force-displacement curve that will be used in this study. The displacement axis is represented by y, where $y = Y_2 - Y_1 - l_0$. Y_1 and Y_2 are the height of the two masses with respect to the ground, and l_0 is the free length of the nonlinear spring. This curve consists of four linear sections with different stiffness coefficients (k_1 to k_2). We also consider the structural and actuation limit that can constrain the problem. The structural limit (H) is the maximum relative displace-

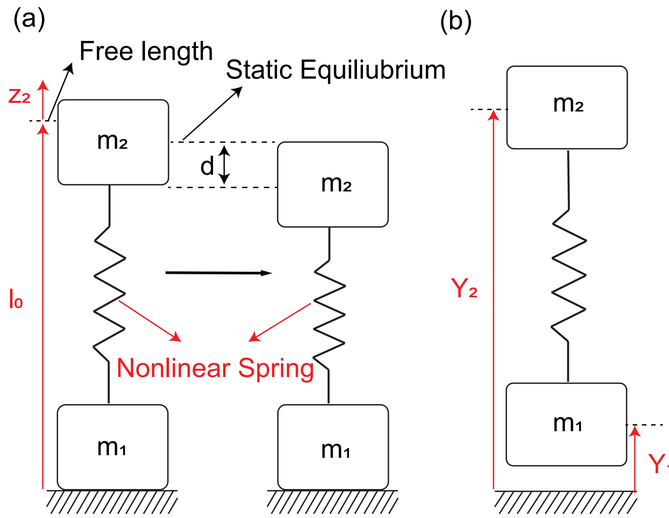

Figure 3.1: Schematic of the jumping mechanism in (a) pre-jump phase of motion and (b) post-jump phase of motion.

ment between the two masses in order to compress the spring and store an initial energy. The actuation limit is the maximum amount of external force (f_c) the actuator can provide. Moreover, the force-displacement curve can be divided in to two separate regions: The compression region (negative displacement), where the spring is compressed; and the tension region (positive displacement), where the spring is under tension. This separation allows us to study the energy storage (compression) and jumping dynamics (tension) in a more systematic approach, as we will see later in section 3.4.

Knowing the reaction force of the nonlinear spring, we can now investigate the dynamic behavior of the system. The dynamic motion of the jumping mechanism can be divided into two different phases: 1) pre-jump phase and 2) post-jump phase. In order to just focus on the potential effects of the nonlinear spring, we assumed that the masses are equal: $m_1 = m_2 = m$. In the following two sections, we study the motion of the system in these two phases.

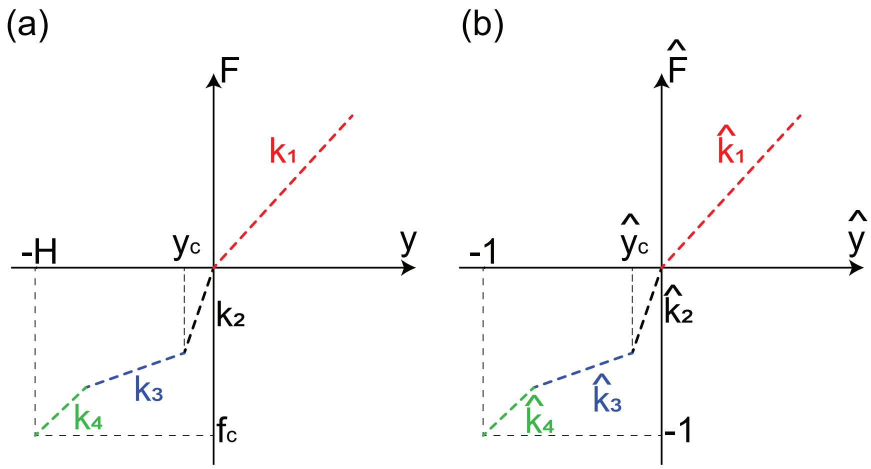

Figure 3.2: (a) Piecewise linear reaction force-displacement curve of spring with structural and actuation limits. (b) Non-dimensional force-displacement curve.

3.3.1 Pre-Jump Phase of Motion

The pre-jump phase (figure 3.1(a)) occurs for all time prior to the bottom mass m_1 leaving the ground. During this phase, an input actuation force displaces up to a certain initial position (d). Once the input force is removed, the reaction force of the spring accelerates the upper mass upward. The governing equation of motion during this phase can be represented by:

$$m\ddot{Y}_2 = -F(Y_2 - l_0) - mg, \tag{3.1}$$

where m is the mass of the upper body, $F(Y_2 - l_0)$ is the reaction force of the spring, and $\ddot{Y}_2$ and Y_2 represent the acceleration and position of the upper mass (relative to the ground), respectively. We define $k^* = f_c/H$, the ratio between actuation limit and structural limit, as a reference linear spring coefficient. Equation 3.1 can be non-dimensionalized as follows:

$$\frac{d^2\hat{Y}_2}{d\tau^2} + \hat{F}(\hat{Y}_2 - \hat{l}_0) = -\hat{G}, \tag{3.2}$$

where, $\hat{Y}_2 = Y_1/H$, $\tau = t\omega$, $\omega = \sqrt{k^*/m}$, $\hat{F}_2 = F/f_c$, $\hat{l}_0 = l_0/H$, and $\hat{G} = mg/f_c$. We can also non-dimensionalize the stiffness coefficients: $\hat{k}_i = k_i/k^*$, $(i = 1, 2, ..., 4)$.

3.3.2 Post-Jump Phase of Motion

In order for a jump to be possible, the jumping mechanism must be capable of surpassing the gravitational force once the displacement in the non-linear elastic element has become positive. That is, the restoring force of the non-linear elastic element acting on the lower mass must exceed its weight. The jumping occurs when $\hat{Y}_2 = \hat{Y}_{2,jump}$, where:

$$\hat{F}(\hat{Y}_{2,jump} - \hat{l}_0) = \hat{G}. \tag{3.3}$$

The airborne or post-jump phase of the motion is illustrated in figure 3.1(b). Once the bottom mass has left the ground, the governing system of coupled equations of motion can be defined as:

$$\begin{aligned} m\ddot{Y}_1 &= F(Y_2 - Y_1 - l_0) - mg, \\ m\ddot{Y}_2 &= -F(Y_2 - Y_1 - l_0) - mg. \end{aligned} \tag{3.4}$$

Following the same procedure of section 3.3.1, we can derive the non-dimensional system of equations as follows:

$$\begin{aligned} \tfrac{d^2\hat{Y}_1}{d\tau^2} &= F(\hat{Y}_2 - \hat{Y}_1 - \hat{l}_0) - \hat{G}, \\ \tfrac{d^2\hat{Y}_2}{d\tau^2} &= -F(\hat{Y}_2 - \hat{Y}_1 - \hat{l}_0) - \hat{G}. \end{aligned} \tag{3.5}$$

The initial conditions of equation 3.5 can be extracted from the solution of pre-jump phase (equation 3.2). In the next section, we present the numerical simulation results of solving the equations of motion.

3.4 Studying The Effect of Force-Displacement Curve of the Nonlinear Spring on the Jumping Performance

Jumping occurs when the upper mass in figure 3.1 reaches a specific height (equation 3.3), as we mentioned earlier. At this point, the lower mass loses its contact with the ground and jumps off the ground. At the transition stage when the jump starts, most of the stored energy in the spring (E_0) is converted to the kinetic energy of the upper mass and some portion will be converted to gravitational potential energy. We assume that the whole mechanism is subject to conservative forces and no damping is involved. Therefore, during the post jump phase when both of the masses are airborne, the total energy of the system (aka. kinetic energy + spring potential energy + gravitational potential energy) will be conserved. Nevertheless, we expect that two different masses of the mechanism exhibit complex behaviors after jumping due to the presence of a nonlinear spring element. Therefore, it is important to study both the responses of the masses individually and the movement of the overall center of gravity in order to obtain a clear understanding of the dynamic behaviors. To this end, we start our investigation by analyzing the effect of the stored energy on the jumping performance. The stored energy is related to the compression (negative displacement) section of the force-displacement curve. Therefore, the first objective would be to gain an accurate comprehension of the underlying principles that regulate the relation between the compression section of the force-displacement curve and the jumping phenomenon (section 3.4.1). In order to acquire a comprehensive tool for designing a jumper with a desired functionality, we also investigate the effect of the tension (positive displacement) section of the force-displacement curve on the jumping

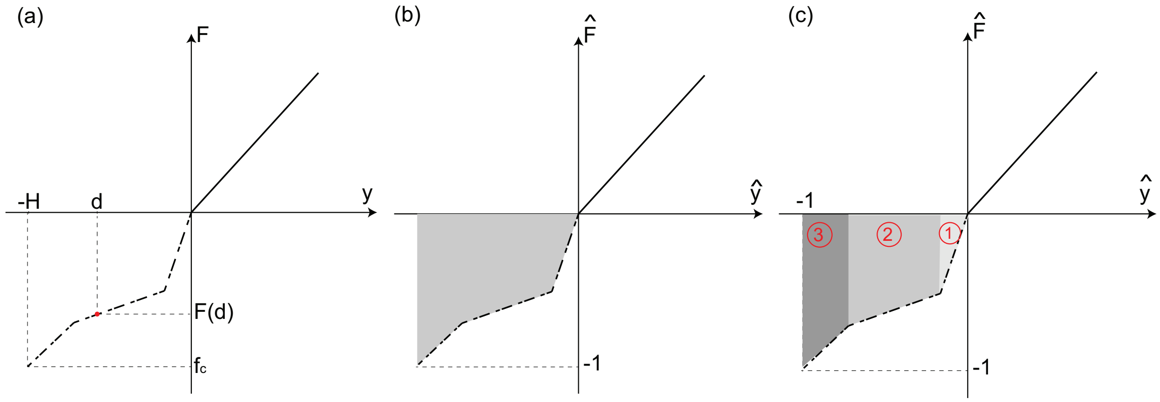

Figure 3.3: (a) Reaction force-displacement curve of the spring with an initial displacement (d). (b) Non-dimensional force-displacement curve of the spring with the shaded area representing the initial stored energy. (c) Three constituent areas of the shaded region.

behavior of the overall center of gravity and both masses (section 3.4.2).

3.4.1 Energy Storage and the Compression (Negative Displacement) Section of the Force-Displacement Curve

Storing energy in the system, shown in figure 3.1, is achieved by compressing the spring element to an initial displacement. The stored energy (E_0) at this stage is equal to the amount of work (W_{ext}) that has been done on the spring to compress it. The relationship between the stored energy and the restoring force of the spring, if it is compressed from the free length, can be expressed as:

$$E_0 = W_{ext} = \int_0^d F(y).\, dy, \tag{3.6}$$

where d is the displacement of the spring from the free length and $F(y)$ represents the restoring force of the spring (figure 3.3(a)). As we mentioned in section 3.3, a piecewise linear force-displacement curve (figure 3.2) is an advantageous tool for representing most of the nonlinear stiffness properties that have been used for engineering applications. Therefore, in this section we focus on the generic piecewise linear force-displacement curves constrained by the actuation and structural limits (figure 3.2(b)) to study the effect of nonlinear spring elements on the jumping phenomenon. To obtain a better insight into the energy storage function, we first non-dimensionalize equation 3.6 based on the structural and actuation limit so that,

$$\hat{E}_0 = \int_0^{\hat{d}} \hat{F}(\hat{y}).\, d\hat{y}, \tag{3.7}$$

where: $\hat{E}_0 = \frac{E_0}{\frac{1}{2}k^* H^2}$, $\hat{d} = \frac{d}{H}$.

Two important factors affect the amount of stored energy in the mechanism, namely initial displacement and the force-displacement function. It is clear that for a given force-displacement relationship, one can store the maximum amount of energy when the mechanism is initially compressed all the way up to its structural limit, that is $\hat{d} = -1$.

Meanwhile, shape of the force-displacement curve plays a significant role as well. Consider an arbitrary piece-wise linear curve in the negative displacement region, bounded by the two structural and actuation limits ($\hat{d} = -1$ and $F(d) = -1$, figure 3.3(b)). The stored energy of the system is equal to the area between the $\hat{y}$-axis and the $F(\hat{y})$ curve (shaded region in figure 3.3(b)). The area can be represented by the summation of three constituent areas, one triangle (A_1) and two trapezoids (A_2 and A_3) (figure 3.3(c)), as follows:

$$\hat{E}_0 = A_1 + A_2 + A_3. \tag{3.8}$$

The compression section of the generic force-displacement curve consists of

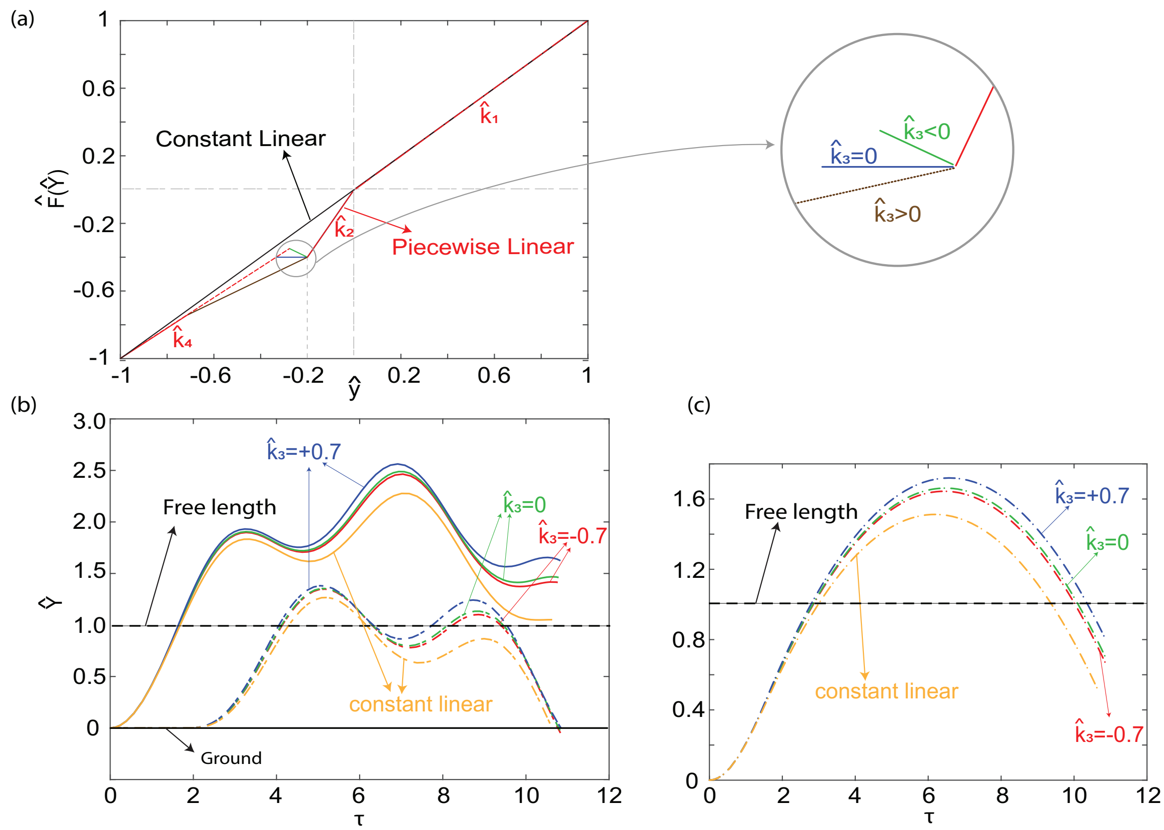

Figure 3.4: (a) Three different piecewise linear force-displacement curves, with positive, negative and zero $\hat{k}_3$ stiffness coefficients. (b) Vertical displacement of the upper mass (solid line) and lower mass (dashed line). (c) Vertical displacement of the center of gravity.

three piecewise linear curves with three different non-dimensional stiffness coefficients: $\hat{k}_2$, $\hat{k}_3$ and $\hat{k}_4$. The magnitudes of these three stiffness coefficients can be varied to examine the effect of energy storage on the jumping behavior. Figure 3.4(a) demonstrates three different piecewise linear force-displacement curves with a positive, negative, and zero $\hat{k}_3$ coefficient, respectively. Another "constant linear" force-displacement curve with stiffness coefficient $\hat{k} = 1$ is also plotted in this figure for reference. Constant linear force-displacement curve is a linear curve with a constant stiffness throughout its domain. Indeed, this constant linear force-displacement relationship can lead to the largest possible stored energy among all of the linear stiffness curves bounded by the structural and actuation limit. There-fore, it represents the best possible linear spring. We assume the three piecewise linear curves share the same $\hat{k}_1$, $\hat{k}_2$ and $\hat{k}_4$ stiffness coefficients and $\hat{y}_c$. In addition, we choose the tension stiffness of all three piecewise linear springs to be the same as the fully linear spring, that is $\hat{k}_1 = k = 1$, in order to compare the performance of nonlinear and linear springs. All of the piecewise linear curves are chosen to provide more stored energy than the constant linear spring.

We used MATLAB ODE45 solver to solve the system of ordinary differential equations governing the motion, presented by equation 3.2. Initial condition of the upper mass is chosen as $[\hat{Y}_2 = 0, \dot{\hat{Y}}_2 = 0]$, where $\hat{Y}_2$ is measured from the ground. Additionally, Initial conditions of the post-jump phase of motion presented by equation 3.5, is extracted from the solution of pre-jump phase (governed by equation 3.2).

Figure 3.4(b) and 3.4(c) show the vertical displacement of both masses and the center of gravity. Based on the results, it can be seen that the jumping mechanisms featuring piecewise linear springs outperform the one with constant linear springs in terms of jumping distances (up to 14 precent increase). Furthermore, both of the masses and also the center of gravity are able to reach higher heights when $\hat{k}_3$ is positive. This is because the mechanisms with positive $\hat{k}_3$ stiffness coefficients are able to store more energy due to the larger area between the displacement axis and the force-displacement curve (aka. larger A_2 in figure 3.3).

Besides jumping height, we also compare the energy efficiency of these mechanisms. The ability of reaching higher heights in piecewise linear springs stems from their capability of storing more energy in the system. Therefore, it is important to analyze the efficiency of utilizing this additional energy. We define the energy efficiency of the mechanism as the ratio between the maximum gravitational potential energy of the overall center of gravity ($\max(PE_{CG})$) and the initial stored energy

(E_0):

$$\eta = \frac{\max(PE_{CG})}{E_0} \times 100 \tag{3.9}$$

Figure 3.5(a-d) shows the gravitational potential energies of three different systems presented in figure 3.4. Also shown in this figure is the initial stored energy level. Based on these results, we can observe that the mechanism utilizing the piecewise linear spring exhibit a slight drop in energy efficiency (¡2 percent for the spring with positive $\hat{k}_3$).

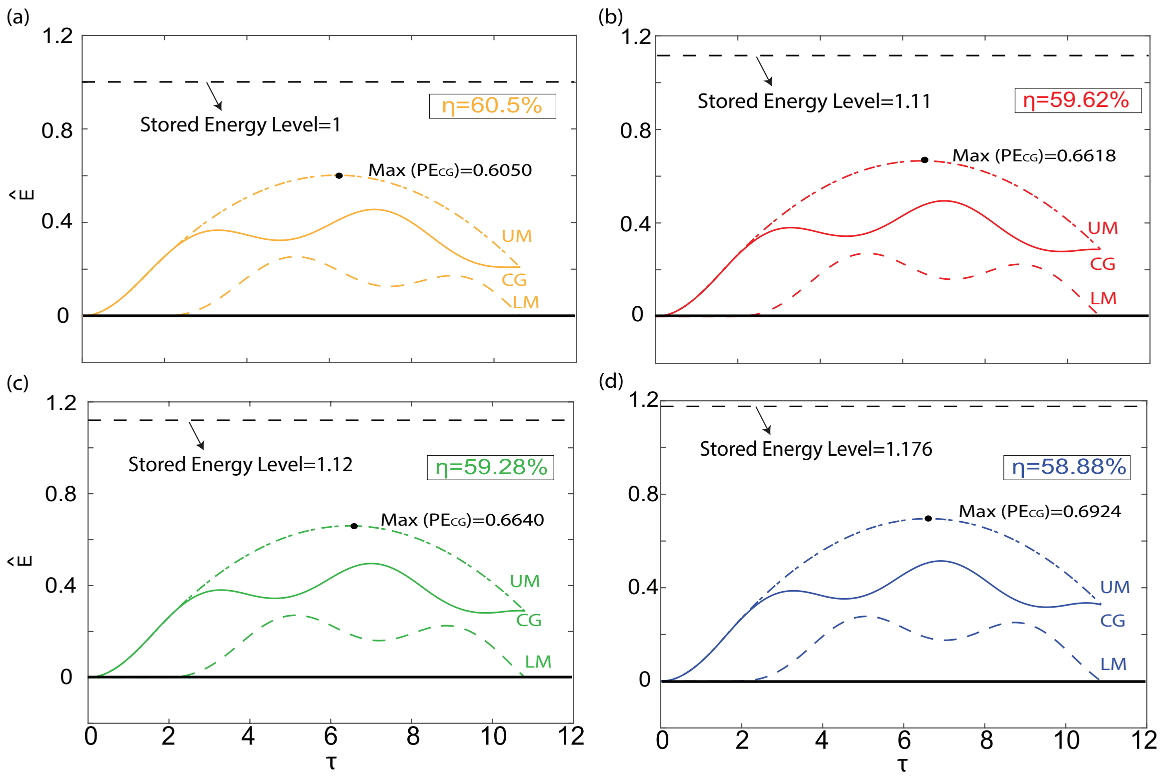

Figure 3.5: (a) Gravitational potential energy levels of the upper mass (UM), lower mass (LM) and center of gravity (CG) for constant linear stiffness (a); and three piecewise linear cases (b-d). The three piecewise linear force-displacement curves feature the same $\hat{k}_1 = 1$, $\hat{k}_2 = 2$, $\hat{k}_4 = 0.9$, $\hat{y}_c = -0.2$. But they have different $\hat{k}_3$ values: (b) $\hat{k}_3 = -0.7$, (c) $\hat{k}_3 = 0$ and (d) $\hat{k}_3 = +0.7$.

We further analytically investigate this efficiency drop for the mechanisms with higher initial stored energy. Consider the initial stored energy of a mechanism utilizing a constant linear spring with stiffness coefficient $\hat{k}_1 = 1$. We can represent the non-dimensional initial stored energy of the system by E_0, where:

$$\hat{E}_0 = \frac{E_0}{E_{0,\, linear\, spring}} = \frac{E_0}{\frac{1}{2}k^* H^2} = 1 + \hat{e}, \tag{3.10}$$

where $\hat{e}$ ($0 <= \hat{e} <= 1$) represents the additional non-dimensional stored energy by utilizing a nonlinear properties in the compression section of the force-displacement curve. One can represent the difference between the efficiencies of the nonlinear system and the linear system by the following equation:

$$\Delta\eta = \eta_{linear} - \eta_{nonlinear} = \left(\frac{max(PE_{CG,linear})}{\hat{E}_{0,linear}} - \frac{max(PE_{CG,nonlinear})}{\hat{E}_{0,linear} + \hat{e}} \right) \times 100. \tag{3.11}$$

By considering the fact that the additional energy due to utilizing a nonlinear spring will be converted to the kinetic energy of the system at the free length and with some mathematical work, one can show that:

$$\eta_{linear} - \eta_{nonlinear} = \left(2\hat{G}\frac{\hat{e}}{1 + \hat{e}} \right) \times 100. \tag{3.12}$$

This equations implies that the efficiency drop of a nonlinear mechanism follows a hyperbolic relationship with respect to the additional energy $\hat{e}$. If more energy is stored in the pre-jump phase via using nonlinear springs, jumper mechanism becomes less efficient. However, it is important to point out that this drop in efficiency is linearly dependent on $\hat{G}$, which is the ratio of the jumping mechanism mass over the maximum spring reaction force (aka. actuation limit). For a typical jumping mechanism, this ratio is designed to be small and significantly less than one. In our case study, $\hat{G} = 0.1$. As a result, the magnitude of the efficiency drop from using nonlinear spring is small (less than 2 percent in our case studies). The benefit of significantly higher jump distance (up to 14 percent increase) easily outweigh the small sacrifice in terms of efficiency.

Therefore, our results elucidate that implementing nonlinear spring can significantly increase the jumping height by providing a pathway to store more energy under the actuation and structural limits. Although these results are based on a C^0 piecewise linear force-displacement curve, the principles can be directly extended to any $C^n(n >= 1)$ nonlinear curves.

3.4.2 Tension (Positive Displacement) Section of the Force-Displacement Curve

In the previous section, we analyzed the effect of utilizing nonlinear properties to increase the energy storage in the compression section (negative displacement) of the force-displacement curve. In order to fully comprehend the effect of nonlinear springs on jumping, we also need to study the tension (positive displacement) section of the force-displacement curve. In this section, we consider three different stiffness profiles (figure 3.6). The compressive part of these force-displacement curves are same as the one in the previous section with positive $\hat{k}_3(= +0.7)$; while the tension parts of these curves ($\hat{k}_1$) differ. Three different $\hat{k}_1$ values are chosen: $\hat{k}_1 = 1$ represents a spring with the same tension stiffness as the constant linear spring discussed in the previous section. $\hat{k}_1 = 0.5$ and $\hat{k}_1 = 5$ represent springs with softer and stiffer (with respect to $\hat{k}_1 = 1$) tension stiffness, respectively (figure 3.6).

Figure 3.7(a) shows the vertical displacement of both of the masses according to the three different tension stiffness coefficients. Based on the results of figure 3.7(c), we can observe that changing the tension (positive displacement) stiffness of

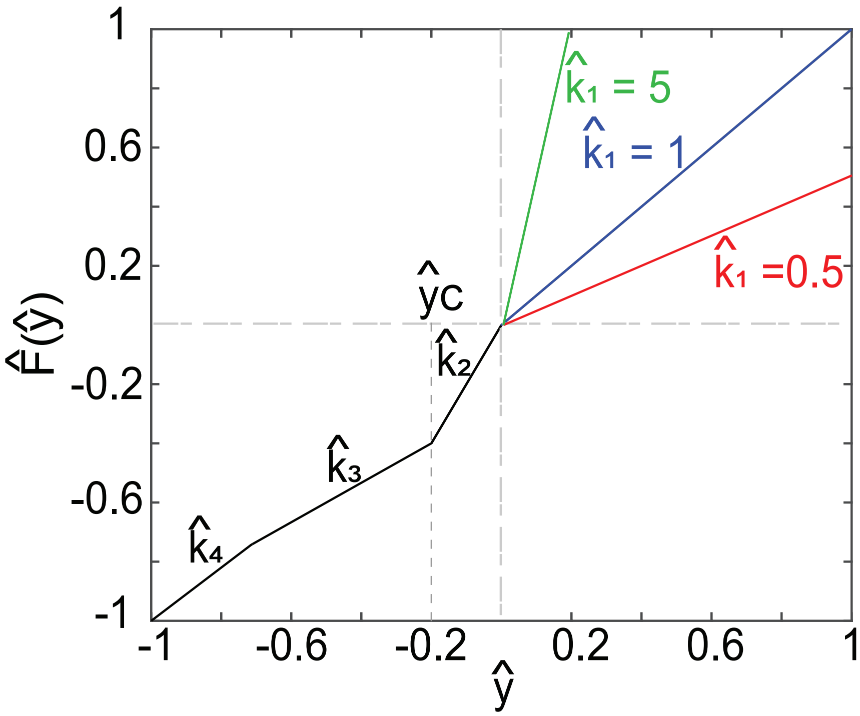

Figure 3.6: Three different piecewise linear force-displacement curves with the same compression section ($\hat{k}_2 = 2$, $\hat{k}_3 = +0.7$, $\hat{k}_4 = 0.9$, $\hat{y}_c = -0.2$) but different tension stiffness coefficients.

the force-displacement profile does not affect the maximum height that the center of gravity of the mechanism can reach. On the other hand, the stiffness of the tension section has a significant effect on the oscillations of two constituent masses of the mechanism. Based on the results of figure 3.7(b), we can observe that increasing the tension stiffness will decrease the amplitude of the internal oscillations of the mechanism, but increases their frequency. In the next section, we try to qualitatively explain these observations analytically by performing a modal analysis on a simplified system.

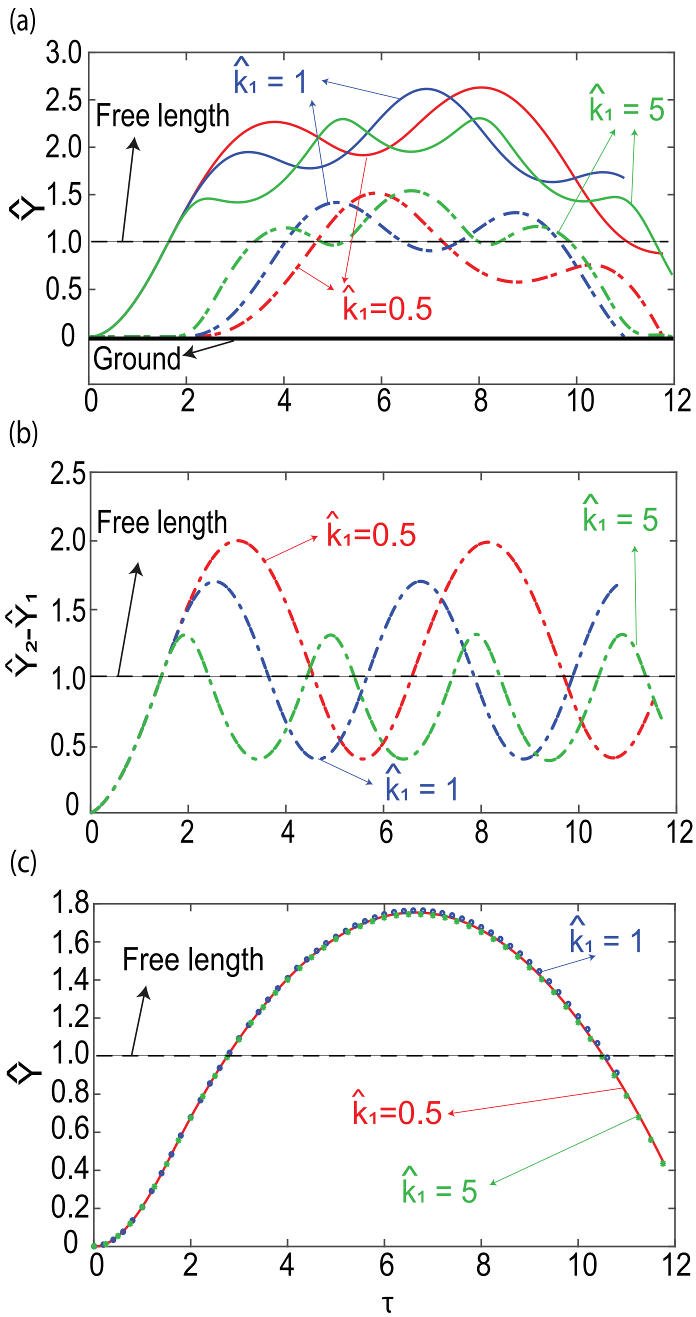

Figure 3.7: (a) Vertical displacement of the upper mass (solid line) and the lower mass (dashed line). (b) Internal oscillations of the jumping mechanism. (c) Vertical displacement of the center of gravity. Colors are the same as in figure 3.6

3.4.3 The Effect of Tension Stiffness on the Jumping Motion of the Center of Gravity and the Internal Oscillations

Figure 3.1(b) shows the jumping mechanism at its airborne phase. We derived the equations of motion for the case where $m_1 = m_2 = m$ (equation 3.5). At this section we consider a more general case where the upper and the lower mass can be different. We can show that the motion of the both masses is governed by the following system of equations:

$$\begin{aligned} m_1\ddot{z}_1 &= F(z_2 - z_1) - m_1 g \\ m_2\ddot{z}_2 &= -F(z_2 - z_1) - m_2 g, \end{aligned} \tag{3.13}$$

where z_2 and z_1 are measured from the free length and the ground, respectively and $F(z_2 - z_1)$ is a nonlinear function. Here, we simply use the tension stiffness k_1 to represent the stiffness characteristics around the equilibrium ($z_2 = 0$). This is a reasonable simplification because the post-jump phase of motion initially occurs when the spring is under tension. Therefore, we can simplify the equations of motion in a linear matrix form:

$$\begin{pmatrix} \ddot{z}_1 \\ \ddot{z}_2 \end{pmatrix} = \begin{pmatrix} -\frac{k_1}{m_1} & \frac{k_1}{m_1} \\ \frac{k_1}{m_2} & \frac{k_1}{m_2} \end{pmatrix} \begin{pmatrix} z_1 \\ z_2 \end{pmatrix} + \begin{pmatrix} -g \\ -g \end{pmatrix} \equiv \ddot{\vec{Z}} = [K]\,\vec{Z} - \vec{g}. \tag{3.14}$$

We can find the eigenvalues and the corresponding eigenvectors of the stiffness matrix ($[K]$) as follows:

$$\begin{aligned} \lambda_1 = 0,\ \vec{v}_1 &= \begin{pmatrix} 1 \\ 1 \end{pmatrix} \\ \lambda_1 = -k_1\tfrac{m_1+m_2}{m_1 m_2},\ \vec{v}_2 &= \begin{pmatrix} -m_2/m_1 \\ 1 \end{pmatrix}. \end{aligned} \tag{3.15}$$

One can show that, by diagonalization:

$$[K] = [V][\Lambda][V]^{-1}, \tag{3.16}$$

where:

$$[V] = \begin{pmatrix} \vec{v}_1 & \vec{v}_2 \end{pmatrix} = \begin{pmatrix} 1 & -\frac{m_2}{m_1} \\ 1 & 1 \end{pmatrix}, [\Lambda] = \begin{pmatrix} \lambda_1 & 0 \\ 0 & \lambda_2 \end{pmatrix} = \begin{pmatrix} 0 & 0 \\ 0 & -k_1\frac{m_1+m_2}{m_1 m_2} \end{pmatrix}. \tag{3.17}$$

Therefore, we can update equation 3.14 as follows:

$$\ddot{\vec{Z}} = [V][\Lambda][V]^{-1}\vec{Z} - \vec{g}. \tag{3.18}$$

Pre-multiply both sides of equation 3.18 by V^{-1}:

$$[V]^{-1}\ddot{\vec{Z}} = [\Lambda][V]^{-1}\vec{Z} - [V]^{-1}\vec{g}, \tag{3.19}$$

and define $\vec{U} = [V]^{-1}\vec{Z}$. That is:

$$\vec{U} = \begin{pmatrix} u_1 \\ u_2 \end{pmatrix} = [V]^{-1}\vec{Z} = \begin{pmatrix} \frac{m_1 z_1 + m_2 z_2}{m_1+m_2} \\ \frac{m_1}{m_1+m_2}(z_2 - z_1) \end{pmatrix}. \tag{3.20}$$

Based on equation 3.20, we can observe that u_1 and u_2 represent the position of the center of gravity and the magnitude of the internal oscillatory motion of the mechanism, respectively. Using $\vec{U}$ as the new state variable, we can update equation 3.18:

$$\ddot{\vec{U}} = [\Lambda]\vec{U} - [V]^{-1}\vec{g}. \tag{3.21}$$

By substituting and matrices into equation 3.21, we have:

$$\begin{pmatrix} \ddot{u}_1 \\ \ddot{u}_2 \end{pmatrix} = \begin{pmatrix} 0 & 0 \\ 0 & -k_1\frac{m_1+m_2}{m_1m_2} \end{pmatrix} \begin{pmatrix} u_1 \\ u_2 \end{pmatrix} - \begin{pmatrix} \frac{m_1}{m_1+m_2} & \frac{m_2}{m_1+m_2} \\ -\frac{m_1}{m_1+m_2} & \frac{m_1}{m_1+m_2} \end{pmatrix} \begin{pmatrix} g \\ g \end{pmatrix}. \tag{3.22}$$

This means that:

$$\begin{aligned} \ddot{u}_1 &= -g\left(\tfrac{m_1}{m_1+m_2} + \tfrac{m_2}{m_1+m_2}\right) = -g \\ \ddot{u}_2 &= -k\left(\tfrac{m_1+m_2}{m_1m_2}\right)u_2. \end{aligned} \tag{3.23}$$

We can clearly see that the acceleration of the center of gravity is independent of the stiffness of the tension section and is always equal to $-g$. Therefore, we can conclude that, even with different tension stiffness coefficients, the center of gravity movement of these mechanisms will be the same as long as the initial stored energy based on compression section is the same. We also observed this for the actual nonlinear system (figure 3.7(c)). We can also derive the frequency of the internal oscillations of the simplified mechanism as follows:

$$\Omega = \sqrt{\frac{m_1+m_2}{m_1m_2}k_1}. \tag{3.24}$$

Although equation 3.24 is derived for a simplified mechanism and does not provide the exact frequency of oscillations for the nonlinear system, it suggests that the internal oscillations of the mechanism depend on the tension stiffness, which is in agreement with the numerical simulation results, based on the actual nonlinear system (figure 3.7(b)).

Therefore, although changing the stiffness coefficient of the tension section does not change the jumping behavior of the center of mass, it has a significant effect on the internal oscillations of the system. Consequently, utilizing a specific tension stiffness for the mechanism is a choice that depends on the desired internal behavior of the mechanism, and may vary in different applications.

3.5 Conclusion and Discussion

In this study, we investigate the dynamic behaviors of a jumping mechanism consisting two masses connected by a nonlinear spring characterized by a generic piecewise linear function. We derive the non-dimensional equations of motion and solve them numerically to elucidate the effect of two main sections of the nonlinear force-displacement curve, i.e. compression and tension, on the jumping performance of the system. We observe that utilizing nonlinear springs can store more initial strain energy in the system compared to a linear spring, and can lead to higher jumps both in term of the center of gravity and the individual masses. However, the energy efficiency of the jumping would drop slightly. In addition, we saw that the stiffness coefficient of the tension section of the non-linear force-displacement curve does not affect the airborne motion of the center of gravity. Although it has a significant effect on the internal oscillations of the jumping mechanism after it leaves the ground. Researchers have investigated various approaches for creating nonlinear spring characteristics, from combining different linear springs [67] to fluidic [35,63,105] and bi-stable [26] origami. Therefore, results of this study is generic and can be applied to a variety of robotic designs to create more efficient and optimized jumping and hopping performance.

In the next chapter, we use the results and outcome of this study to analyze the effect of using a Tachi-Miura polyhedron (TMP) bellow origami structure to materialize the nonlinear spring with desired strain-softening effects in the jumping mechansim. We show how this origami strcture can enhance the performance of the jumping mechanism.

Chapter 4

Design and Optimization of an Origami-Inspired Jumping Mechanism with Nonlinear Stiffness Properties

4.1 Abstract

This research investigates the feasibility of utilizing origami folding techniques to create an optimized jumping mechanism. As a theoretical example, we study the dynamic characteristics of a jumping mechanism consisting of two masses connected by a Tachi-Miura Polyhedron (TMP) origami structure with nonlinear stiffness characteristics. We show how the desired "strain-softening" effects of the TMP structure can lead to design of jumping mechanisms with optimized performance. The kinematics of TMP origami structure is reviewed and a modified model of its reaction-force displacement curve is presented. We derive the equations of motion of the jump-

ing process and use their numerical solutions extensively for design optimization. Through this process we are able to obtain optimum geometrical configurations for two different objectives: The maximum time spent in the air and the maximum clearance off the ground. Results of this study can lead to emergence of a new generation of more efficient jumping mechanisms with optimized performance in the future.

4.2 Introduction

Among the myriad of great achievements in human history, invention of robots is a major breakthrough. Robots have affected and revolutionized so many aspects of our mundane life. From industrial [106–108] and military [109] applications to education [110, 111] and healthcare [112, 113] services, they have been and will continue improving the quality of our lives. Among the various existing categories of robots, mobile robots are particularly important because they can perform tasks that are inaccessible or unsafe for humans [114], such as volcano exploration, coal extraction, and disaster rescue [115]. Mobile robots can be classified into five different categories according to their ground-contact-based modes of locomotion: wheeled robots, tracked robots, snake robots, legged robots, and wheel-legged robots [115]. Among them, the legged robots are particularly advantageous due to their relative superiority in maneuvering and their capability to access vastly different terrains [116] like mountain lands, sands, and even rugged terrains [115].

However, the dynamics of legged robots, in general, is more complicated compared to the wheeled, tracked, or snake robots especially due to their impacts with the ground [84]. They also require complex nonlinear control strategies. Therefore, researchers have been encouraged to study single-legged robotic systems as well [84, 117]. Despite the relative simplicity of their configuration, single-legged robots are found to be extremely advantageous in different applications [84]. The locomotion in this kind of robotic systems is achieved by jumping [85], which is a relatively simple mode of locomotion that can be beneficial in terrains that are inaccessible to wheeled or tracked systems [84]. Recently, there have been a surge of interest in single-legged robotic systems and several researchers have studied different facets of jumping mechanisms and their locomotion [86, 89, 90, 93].

One of the most important and crucial topics in the field of jumping robots is the energy storage technique. In all of the existent jumping mechanisms, the jumping phase of motion is achieved by an instant release of the stored energy in the system [89]. Therefore, energy storage has an undeniably important role in the performance of the jumping robots [117]. Researchers have proposed various methods for storing energy in robotic systems: From traditional springs [118–120] (compression, extension, or torsional springs), and compressed air [96], to custom-designed elastic elements [98, 99, 102]. The latter approach of energy storage essentially uses the nonlinear spring elements to introduce unique and desirable nonlinear dynamic characteristics to jumping robots.

Nonlinear spring elements have been used in several jumping robots and their effect on the overall dynamic performance has been studied in several researches. For example, in the study by Yamada et al., the snap-through buckling of a closed elastica has been examined as a means of energy storage [101, 102]. In another study, Fiorini and Burdick investigated a jumping mechanism with a nonlinear stiffness achieved by implementing a linear spring in a 6-bar geared mechanism [104]. Furthermore, the authors of this paper have recently rigorously examined the effects of using a generic nonlinear spring in a jumping mechanism [117] both numerically and analytically. We showed that utilizing nonlinear springs with "strain-softening" characteristics, can increase the initial stored energy and consequently create higher jumps in terms of center of gravity and ground clearance, while sacrificing only a negligible amount of efficiency [117]. More importantly, results of this study were generic so that they can be applied to different types of nonlinear spring mechanisms. This leads to the research question of this study: Can we use origami structure to materialize the desired nonlinear stiffness characteristics in a jumping mechanism?

Origami – the ancient Japanese art of paper folding – has recently expanded the design and fabrication repertoire of engineers [27]. It has found lots of applications from kinetic architectures [72] and self-folding robots [17] to surgery devices [121] and DNA machines [122]. In addition, researchers have been studying origami folding techniques as a method for achieving tunable nonlinear stiffness recently such as negative and quasi-zero stiffness [59, 123] and multi-stability [26, 124].

Therefore, in this paper, we investigate the feasibility of using origami as the energy storage element in the jumping mechanism and achieve the desired "strain-softening" nonlinear stiffness. To this end, we first analyze the stiffness properties of a re-entrant origami structure based on Tachi-Miura polyhe-dron (TMP) [33] and investigate the effect of its design parameters on the structure's overall force-displacement relationship. Then, we examine a basic jumping mechanism consisting of two masses connected by the TMP structure —– which acts as a nonlinear spring element in the system —– and analyze its dynamic jumping behavior. Finally, we try to optimize the design of this origami jumper based on two different performance criteria: 1) jumping air-time and 2) clearance of the bottom mass.

The rest of the paper is organized as follows: In Section 4.3, we review the governing kinematic relations of TMP structure and its force-displacement curve under quasi-static loading. Furthermore, we modify the mathematical model of its force-displacement curve based on the nonlinear constitutive model of rotational springs proposed by Liu and Paulino [125]. In Section 4.4, we derive the equations of motion of the jumping mechanism for the pre-jump and post-jump phases of motion. Section 4.5 focuses on design optimization of the origami structure based on the abovementioned performance criteria. To this end, we solve the derived equations of motion numerically and use the results extensively. Section 4.6 concludes the paper with a summary and discussion.

4.3 Tachi-Miura Polyhedron (TMP) Bellow

In this study, we use a variation of the Tachi-Miura polyhedron (TMP) origami bellow studied by Yasuada and Yang [33] as the basis for our jumping mechanism. The TMP bellow is essentially a linear assembly of identical unit cells and each cell consists of two connected origami sheets (aka. the front sheet and back sheet shown in Figure 4.1(a,b)). The geometric design of two origami sheets can be uniquely defined based on two fold lines (l, m), the side length (d) and a sector angle (α) For clarity, we refer the fold lines that remain parallel to the horizontal $x - z$ reference plane as the "main-folds" and all other fold lines are the "sub-folds" (Figure 4.1(b)).

Despite the relatively complex geometry, TMP bellow is rigid-foldable in that its folding motion does not induce any deformations in the facets. Therefore, we can assume the facets are rigid, and the fold lines behave like perfect hinges with assigned torsional stiffness. In this way, we can use the virtual work principle and estimate the reaction force F of the TMP bellow along its length direction (y-axis in Figure 4.1(a)) as follows [33]:

$$F = \frac{-32}{Nd\cos\theta_M}\left[k_M(N-1)\left(\theta_M - \theta_{M_0}\right) + Nk_S\left(\theta_S - \theta_{S_0}\right)\frac{\cos^3\theta_G/2\sin\theta_M}{\cos\alpha\sin\theta_S}\right]. \tag{4.1}$$

In this equation, is the number of unit cells in the TMP bellow; and are the equivalent torsional stiffness of the main-folds and sub-folds, respectively; is the dihedral an-gle associated with the main-folds, defined between the facets and x-z reference plane as shown in Figure 1(c); is the dihe-dral angle between the facets along the sub-folds; and is the angle between x-axis and a main-fold. Denote as the change in unit cell height through folding and as the main fold angle corresponding to the initial, resting configuration, the magnitude of these angles can be calculated as:

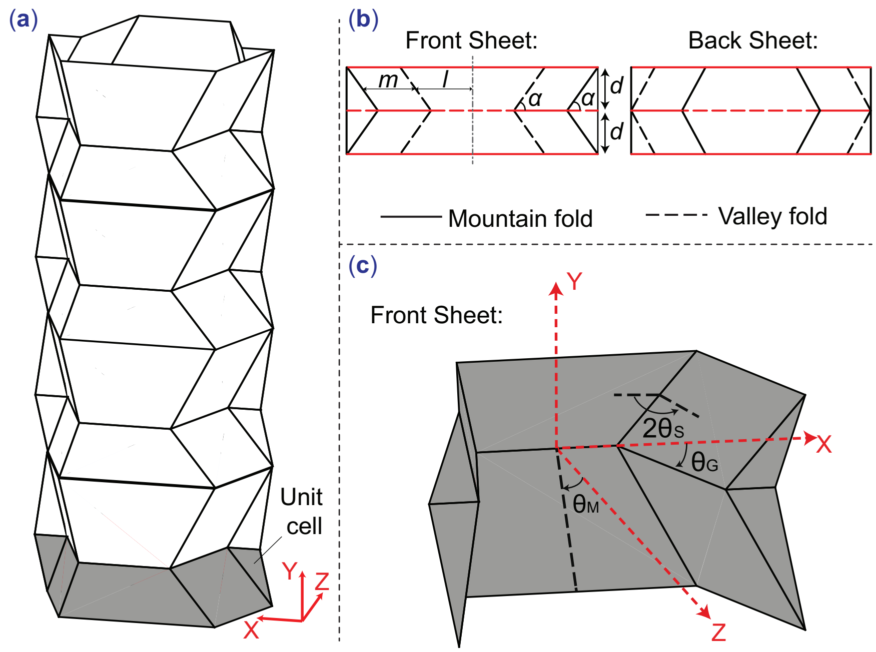

Figure 4.1: Design of the Tachi-Miura Polyhedron (TMP) bellow. (a) The overall external geometry of a TMP bellow; this one consists of eight unit cells, and one of them is highlighted in gray. (b) The crease design of the front sheet and back sheet that makes up two unit cells. The main-folds are highlighted by red color. (c) The external geometry of a folded front sheet, showing the different angles used in the kinematics and mechanics analysis.

In this equation, N is the number of unit cells in the TMP bellow;k_M and k_S are the equivalent torsional stiffness of the main-folds and sub-folds, respectively; θ_M is the dihedral angle associated with the main-folds, defined between the facets and $x - z$ reference plane as shown in Figure 4.1(c); θ_S is the dihedral angle between the facets along the sub-folds. Denote u as the change in unit cell height through folding and θ_{M0} as the main fold angle corresponding to the initial, resting configuration, the magnitude of these angles can be calculated as:

$$\theta_M = \sin^{-1}\left(\sin\theta_{M0} - \frac{u}{Nd}\right), \tag{4.2}$$

$$\theta_G = 2\tan^{-1}\left(\tan\alpha\cos\theta_M\right), \tag{4.3}$$

$$\theta_S = \cos^{-1}\left(\frac{\sin\frac{\theta_G}{2}}{\sin\alpha}\right). \tag{4.4}$$

Figure 4.2(a) illustrates the force displacement curve of a TMP bellow design based on $l = m = d = 30mm$, $\alpha = 40°$, $\theta_M0 = 65°$ and $k_M = k_S = 0.03N.m/rad$. Due to the nonlinear geometric relationships induced by origami folding, the TMP bellow shows a strong nonlinearity. In Particular, it shows a "strain softening" behavior in compression. That is, the TMP exhibits a high stiffness under small compressive deformation, but its stiffness decreases as the deformation increases. Previous study by the authors has shown that such nonlinearity is desired because it can store more energy upon compression compared to the traditional linear spring, leading to a higher jump [117]. Moreover, after careful examinations, we discover that the reaction force generated by the sub-folds shows a stronger nonlinearity than the main-folds. Therefore, we will intentionally weaken main-folds and stiffen up the sub-folds to strengthen the desired non-linearity. This allows us to neglect the contribution of the main-folds to the overall reaction force, and simplify equation 4.1 into the following:

$$F = \frac{-32k_S}{Nd\cos\theta_M}\left[N\left(\theta_S - \theta_{S0}\right)\frac{\cos^3\frac{\theta_G}{2}\sin\theta_M}{\cos\alpha\sin\theta_S}\right]. \tag{4.5}$$

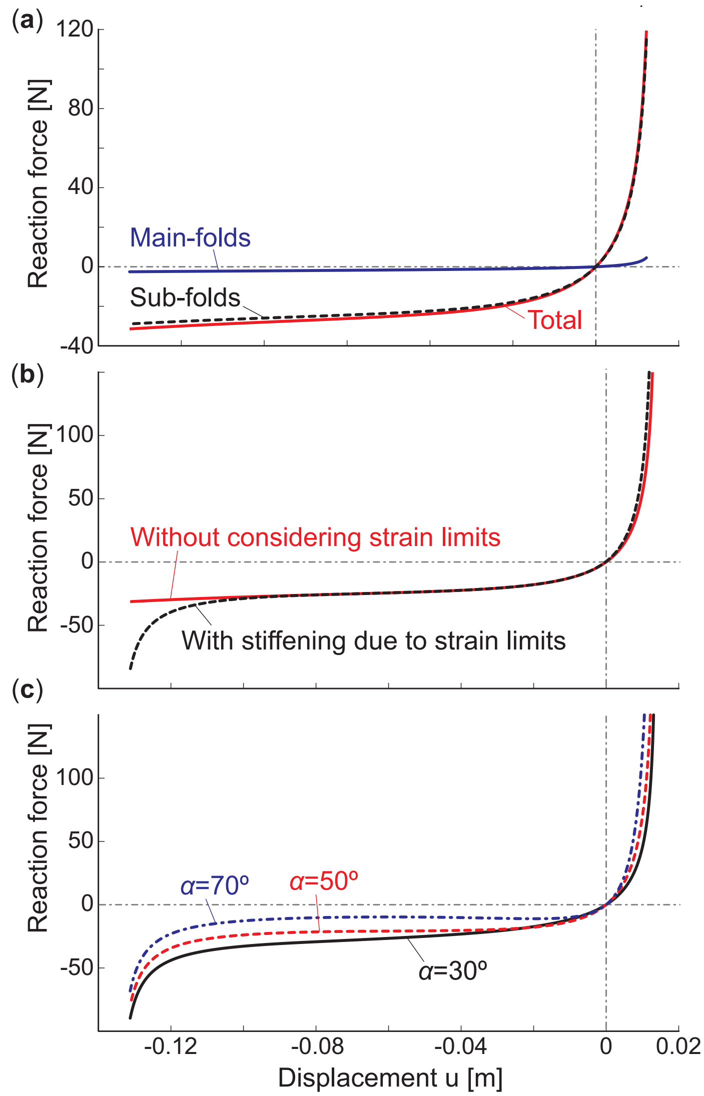

Figure 4.2: The force-displacement curve of a TMP bellow. (a) The contribution of main-folds and sub-folds to the overall reaction force, and the sub-folds show the desired "strain softening" behavior in compression. (b) The modified reaction force curve considering the deformation limit due to folding. (c) The reaction force curve corresponding to different α, while all other design variables remain the same as those used in (a).

However, this reaction force equation does not consider the deformation limits due to rigid folding. That is, TMP bellow can only be folded in-between its compression limit at $\theta_S = 0°$ (fully compressed) and extension limit at $\theta_S = 90°$ (fully stretched). However, in reality when the TMP is compressed near $\theta_S = 0°$, its facets would come into contact with each other and resist further compression. On the other hand, when the TMP is extended near $\theta_S = 90°$, both the front and back sheets are stretched flat so that the overall tension stiffness would increase significantly. To incorporate these deformation limits by folding, we adopt the method developed by Liu and Paulino [125] and set two folding angle limits: $\theta_1 = 20°$ for compression and $\theta_2 = 70°$ for tension. When $\theta_S < \theta_1$, the reaction force equation (equation 4.5) is modified into the following:

$$F = \frac{-32k_S}{Nd\cos\theta_M}[N(\theta_1 - \theta_{S0}) + \frac{2\theta_1}{\pi}\tan\left(\frac{\pi(\theta_S - \theta_1)}{2\theta_1}\right)\frac{\cos^3\frac{\theta_G}{2}\sin\theta_M}{\cos\alpha\sin\theta_S}]. \tag{4.6}$$

Similarly, when $\theta_S > \theta_2$, the reaction force becomes:

$$F = \frac{-32k_S}{Nd\cos\theta_M}[N(\theta_2 - \theta_{S_0}) + \frac{2\theta_2}{\pi}\tan(\frac{\pi(\theta_S - \theta_2)}{2\theta_2})\frac{\cos^3\frac{\theta_G}{2}\cos\theta_M}{\cos\alpha\cos\theta_S}] \; . \tag{4.7}$$

Figure 4.2(b) illustrates the modified reaction force, which is used for the subsequent dynamic analysis and optimization. Figure 4.2(c) illustrates the effect of the sector angle α on the force-displacement curve. When other design variables are fixed, increasing the α angle would decrease the reaction force in the structure when compressed. This leads to less stored strain energy. For this reason we would expect smaller α angles to lead to better jumping performance.

4.4 The Dynamics of TMP Jumper

The TMP jumping mechanism (shown in Figure 4.3) consists of two identical masses connected by a TMP bellow, which serves as the energy storage element in the mechanism. It is worth noting again that the TMP exhibits nonlinear stiffness properties. In order to only focus on the effects of nonlinear stiffness on the jumping

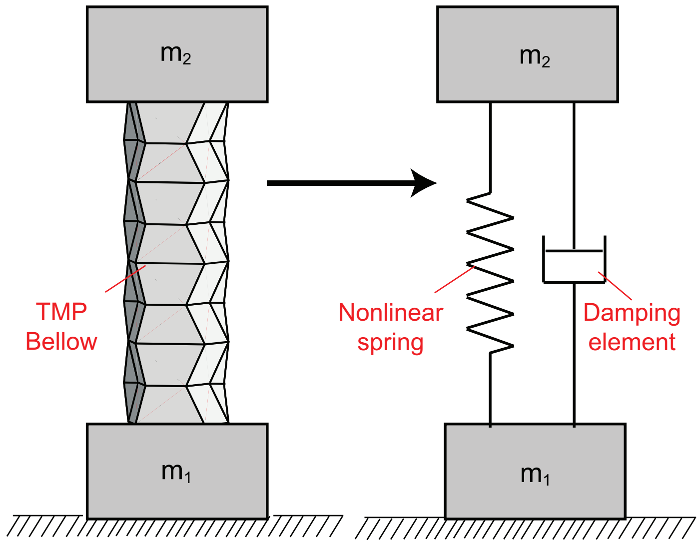

Figure 4.3: The jumping mechanism based on TMP bellow and its equivalent system. Here the nonlinear spring shows the force-displacement curves defined in equations (4.5-4.7).

performance of the origami structure, in this study, we assume that damping is zero. One should notice that although damping can affect the dynamics quantitatively, it does not fundamentally alter the behavior of the structure as long as it does not eliminate the desired mono-stable strain softening stiffness. To initiate jumping, this mechanism is actuated via an external force acting on the upper mass, which deforms the TMP bellow and thus stores energy in the system.

The dynamics of jumping can be divided into two distinct phases: 1) pre-jump phase and 2) post-jump phase. To focus on the effects of the TMP bellow on the dynamic performance of the jumping mechanism, we assumed that the masses are equal: $m_1 = m_2 = M$. In the following two subsections we investigate the motion in these two phases and derive the equations of motion for pre-jump and post-jump phases, respectively.

4.4.1 Pre-jump Phase of Motion

In this phase, the jumping mechanism is actuated by an external force on the upper mass, which moves it to a certain initial displacement (d). Then the external force is removed and the reaction force from TMP bellow accelerates the upper mass upward. This pre-jump phase of motion continues until the bottom mass leaving the ground. One can derive the governing equation of motion for this phase as:

$$M\ddot{Y}_2 = -F(Y_2 - l_0) - Mg, \tag{4.8}$$

where M is the mass of the upper body; $F(Y_2 - l_0)$ is the reaction force of the TMP bellow defined in equation 4.5; l_0 is the initial, resting length of the TMP; $\ddot{Y}_2$ and Y_2 are the acceleration and position of the upper mass (relative to the ground), respectively.

4.4.2 Post-jump Phase of Motion

If the jumping mechanism can overcome the gravitational force after the deformation of the TMP bellow becomes positive, the jump can occur. In other words, once the restoring force of the TMP bellow on the lower mass exceeds its weight (aka. $F(Y_{2,jump} - l_0) \geq Mg$, the jumping mechanism enters the second phase of motion. Here $Y_{2,jump}$ stands for the critical upper mass displacement when the jump occurs.

Once the bottom mass has left the ground, the governing system of coupled equations of motion can be described as:

$$\begin{aligned} M\ddot{Y}_1 &= F(Y_2 - Y_1 - l_0) - Mg, \\ M\ddot{Y}_2 &= -F(Y_2 - Y_1 - l_0) - Mg. \end{aligned} \tag{4.9}$$

The initial conditions of equation 4.9 can be extracted from the solution of the pre-jump phase equation 4.8. Figure 5 shows a typical time response of an origami jumper, in which one can clearly identify the two different phases of jumping. Moreover, once the origami jumper is airborne, it also exhibits an internal oscillation with respect to its center of mass. In the next section, we use the numerical solution of equation (8) and (9) to optimize the performance of the jumping mechanism.

4.5 TMP DESIGN OPTIMIZATION

The goal of this optimization is to identify the TMP bel-low design that can lead to the best jumping performance. To this end, we describe the jumping performance based on two different objectives: Airtime and Clearance (illustrated in Figure 4.4). Airtime is the total time that the jumping mechanism spends in the air; and Clearance is the peak height achieved by the lower mass. We normalize the Clearance by the rest height of TMP bellow and use the normalized values as the optimization objective function.

There are five design variables that that can be tailored to optimize the jumping performance. The definition and range of these variables are listed in Table 4.1, and Figure 4.1 illustrates how they relate to the overall geometry of TMP bellow. Moreover, three geometric constraints are imposed. The first constraint ensures that the design of TMP bellow is properly defined and there are no conflicting crease lines. The second constraint defines a minimum main-fold length for the ease of manufacturing and assembly. The third constraint sets an upper limit on the unit cell length. The additional $15mm$ in the third constraint is for an extended tab to facilitate the assembly of two sheets.

In this study, the three constraints on design variables are defined based on the

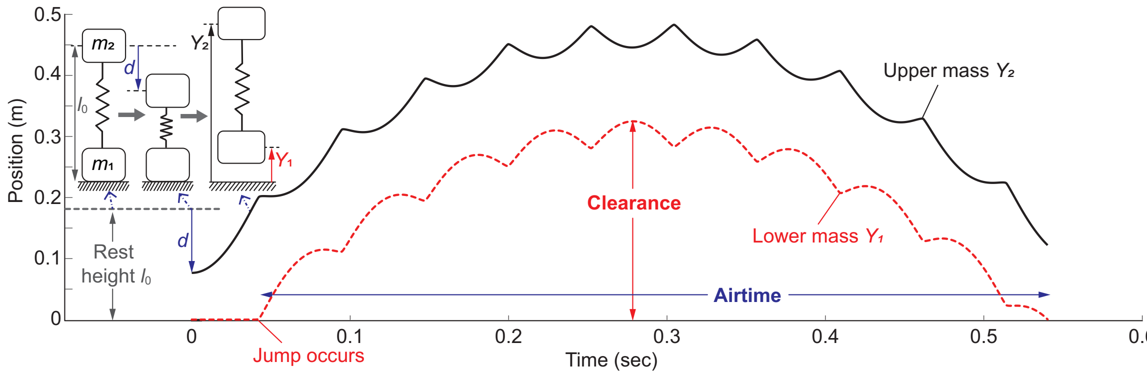

Figure 4.4: A typical time response of the TMP origami jumper. The schematic plots at the upper left corner illustrates the origami jumper at resting configuration, initial configuration when the upper mass is compressed, and post jump phase, respectively. The two objective functions of the design optimization: Airtime and Clearance are highlighted. Notice the internal oscillation during the post-jump phase influences the Clearance performance.

fabrication capabilities available to the authors. Increasing the variables beyond the upper limits would require additional fabrication equipment; while reducing them below the lower limit would makes assembly too difficult. Regardless, we can still obtain valuable insights on the correlations between the design variables and jumping performance within these constraints.

Besides the geometric design variables of TMP bellow, the magnitudes of some other variables are defined for the optimization (Table 4.2). One of them is the stress-free, resting folding angle of the main-folds θ_{M_0}. However, a very large resting folding angle is difficult to achieve in experiments. Based on repeated trial-and-errors using TMP prototypes of different geometric designs, $\theta_{M_0} = 65°$ is found to be a realistic value. Another important variable is the initial folding ratio, which is essentially the initial condition of the dynamic simulation discussed below. Again, after repeated trial-and-error, it is found that an initial folding ratio of 75 % is preferred because it can achieve the maximum stored energy for jumping without inducing any significant plastic deformation. The crease torsional stiffness coefficient k is estimated based

Table 4.1: The design variables and geometric constraints used in the design optimization.

N: Unit cell	$4 \leq N \leq 10$
d: Side length	$20mm \leq d \leq 40mm$
α: Sector angle	$30^\circ \leq \alpha \leq 70^\circ$
l: Fold Length	$20mm \leq l \leq 40mm$
m: Fold Length	$20mm \leq l \leq 40mm$
Constraint 1:	$2l - d \cot \alpha + 2m \cos \alpha \geq 0$
Constraint 2:	$\frac{d}{2 \tan \alpha} - l \leq -10\text{mm}$
Constraint 3:	$2 \left(l + m + \frac{d}{2} \tan \left(\frac{\pi}{2} - \alpha \right) + 15 \right) \leq 300\text{mm}$

on the experimental data gathered from different shim stock, which will be used to stiffen the sub-folds.

We numerically simulate the jumping behavior of the TMP mechanism in MATLAB using ode45 solver for the different jumping phases outlined in Section 4.4. In these simulations, we assume the upper mass is lowered so that the TMP bellow is compressed to the initial folding ratio of 75%, and then the upper mass is released for jumping. We then use the ode45 solver to obtain the pre-jump time response according to equation 4.8. Based on this response, we can identify the moment when the TMP bellow is stretched to the point that its resulting tension force surpass the weight of lower mass. At this moment, the lower mass leaves the ground so that we can use this as the initial conditions for the post-jump phase. Ode45 solver is

Table 4.2: The design variables and geometric constraints used in the design optimization.

M: End masses	$m_1 = m_2 = M = 0.25kg$
θ_{M_0}: Resting main angle	$\theta_{M_0} = 65°$
FR: Initial folding ratio	$FR = \frac{90° - \theta_M}{90°} \times 100\% = 75\%$
k_S: Sub-fold stiffness	$k_S = 0.0383 Nm/rad$

used again to obtain the time response of the jumping phase so that the Airtime and Clearance can be recorded.

To optimize the TMP bellow design, we integrate the jumping simulations and ModeFrontier using the NSGA-II optimization algorithm. NSGA-II is a common genetic algorithm for multi-objective optimization problems. We use a total population size of 2500 individuals across 5 generations. The optimization results according to each objective function are represented in Table 4.3.

From the results in Table 4.3, one can observe that the optimized sector angle α is always at its lower limit. As we explained in Section 4.3, a lower α angle corresponds to a stronger nonlinearity in the force-displacement relationship of the TMP bellow (Figure 4.2(c)), which is desired for better jumping performance. The optimized unit cell side length d and the crease length l, m are the same. Moreover, d and m are also at their lower limit. The unit-cell side length d appears in the denominator of the reaction force equation (equation 4.9), so a small side length corresponds to a bigger reaction force and therefore more stored strain energy for jumping. The crease length m does not appear in the reaction force equation explicitly, but its value is kept low to avoid violating the third geometric constraint. Similarly, the value of crease length

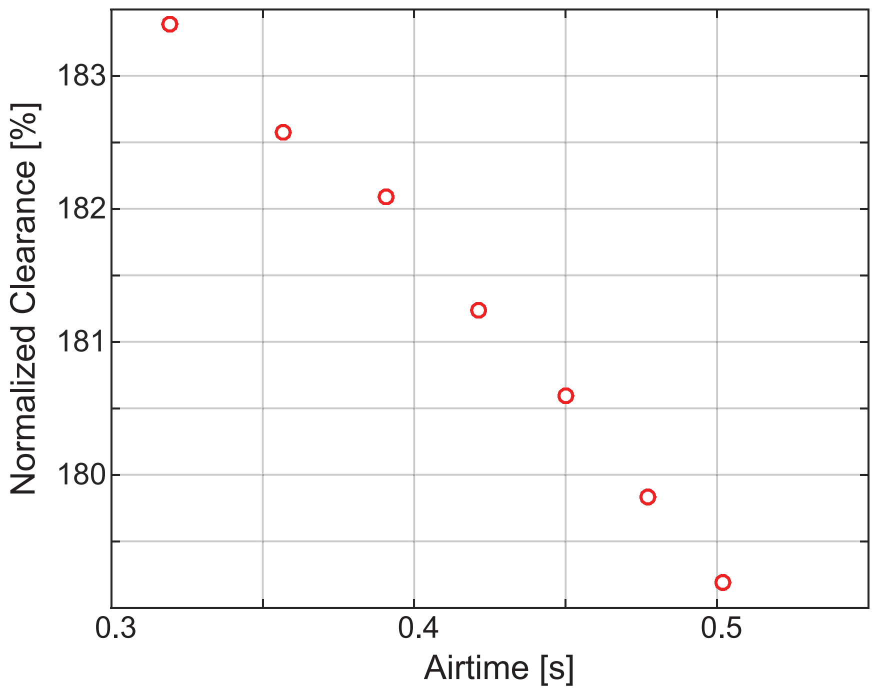

Figure 4.5: Pareto front obtained in the optimization results.

l is also kept low to avoid violating the second geometric constraint.

The difference between the two optimized designs are the number of unit cells N. More unit cells in a TMP bellow means a larger initial displacement of the upper mass, therefore more strain energy is stored for jumping and a longer airtime. However, increasing the N values also increases overall structure height, which can negate the performance of normalized Clearance. Such a trade-off between Airtime and Clearance can be illustrated in the pareto front shown in Figure 4.5.

Table 4.3: Linear TMP parameter sets resulting from single objective optimization

	Design Variables					
	N [-]	α [°]	d [mm]	l [mm]	m [mm]	Airtime [sec]
Optimum Airtime	10	30	20	28.5	20	0.502
Optimum Clearance	4	30	20	28.5	20	0.320

4.6 Discussion and Conclusion

In this study we investigate the idea of utilizing origami folding techniques to enhance the performance of a jumping mechanism. We study the feasibility of using Tachi-Miura Polyhedron (TMP) origmai struture as the energy storing unit in a mechanism consisting of two masses, through analyzing the dynamic characteristics of the system. The TMP origami structure exhibits nonlinear stiffness characteristics. We show how the desired "strain-softening" effects of the TMP structure can lead to design of jumping mechanisms with optimized performance. We present a review of the kinematics of TMP origami structure and derive a modified model of its reaction force-displacement curve. We derive the equations of motion of the jumping process and use their numerical solutions extensively for design optimization. The optimum geometric configurations for two different objectives are derived: The maximum time spent in the air (a.k.a airtime) and the maximum clearance off the ground. Although this study has been conducted on a specific origami pattern (TMP bellow), the results show that origami folding techniques can add more tools to the repertoire of robotic researchers to create jumping mechanisms with higher performance. Therefore, the outcome of this research can lead to emergence of a new generation of more efficient jumping mechanisms with optimized performance in the future.

So far, we investigate two possible dynamic applications of origami folding. The next chapter on the hand, focuses on the second perspective of analyzing dynamics of origami folding. In chapter 5, we demonstrate how can we use dynamic excitation to achieve reversible and rapid folding in a bi-stable origami structure.

Chapter 5

Dynamic Folding of Origami By Exploiting Asymmetric Bi-Stability

5.1 Abstract

In this study, we examine a rapid and reversible origami folding method by exploiting a combination of resonance excitation, asymmetric bi-stability, and active control. The underlying idea is that, by harmonically exciting a bi-stable origami at its resonance frequencies, one can induce rapid folding between its different stable equilibria with a much smaller actuation magnitude than static folding. To this end, we use a bi-stable water-bomb base as an archetypal example to uncover the underlying principles of dynamic folding based on numerical simulation and experimental testing. If the water- bomb initially settles at its "weak" stable state, one can use a base excitation to induce the intra-well resonance. As a result, the origami would fold and remain at the other "strong" stable state even if the excitation does not stop. The origami dynamics starting from the strong state, on the other hand, is more complicated. The water-bomb origami is prone to show inter-well oscillation rather than

a uni- directional switch due to a nonlinear relationship between the dynamic folding behavior, asymmetric potential energy barrier, the difference in resonance frequencies, and excitation amplitude. Therefore, we develop an active feedback control strategy, which cuts off the base excitation input at the critical moment to achieve robust and uni-directional folding from the strong stable state to the weak one. The results of this study can apply to many different kinds of origami and create a new approach for rapid and reversible (self-)folding, thus advancing the application of origami in shape morphing systems, adaptive structures, and reconfigurable robotics.

5.2 Introduction

Origami—the ancient art of paper folding—has received a surge of interests over the past decade from many research communities, such as mathematicians, material scientists, biotics researchers, and engineers [126]. A key driving factor underneath such interests is the seemingly infinite possibilities of developing three-dimensional shapes from folding a simple flat sheet. The *kinematics* (or shape transformation) of origami is rich and offers many desirable characteristics for constructing deployable aerospace structures [127], kinetic architectures [72, 128], self-folding robots [17], and compact surgery devices [21, 129]. The *mechanics* of origami offers a framework for architecting material systems [126] with unique properties, like auxetics [130], tunable nonlinear stiffness [117, 131], and desirable dynamic responses [26, 63, 105]. Moreover, the origami principle is geometric and scale-independent, so it applies to engineering systems of vastly different sizes, ranging from nanometer-scale graphene sheets [132] all the way to meter-scale civil infrastructures [25].

For most of these growing lists of origami applications, large amplitude and autonomous folding (or self-folding) are crucial for their functionality. However, achieving a (self-)folding efficiently and rapidly remains a significant challenge [133]. To this end, we have seen extensive studies of using responsive materials to achieve folding via different external stimuli, such as heat [134], magnetic field [135], ambient humidity change [136], and even light exposure [137, 138]. In a few of these studies, bi-stability was also introduced as a mechanism to facilitate folding and maintain the folded shape without requiring a continuous supply of stimulation [139, 140]. While promising, the use of responsive materials could incur complicated fabrication requirements, and their folding can be slow or non-reversible.

In this study, we examine a rapid and reversible origami folding method by exploiting the combination of harmonic excitation and embedded asymmetric bi-stability. Bi-stable structures possess two distant stable equilibria (or "stable states"), and this strong non-linearity can induce complex dynamic responses from external excitation, such as super-harmonics, intra/inter-well oscillations, and chaotic behaviors [141]. These nonlinear dynamics have found applications in wave propagation control [142], energy harvesting [143], sensing [144], and shape morphing [145, 146]. Here, shape morphing is particularly relevant to folding, so we used a proof-of-concept numerical simulation to demonstrate the feasibility of using harmonic excitation to induce folding in a bistable water-bomb base origami [147, 148] (Figure 5.1(a)). The bi-stability of the water-bomb base is asymmetric [139, 140], i.e. the two stable states of the structure are asymmetric with respect to the unstable state and the energy gaps of the two stable states are different, so the resonance frequencies of its two stable configurations differ significantly. Due to this asymmetry, it is possible that when the water-bomb origami is harmonically excited at the resonance frequency of its current stable state, it can rapidly fold to and remain at the other stable state. Moreover, the required excitation magnitude by this dynamic folding method is smaller than static folding.

Building upon this proof-of-concept study, this study aims to obtain a comprehensive understanding of the harmonically-excited rapid folding via a combination of dynamic modeling, experimental validation, and controller design. First, we formulate a new and nonlinear dynamic model of a generic water-bomb origami and conduct an in-depth examination into the relationships among the dynamic folding behaviors, potential energy landscape, resonance frequencies, and excitation amplitudes. It is worth noting that this model is a significant advancement to our previous study in that it releases unnecessary boundary conditions and includes the facet rigid body motion (both translational and rotational). Since the bistability of water-bomb origami is asymmetric, we can designate its two stable states as "strong" or "weak" based on the magnitude of potential energy barriers between them. Our simulation and experiment results show dynamic folding from the weak stable state to the strong one is relatively easy, but folding in the other direction is quite challenging to achieve. That is, starting from the strong stable state, the water-bomb origami tends to exhibit inter-well oscillations under most excitation conditions, which is undesirable for rapid folding purposes. This challenge is further complicated by the fact that the nonlinear dynamics of origami are highly sensitive to design variations, fabrication errors, and excessive damping. Therefore, we then devise and experimentally validate a control strategy that ensures the robustness of dynamic folding by cutting off the excitation input at a critical configuration. This control strategy is essential for practical implementations of this dynamic folding method in the future.

It is worth highlighting that although this study uses the water-bomb origami as an example, the insights into the harmonically excited folding and the control strategy can apply to many other origami designs that exhibit asymmetric multi-stability, such as stacked Miura-ori [149], Kresling [150], and leaf-out pattern [151]. Moreover, harmonic excitation at the resonance frequency has a high actuation authority, so it can be an efficient method compared to other dynamic inputs, such as impulse [41]. Therefore, the results of this study can create a new approach for rapid and reversible (self-)folding, thus advancing the application of origami in shape morphing systems, adaptive structures, and reconfigurable robotics.

In what follows, Section 5.3 of this paper details the dynamic modeling of the water-bomb base origami, section 5.4 discusses its dynamic folding behavior under harmonic excitation, section 5.5 explains the active control strategy, and section 5.6 concludes this paper with a summary and discussion.

5.3 Dynamic Model of the Water-bomb Origami

In this section, we derive the governing equation of motion of a generic water-bomb base origami. Assuming the water-bomb is symmetric in its design and rigid-foldable (i.e., rigid facets and hinge-like creases), we can describe the kinematics of a water-bomb with N triangular facets as a two degrees-of-freedom (DOF) mechanism. These two degrees can be defined by the angle between the vertical Z-axis of the origami and its valley creases (θ_v in Figure 5.1(b)), and the vertical position of the central vertex h_p, respectively. We assume that this central vertex is rigidly connected to an external excitation, which is a vertical shaker table in this case (APS Dynamics 113, Figure 5.2). In this way, h_p becomes the dynamic input variable, and θ_v is the only degree-of-freedom left.

Using spherical trigonometry, we can derive the angle between the vertical Z-axis and the mountain creases of the structure as a function of θ_v in that:

$$\theta_m = \cos^{-1}\left(\frac{\cos\alpha}{\cos(d/2)}\right) + \cos^{-1}\left(\frac{\cos\theta_v}{\cos(d/2)}\right), \tag{5.1}$$

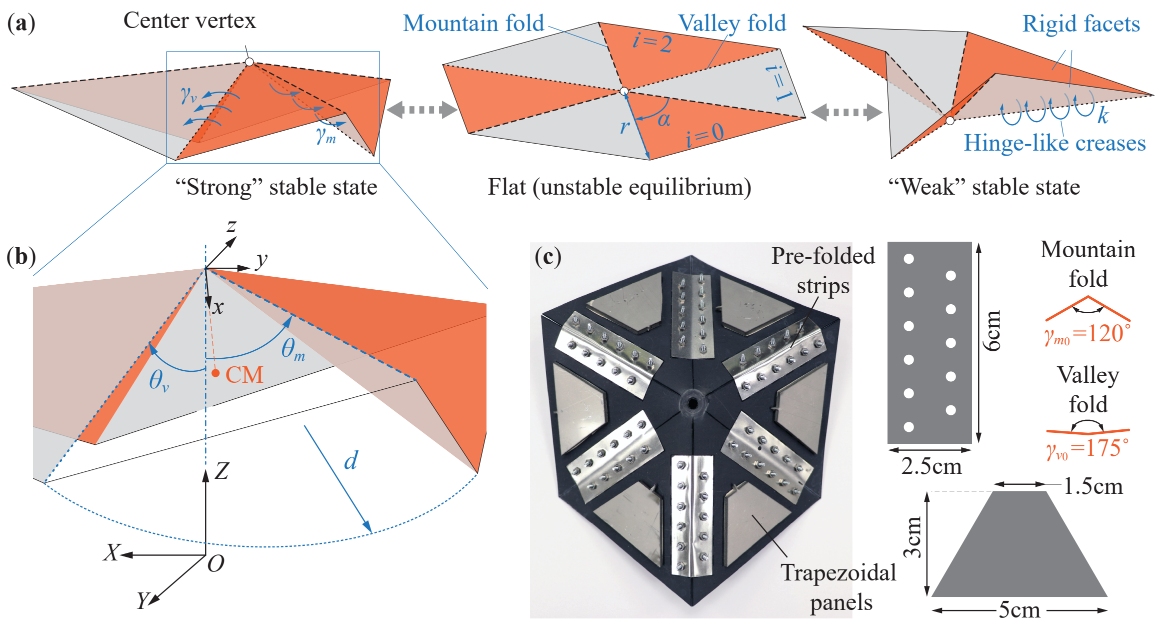

Figure 5.1: The design, folding kinematics, and prototyping of the water-bomb base origami. (a) The external shape of the water bomb origami at its unfolded flat configuration and two stable states ($N = 6$). We assume the triangular facet is rigid, and the fold lines behave like hinges with embedded torsional springs. (b) Variables that define the folding kinematics. The inertial frame of reference (XYZ) is attached to the ground, and the body frame of reference (xyz) is attached to the facets. (c) Proof-of-concept prototype made out of a polypropylene sheet with perforations along the creases. The geometry of the pre-folded shim stocks used to create stiffness along the creases is shown along with its folding angles for mountain and valley crease. The geometry of the water-jet cut trapezoidal panels is also shown.

where $\alpha = 2\pi/N$, and d is the radius of a circular arc defined by the central vertex and two adjacent vertices on the valley creases (Figure 5.1(b)):

$$d = \cos^{-1}\left(\cos^2\theta_v + \sin^2\theta_v \cos\beta\right), \tag{5.2}$$

where $\beta = 2\alpha$. Again, using spherical trigonometry, one can show that:

$$\gamma_m = \pi - \cos^{-1}\left(1 + \frac{\cos^2\theta_v + \sin^2\theta_v \cos\beta - 1}{\sin^2\alpha}\right), \tag{5.3}$$

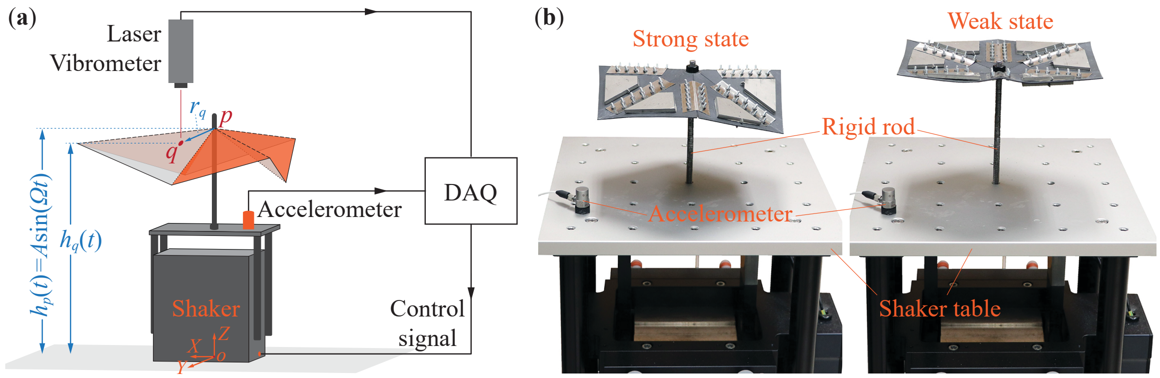

Figure 5.2: Dynamic folding test of the waterbomb origami. (a) A schematic drawing showing the overall experiment setup. A rigid rod connects the central vertex to the shaker table. The facets are free to rotate. The vertical oscillations of one of the facets are measured using a laser vibrometer ($r_q \approx 3$cm), which is then converted to folding angles in the DAQ system. The vibrations of the shaker are measured using a piezoelectric accelerometer. (b) The water-bomb origami prototype in its strong stable state (left) and weak stable state (right).

$$\gamma_v = \begin{cases} -\pi + 2\cos^{-1}\left(\cot\alpha\tan\dfrac{d}{2}\right) + 2\cos^{-1}\left(\cot\theta_v\tan\dfrac{d}{2}\right) & \text{if } \theta_v \leq \dfrac{\pi}{2} \\ \pi - 2\cos^{-1}\left(\dfrac{(\cos d - 1)\cot\theta_v}{\sin d}\right) + 2\cos^{-1}\left(\cot\alpha\tan\dfrac{d}{2}\right) & \text{if } \theta_v > \dfrac{\pi}{2} \end{cases} \quad (5.4)$$

where γ_m and γ_v are the angles between the facets connected by the mountain and valley creases, respectively (Figure 5.1).

The position and orientation of each triangular facet can be described by the position of the central vertex h_p in the XYZ (inertial) frame of reference attached to the ground and the orientation of the xyz (body) frame of reference. The latter can be described by three independent Euler angles, which represent the consecutive rotations of the XYZ (inertial) frame of reference needed to align it with the xyz (body) frame of reference. The order of rotations is arbitrary. Here, we choose the zyx order (aka, the aircraft rotations) that consists of three steps: The first step is a rotation about the Z-axis by ψ_i, where $\psi_i = \frac{2\pi}{N}$. The second step is a rotation about the y'-axis (aka., y-axis of the rotated frame after the first step) by θ_i, where $\theta_i = \frac{1}{2}(\pi - \theta_v - \theta_m)$. The third step is a rotation about the x''-axis (aka. x-axis of the rotated frame after the second step) by ϕ_i, where

$$\phi_i = \begin{cases} \dfrac{\gamma_m}{2} & \text{if } i \text{ is even,} \\ 2\pi - \dfrac{\gamma_m}{2} & \text{if } i \text{ is odd.} \end{cases} \tag{5.5}$$

Here, the sub-index "i" ($i = 0 \ldots N-1$) labels the different triangular facets as defined in Figure 5.1(a). Therefore, the total rotation matrix is a combination of these three steps in that $C_i = \Phi_i \Theta_i \Psi_i$, where:

$$\Phi_i = \begin{bmatrix} 1 & 0 & 0 \\ 0 & \cos\phi_i & \sin\phi_i \\ 0 & -\sin\phi_i & \cos\phi_i \end{bmatrix}, \tag{5.6}$$

$$\Theta_i = \begin{bmatrix} \cos\theta_i & 0 & -\sin\theta_i \\ 0 & 1 & 0 \\ \sin\theta_i & 0 & \cos\theta_i \end{bmatrix}, \tag{5.7}$$

$$\Psi_i = \begin{bmatrix} \cos\psi_i & \sin\psi_i & 0 \\ -\sin\psi_i & \cos\psi_i & 0 \\ 0 & 0 & 1 \end{bmatrix}. \tag{5.8}$$

In addition, the angular velocity of the xyz (body) frame of reference can be derived using:

$$\omega_i = \omega_{xi}\hat{\imath} + \omega_{yi}\hat{\jmath} + \omega_{zi}\hat{k}, \tag{5.9}$$

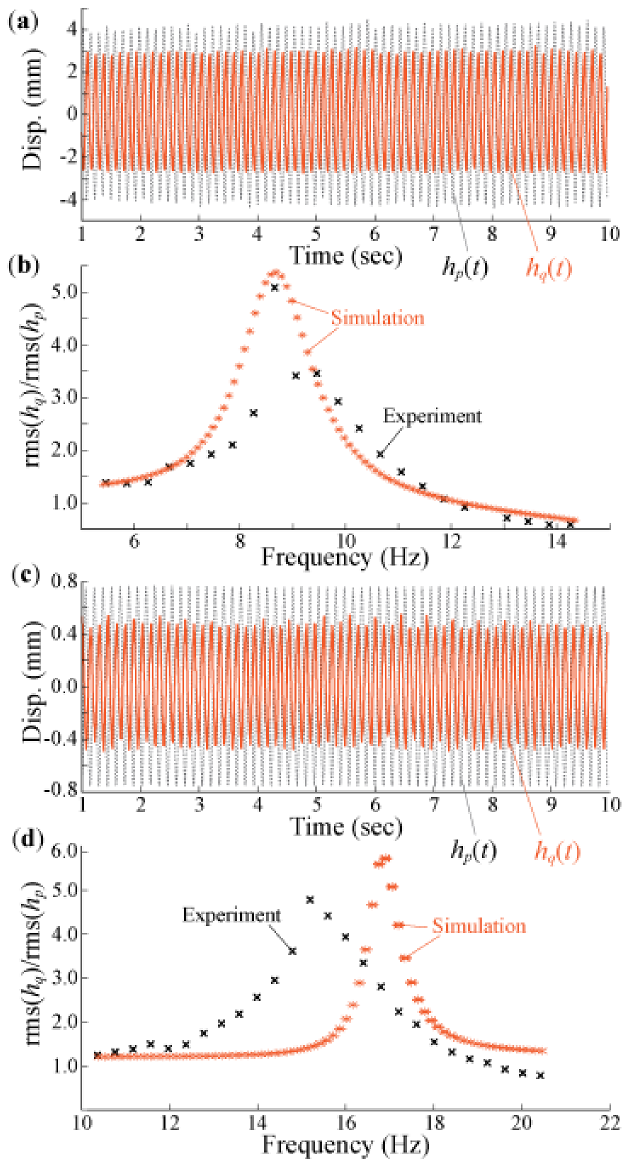

Figure 5.3: Frequency response near the two stable states of water-bomb origami. (a) A typical time response from small amplitude intra-well oscillations around the stress-free stable state. Here the vertical displacements of point q are represented in orange and the corresponding shaker excitations represented in gray. (b) Stroboscopic sampling results for intra-well oscillations around the stress-free strong stable state. (c) Typical time response of similar small-amplitude intra-well oscillations around the other stable state.(d) The corresponding stroboscopic sampling results.

where:

$$\begin{cases} \omega_{xi} = \dot{\phi}_i - \dot{\psi}_i \sin\theta_i, \\ \omega_{yi} = \dot{\psi}_i \cos\theta_i \sin\phi_i + \dot{\theta}_i \cos\phi_i, \\ \omega_{zi} = \dot{\psi}_i \cos\theta_i \cos\phi_i - \dot{\theta}_i \sin\phi_i. \end{cases} \tag{5.10}$$

5.3.1 Kinetic energy of the origami

As the water-bomb base origami folds, its facets exhibit both translational and rotational motions with respect to the central vertex. One can show that the total kinetic energy of the origami structure originates from these two distinct motions based on the following equations:

$$T_{tot} = \frac{1}{2} N m |v_p|^2 + \sum_{i=0}^{N-1} \left(\frac{1}{2} \omega_i^I \omega_i + m v_p \cdot \dot{\rho}_{ci} \right), \tag{5.11}$$

where, m is the mass of a triangular facet, v_p is the velocity of the central vertex. $\dot{\rho}_c = \omega \times \rho_{ci}$, where ρ_{ci} is the vector of center of mass of each facet in xyz (body) frame of reference. Note that v_p and $\dot{\rho}_{ci}$ should be expressed in the same frame of reference which is possible using the total rotation matrix C. Finally, the matrix I contains that moment of inertia of each facet around the central vertex in that

$$I = \begin{bmatrix} I_{xx} & 0 & 0 \\ 0 & I_{yy} & 0 \\ 0 & 0 & I_{zz} \end{bmatrix}, \tag{5.12}$$

where, $I_{xx} = \frac{3}{4} m r^2 \sin^2\alpha$, $I_{yy} = \frac{6}{7} m r^2 \cos^2(\frac{\alpha}{2})$, and $I_{zz} = \frac{1}{2} m r^2 + \frac{1}{12} m r^2 \cos^2(\frac{\alpha}{2})$.

5.3.2 Gravitational potential energy of the origami

In order to derive the gravitational potential energy of the water-bomb origami, we need to calculate the location of the center of mass of each facet. One can show that the distance of each center of mass from the ground can be derived using the following relationship:

$$Z_{cm} = h_p - \left(\frac{2}{3} r \cos \frac{\alpha}{2} \cos \left(\frac{\theta_m + \theta_v}{2} \right) \right). \tag{5.13}$$

The corresponding gravitational potential energy is $V_G = NmZ_{cm}$.

5.3.3 Elastic potential energy of the origami

Assuming that the triangular facets are rigid and the creases behave like hinges with embedded torsional springs, we can derive the elastic potential energy of the origami as

$$V_E = \frac{N}{2} \left[k_{\gamma_m} (\gamma_m - \gamma_{m0})^2 + k_{\gamma_v} (\gamma_v - \gamma_{v0})^2 \right], \tag{5.14}$$

where k_{γ_m} and k_{γ_v} are the torsional stiffness coefficient of the mountain and valley creases, respectively. γ_m and γ_v are the dihedral folding angles of the mountain and valley creases (Eq. 5.3 and 5.4). In addition, γ_{m0} and γ_{v0} are the corresponding stress-free dihedral angles.

5.3.4 Equation of motion

The Lagrangian of the origami structure becomes $\mathcal{L} = T_{tot} - V_G - V_E$, and we can derive the governing nonlinear equations of motion using

$$\frac{\mathrm{d}}{\mathrm{d}t}\left(\frac{\partial \mathcal{L}}{\partial \dot{\theta}_v}\right) - \frac{\partial \mathcal{L}}{\partial \theta_v} + F_d = 0. \tag{5.15}$$

F_d is the damping force generated along the origami creases, and we assume that it has a simple form of $cr\dot{\theta}_v$. Here, c is the equivalent viscous damping coefficient, and r is the length of each crease.

5.4 Dynamic folding of the bistable water-bomb origami

The equation of motion (5.15) can be solved numerically using MATLAB ODE45 solver to obtain the dynamic response to arbitrary base excitation inputs and initial conditions. We assume that the base excitation is harmonic in that $h_p = A\cos\Omega t$. By solving the equation of motion under small-amplitude excitations and performing a stroboscopic sampling over a range of excitation frequencies, we obtain the intra-well frequency response of the water-bomb origami near its two stable equilibria. In this way, we can identify the corresponding intra-well resonance frequencies.

We analyze the accuracy of the origami dynamic model by comparing its predicted frequency response near the two stable states and experimental measurements from a proof-of-concept prototype. This prototype has a hexagonal shape with a crease length of 10cm ($N = 6$ and $r = 10$cm, Figure 5.1(c)). We cut a 0.76mm thick flame-retardant Polypropylene sheet and perforated the crease lines using an FCX2000 series GRAPHTEC flatbead cutting plotter to create the compliant base layer of the origami. A significant amount of the material along the creases is removed to reduce the damping as much a possible. The torsional stiffness along the creases are generated by attaching 0.127mm thick shim stocks, which are folded carefully to give the initial stress-free crease hihedral angles $\gamma_{m_0} = 120°$ and $\gamma_{v_0} = 175°$. Then, we attach twelve water jet-cut stainless steel trapezoids (24g each) to the triangular facets to offer sufficient inertia. Moreover, these trapezoids provide the desired rigidity to the facets according to the rigid-folding assumptions.

5.4.1 Intra-well frequency response analyses and parameter estimation

Although the geometric design and mass of the origami are known, we need to estimate the magnitudes of torsional stiffness (k_{γ_m} and k_{γ_v}) and damping coefficient (c) of the creases. To this end, we perform intra-well frequency sweeps near both of the stable states of the structure with a small excitation amplitude to obtain the frequency response. Then we can estimate k_{γ_m} and k_{γ_v}, which are assumed equal in this case, and c by fitting the model predicted frequency responses to experimental results using the least square method. In what follows, we show that these stiffness coefficients are crucial for determining the intra- well resonance frequency, and the damping coefficient directly affects the excitation amplitude for dynamic folding.

Figure 5.3(a) shows the experimentally measured frequency response of the water-bomb origami near its stress-free stable state and the closest numerical prediction based on least square method. Here, the frequency response is defined as $\frac{\mathrm{rms}(h_q(t))}{\mathrm{rms}(h_p(t))}$ after the transient response has damped out, where h_q is the vertical displacement of a representative point on the median of a facet (Figure 5.2(a)). We use an OFV-5000 Polytec laser vibrometer equipped with an OFV-503 laser head to capture the displacement response of this representative point and a 352C33 PCB accelerometer to measure the acceleration of the shaker, which is then converted to displacement. We find that $k_{\gamma_m} = k_{\gamma_v} = 0.32\ \frac{\mathrm{N.m}}{\mathrm{rad}}$ and $c = 0.05\ \frac{\mathrm{kg}}{\mathrm{rad.s}}$ give the best fitting at this stress-free stable state. Figure 5.3(b) shows the experimentally measured frequency response near the other stable state and the corresponding numerical prediction by using the estimated crease stiffness and damping coefficient from the previous test. The comparison shows an approximately 15% discrepancy between the estimated resonance frequency of this second stable state and the measured resonance frequency ($15.8Hz$ based on the experiments and $17Hz$ based on simulation). This discrepancy probably originates from a combination of fabrication uncertainties and the simplifications made in the analytical model. Moreover, the experimental results show higher damping than the prediction, which is reasonable due to the higher excitation frequencies at this stable state.

Overall, our model successfully captures the difference in the intra-well resonance frequencies near the two stable states of the water-bomb base origami with a relatively small error. This difference in resonance frequencies comes from the inherently asymmetric potential energy landscape of the origami (Figure 5.4(a)), which creates an asymmetric force-displacement curve (Figure 5.4(b)) with different tangent stiffness near its two stable equilibria. For clarity, we refer to the initial, stress-free stable equilibrium with a deeper potential energy well as the "strong" state, and the other stable equilibrium with a shallower energy well as the "weak" state. The differences in the energy barriers for switching between these two stable states are evident. That is, the origami must overcome a large barrier to switch from the strong stable state to the weak one, but only needs to overcome a small barrier for the opposite switch ($\Delta V_{G_1} > \Delta V_{G_2}$ in Figure 5.4). In the following subsections, we show that the differences in resonance frequencies, energy barriers, and the base excitation amplitude all play crucial roles in the harmonically excited folding of water-bomb origami.

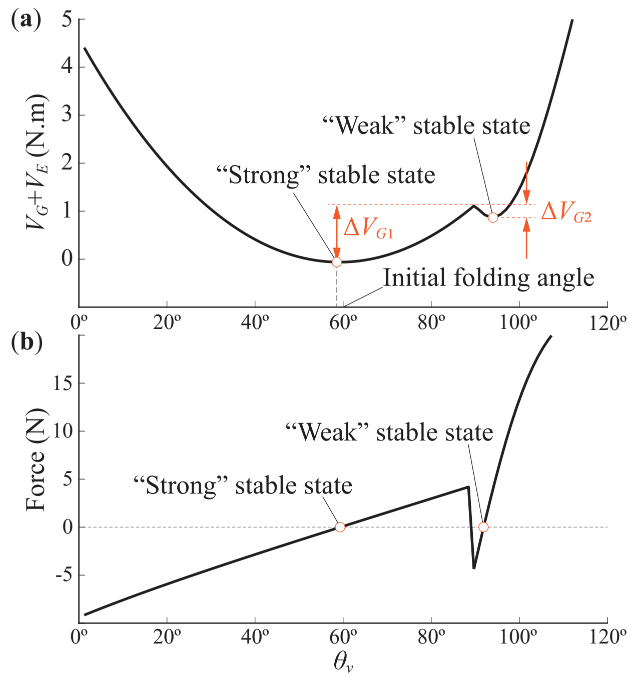

Figure 5.4: The asymmetric bi-stability of the water-bomb origami. (a) The asymmetric elastic potential energy landscape with two different energy barriers (ΔV_{G_1} and ΔV_{G_2}). (b) The reaction force-displacement curve of the origami due to the elastic deformation along the creases.

5.4.2 Dynamic folding from the weak stable state

If the water-bomb origami initially settles at the weak stable state, we can induce an intra-well resonance by exciting it with the corresponding resonance frequency. In this way, the origami can exhibit a large reciprocal folding motion with a small energy input. If the excited origami can overcome the energy barrier ΔV_{G_2}, it can rapidly switch to the other, strong stable state. Moreover, once this switch is complete, the water-bomb will remain in the strong state because 1) the energy barrier of the opposite switch is significantly higher, and 2) the resonance frequency of the strong state is significantly different from the original input frequency (that is, the intra-well resonance stops after the switch).

To experimentally validate this dynamic folding we mount the origami on the shaker and manually set it at the weak stable state initially (Figure 5.2(b)). We excite the shaker with a constant frequency of $\Omega = 15.8$ Hz, which is the experimentally measured intra-well resonance frequency at this stable state. Then, we gradually increase the amplitude of base excitation until the water-bomb "snaps" to the strong stable state. Once the snap occurs, we stop increasing the excitation amplitude (Figure 5.5(a)). The water-bomb origami continues to oscillate around the strong state without switching back to its original configuration. We also replicate the same scenario numerically (Figure 5.5(c, d)). In this simulation, the excitation frequency equals to the experimentally measured resonance frequency, and the excitation amplitude increases linearly over time until the snap-through occurs. It is worth noting that the numerical model predicts a higher base excitation amplitude required for switching. This difference is due to the over-prediction of resonance frequency by the analytical model, as we discussed in the previous subsection. In a different study shown in Figure 5.5(e, f), we repeat the simulation exactly with the numerically predicted resonance frequency ($\Omega = 17$), and observe a much smaller excitation amplitude requirement for switching. Despite these quantitative differences, our model and experiment confirm the feasibility of dynamic folding from the weak stable state to the strong state solely by inducing an intra-well resonance with a small excitation amplitude. Moreover, we can reduce the required excitation magnitude by using this dynamic folding method. That is, the required base displacement to achieve a dynamic folding from the weak to the strong stable state is $A = 1.3mm$, while the required base displacement is significantly higher if we fold the water-bomb quasi-statically ($A = 6.5mm$, Table 5.1).

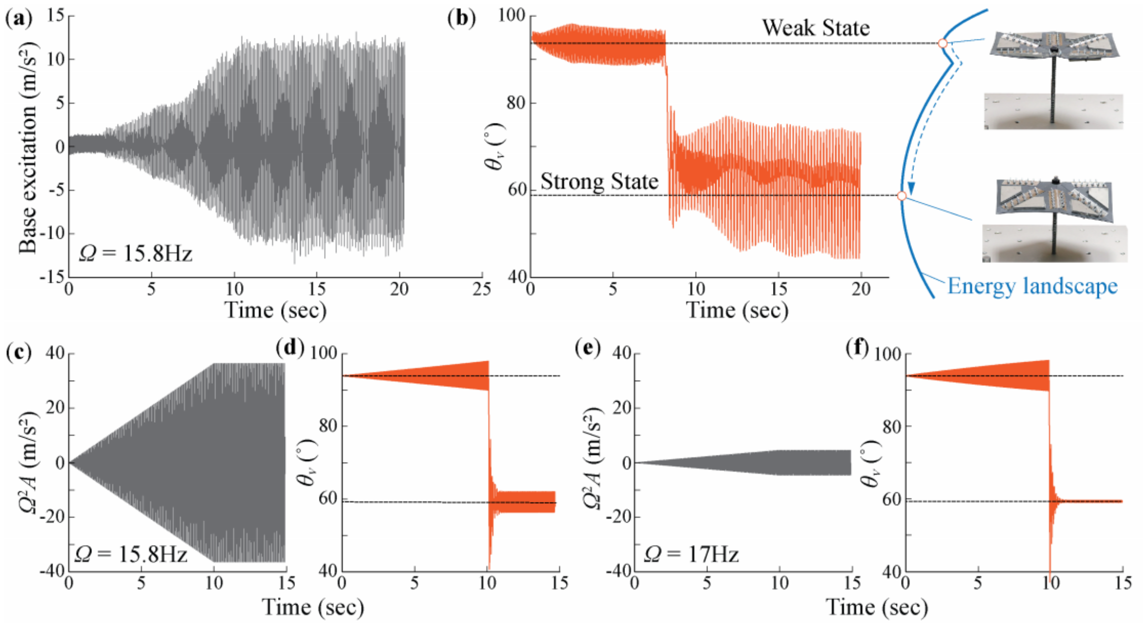

Figure 5.5: Harmonically excited folding from the weak stable state to the strong state. (a) Acceleration of the shaker's base (or central vertex) based on the piezoelectric accelerometer readings. The frequency of excitations here is the experimentally measured resonance frequency from the actual prototype (15.8 Hz). The energy landscape is shown on the right for clarity. (b) Time resposne of θ_v calculated from the laser vibrometer data. (c) The base acceleration from the numerical simulation based on the same excitation frequency of 15.8 Hz. (d) The corresponding time response of θ_v by numerically solving the equation of motion 5.14. (e, f) The base acceleration and time response (θ_v) from a similar numerical simulation using the analytically predicted resonance frequency (17 Hz).

5.4.3 Dynamic folding from the strong stable state

If the water-bomb base origami structure initially settles at the strong stable state, it has to overcome a significantly higher potential energy barrier ΔV_{G_1} to fold to the weak state. Although the intra-well resonance can help the origami to overcome this significant energy barrier, a large amount of energy in the system may lead to an *inter*-well oscillation between the two stable states, which is not desirable for the dynamic folding purpose. To demonstrate this complex nonlinear dynamics, we conduct a parametric study to examine the relationships among the dynamic fold-

Table 5.1: Comparison between the required quasi-static displacement and dynamic excitation amplitude for the dynamic folding between two stable states. Here, the quasi-static displacement is based on the reaction force-displacement curve shown in Figure 5.4.

	Quasi-static	**Dynamic**
Weak to Strong	6.5mm	1.3mm
Strong to Weak	51.1mm	24.2mm

ing behaviors from the strong stable state, potential energy barriers, difference in resonance frequencies, and excitation amplitudes. Figure 5.6(a) shows the numerically predicted frequency responses of water-bomb origami with different stress-free folding angles (θ_{v_0}) around their two stable states, while Figure 5.6(b) shows the corresponding elastic potential energy landscape.

We then excite each water-bomb origami with the resonance frequency of its strong stable state for a range of excitation amplitudes, all from zero initial conditions. Figure 5.6(c) summarizes its overall dynamic behaviors. For every water-bomb design, there exists a small span of excitation amplitude that can generate the desired uni-directional switch (aka. rapidly folding from the strong state to the weak state without switching back). For example, the case (ii) in Figure 5.6(c)—with $\theta_{v_0} = 60°$ and $A =$ 24 mm—exhibits such a dynamic response. Its time response and the corresponding Poincare's map are shown in figure 5.6(d) and (e), respectively. One can observe that the oscillations of this water-bomb origami start from near the strong state, but eventually switch to and remain at the weak stable state.

Any excitation below this span of uni-directional switch is not sufficient to overcome the potential energy barrier, leading to intra-well oscillations only (e.g., the case (i) in 5.6(c-e) with $A = 24$ mm). On the other hand, any excitation above this span would generate an inter-well oscillation. Case (iii) and (iv) 5.6(c, d) are two

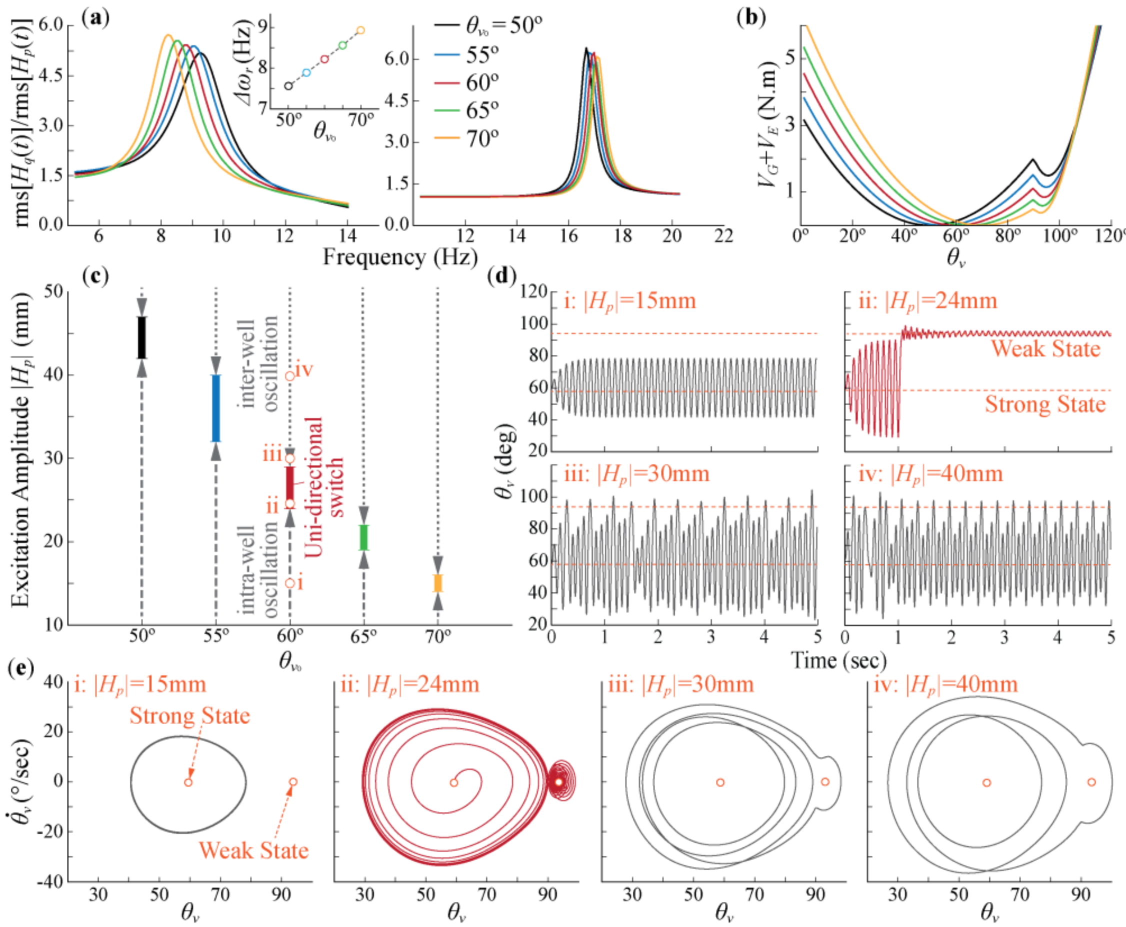

Figure 5.6: Dynamic folding behaviors of the water-bomb base origami from its strong stable state: (a) The numerically predicted frequency responses of water-bomb base origami structures with different stress-free folding angle θ_{v_0}. The small inset figure shows the differences in resonance frequency between the two stable states. (b) The corresponding potential energy landscape. (c) The correlation between stress-free folding angle, excitation amplitude, and the overall response. The desired rapid folding (aka. uni-directional switch) is highlighted. (d) The time responses of four representative cases based on different excitation amplitudes. (e) The corresponding Poincare's map. Note that, except for the case (ii), only steady-state responses are shown in these maps.

examples of this inter-well oscillations. Moreover, one can observe that, although both these two cases show inter-well oscillation, their state-state responses still show marked differences. For example, a period in the steady-state response of case (iii)

($A = 30$ mm) consists of three oscillations around the strong state before one inter-well oscillation, while the responses of the case (iv) ($A = 40$ mm) only involve two oscillations around the strong state before an inter-well oscillation (Figure 5.6(d, e)).

Moreover, there is a clear trade-off between the potential energy barriers and natural frequency differences. As the stress-free folding angle v0 of the water-bomb increases from 50 to 70, the difference in resonance frequencies also increases between the two stable states, however, the energy barrier VG2 decreases. Therefore, as θ_{v_0} increases, the excitation magnitude corresponding to these spans of uni-directional switch decreases, and the width of these spans increases and then decreases. Overall, we observe that a water-bomb origami with $\theta_{v_0} = 55°$ has the most balanced design and the widest excitation span to achieve a uni-directional switch.

Overall, our numerical simulations show that solely using the intra-well resonance to achieve the dynamic folding from the strong stable state to the weak state is possible but quite challenging. That is, the excitation magnitude spans of the uni-directional switch is narrow ($< 10mm$) even with the more optimized origami designs. Moreover, the nonlinear dynamics of the water-bomb base origami are quite sensitive to other uncertainties like initial conditions, fabrication errors, and excessive damping. For example, the actual differences in resonance frequencies are actually less than the prediction shown in Figure 5.3. As a result, we could not achieve a consistent and repeatable fold from the strong stable state to the weak one in the experimental efforts, despite the relatively small differences be- tween the frequency response obtained from experiment and the prediction from numerical simulation. This challenge necessitates an active control strategy, as we detail in the next section.

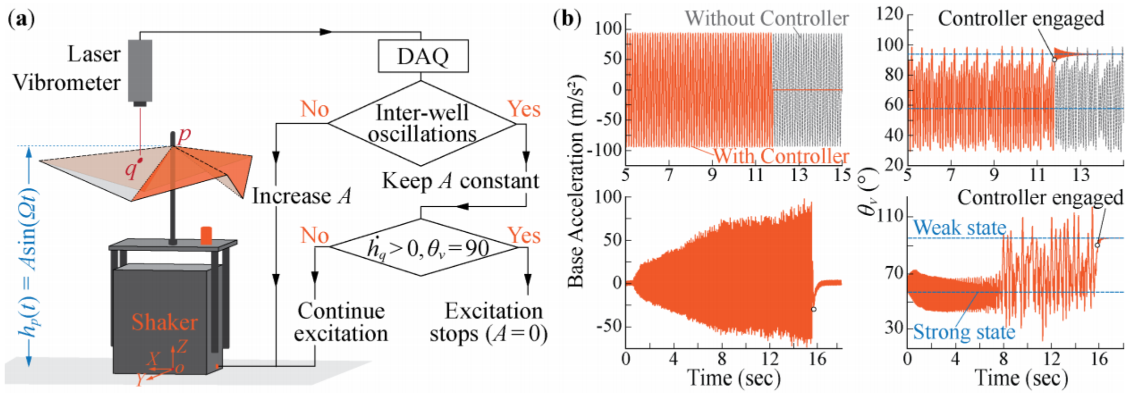

Figure 5.7: The control strategy to achieve a robust and dynamic folding from the strong stable state to the weak state. (a) The flow chart showing the concept and implementation of the controller (b) The controlled base acceleration and water-bomb origami folding angle based on the numerical simulation (top) and experimental validation (below). It is clear that when the controller is engaged, inter-well oscillation is stopped quickly, and the water-bomb settles at the targeted weak stable state.

5.5 Active control strategy for robust folding

In this section, we propose a feedback control strategy that enables us to achieve a robust dynamic folding from the strong stable state of water-bomb origami to the weak state. We show that this strategy is successful when pure dynamic excitation without control only generates inter-well oscillations between the two stable states. The idea of this feedback control strategy seems relatively straightforward. Assuming the water-bomb origami is showing inter-well oscillations due to base excitation, we can cut off this excitation at the moment when the origami is folding toward the weak stable state (aka. $\dot{h}_q > 0$) *and* passing through the flat, unstable equilibrium (aka. $\theta_v = 90°$). In this way, the water-bomb origami should be able to overcome the energy barrier and switch to the weak stable state, but it would not be able to switch back to the strong state due to energy dissipation via damping. Figure 5.7(a) shows the flow chart of this feedback loop based on the proposed control strategy. Figure 5.7(b) shows the numerically simulated folding with this controller.

We experimentally validate the effectiveness of this control strategy on the same water-bomb origami prototype. Figure 5.7(a) shows the flow chart of this feedback loop based on the proposed control strategy. This feedback loop is encoded in a LabVIEW program that uses the laser vibrometer and accelerometer readings as the inputs. The labVIEW program filters out the acceleration data from the accelerometer using a bandpass filter and then integrates it twice to derive the displacement of the shaker's base. Then it calculates the relative displacement of the water-bomb base origami and the shaker by subtracting the derived displacements from the laser vibrometer readings. Finally, it calculates θ_v using this displacement data. In this setup, we excite the water-bomb origami with the intra-well resonance frequency of 8.8 Hz and increase the excitation amplitude until an inter-well oscillation occurs. We then activate the controller, which can automatically detect the threshold of $\dot{h}_q > 0$ and $\theta_v = 0$ and cut ofd the excitation accordingly. In our experiment, this controller can reliably and repeatedly fold the water-bomb origami from the strong stable state to the weak one. Therefore, despite its simplicity, the proposed controller provides an effective approach to complete the bi-directional dynamic folding of the water-bomb origami. Moreover, it is worth noting that the required base displacement to achieve dynamic folding from strong state to the weak state is $A = 24.5$mm, which is much smaller than the excitation amplitude in a quasi-static folding ($A = 51.1$mm, Table 5.1). It is also worth noting that this control algorithm is effective, but can certainly be modified further to increase its efficiency.

5.6 Discussion

Scaling of the harmonically-excited folding strategy: Although this study is based on a water-bomb base origami, the physical insights into harmonically-excited folding and the control strategy certainly apply to other origami or even other structures with similar nonlinear properties. This is because the dynamic folding relies on the asymmetry of the potential energy landscape and the resulting difference in the resonance frequencies between the two stable states. Such asymmetric bi-stability has been demonstrated in other origami designs like the rigid-foldable stacked Miura-Ori [149] and leaf-out pattern [151], as well as the non-rigid foldable Kresling [150] and square twist pattern [152].

It is also worth noting that, although this study focuses on a bi-stable origami, the results could provide some valuable insights into the dynamic folding with more than two stable states (e.g., a waterbomb base assembly with multiple vertices). It is desirable to customize-design the multi-stable origami so that each of its stable states exhibits a unique resonance frequency, and the differences between these frequencies should be significant. Moreover, it is conceivable that a multi-stable origami with complex energy landscape is even more likely to show inter- well oscillations than the bistable water-bomb base, so the active control strategy discussed in this paper (or an improved version of it) will be necessary.

Potential applications: A promising application of the dynamic folding is shape morphing (or deploying). Self-folding origami can serve as the skeleton of light-weight, shape morphing structures that can perform dissimilar tasks optimally [145]. In this case, a low actuation requirement is crucial, so the higher actuation speed and authority (Table 1) of dynamic folding offers a pathway for enhanced morphing performance. Another promising application is origami robotics, especially shape-transforming robots [153]. One can pre-program the bi-stability of origami for different robotic tasks (e.g., the robot can be folded into a small volume for transportation at one stable state and unfolded to perform tasks like locomotion at the other state). Dynamic folding can enable rapid robotic transformations.

Finally, although this study uses a shaker as the source of dynamic input, the required harmonic actuation can also be achieved by other methods depending on the application. It is conceivable that for structural morphing applications, motors and fluidic actuators are applicable. For a smaller-sized origami, one could use external magnetic fields [135] or responsive materials like dielectric elastomers [154]. Note that via dynamic inputs, we could use the responsive materials more effectively than the quasi-static folding.

5.7 Summary and Conclusion

In this study, we examine a dynamic and reversible origami folding method by exploiting the combination of resonance excitation, asymmetric multi-stability, and an active control strategy. The underlying idea is that, by exciting a multi-stable origami at its resonance frequencies, one can induce rapid folding between its different stable equilibria with a much smaller actuation re- quirements than static folding. To this end, we use a bi-stable water-bomb base origami as the archetypal example and, for the first time, formulate a distributed mass–spring model to describe its nonlinear dynamics. Via numerical simulations based on this new model and experimental testing using a proof-of- concept prototype, we characterize the difference in resonance frequencies between the two stable equilibria of the origami. This difference stems from the inherent asymmetry of the water- bomb with respect to its unstable equilibrium at the unfolded flat shape. For example, if the water-bomb initially settles at its weak stable state, one can use a base excitation to induce the intra-well resonance. As a result, the origami would fold and remain at the other stable state even if the excitation does not stop. The origami dynamics near the strong state, on the other hand, is more complicated. The asymmetric energy barrier makes the origami prone to show inter-well oscillation rather than a uni-direction switch. There exist a complex trade-off between the desired uni-directional folding, potential energy barrier, the difference in resonance frequencies, and excitation amplitude.

Therefore, we propose an active feedback control strategy to achieve robust and uni-directional folding from the strong stable state to the weak one. This strategy cuts off the base excitation input when critical dynamic conditions occur. Despite its simplicity, the control strategy is effective for controlling the dynamic folding. We should emphasize that the proposed algorithm can be further modified to enhance performance. For example, we can fully automate the task of detecting inter-well oscillations and sending control signals to cut off shaker input when necessary.

Chapter 6

Physical Reservoir Computing Using Origami Structures for Sensing and Signal Processing

6.1 Abstract

Reservoir computing (RC) is a computational framework suited for temporal/sequential data processing which is derived from several recurrent neural network models. Reservoir computing systems has shown tremendous potentials in temporal pattern classification, prediction, and generation tasks. Recently, physical systems with highly nonlinear dynamic characteristics have been introduced as the physical reservoir computing systems that are capable of performing complex tasks such as computation, pattern generation and control. Witnessing the rich and nonlinear dynamic characteristics of origami structures, in this study we introduce the idea of using origami structures as physical reservoir computing systems and investigate their potentials in sensing and signal processing tasks without relying on external digital

components and signal processing units. The results of this study can advance the state of art and formulate a strategy for constructing mechanically intelligent structures and material systems that can sense the environment, learn from experience and act accordingly, without relying on external controllers and digital components.

6.2 Introduction

Reservoir computing (RC) is a computational framework suited for temporal/sequential data processing which is derived from several recurrent neural network models, including echo state networks (ESNs) [155] and liquid state machines (LSMs) [156]. A reservoir computing system consists of a reservoir for mapping inputs into spatiotemporal patterns in a high-dimensional space by an RNN and a readout for pattern analysis from the high-dimensional states in the reservoir [157]. The reservoir is fixed and only the readout is trained with a simple method such as linear regression and classification [158, 159]. Therefore, the main characteristic that distinguishes reservoir computing from other recurrent neural networks (RNN) is fast learning, which results in low training cost [160]. RC models have been successfully applied to many computational problems, such as temporal pattern classification, prediction, and generation [157].

The role of the reservoir in RC is to nonlinearly transform sequential inputs into a high-dimensional space such that the features of the inputs can be efficiently read out by a simple learning algorithm. Therefore, RNNs can be replaced by other nonlinear dynamical systems as reservoirs [157]. This is the reason behind the recent increasing interest in physical RC using reservoirs based on physical phenomena. Various physical systems, substrates, and devices have been proposed for realizing RC to achieve fast information processing devices with low learning cost. Physical implementation of reservoirs can be achieved using a variety of physical phenomena in the real world, because a mechanism for adaptive changes for training is not necessary [157].

It has been shown that mechanical systems, such as soft and compliant robots, can be used as physical reservoirs. Soft and compliant robots with flexible bodies are difficult to control due to their complex body dynamics compared with rigid robots with stiff bodies. However, such intricate behavior can be harnessed to generate complex nonlinear dynamic behaviors. The ability of physical reservoir computing systems in computation, pattern generation and control has been studied before [157]. For example, a mass–spring network reservoir where mass points are randomly connected to neighboring mass points via nonlinear springs was proposed by Hauser et al. [161]. The input signal is given to some randomly chosen nodes as the external force, inducing nonlinear responses from the mass–spring network. The output signal is obtained as a linear combination of the actual lengths of the springs. Via numerical simulations, they showed the computing power of RC based on the mass–spring network in time series approximation and robot arm tasks. It was shown that by adding feedback loops from the output, the reservoir of a mass–spring network can be applied to pattern generation tasks, which are useful for producing locomotion of robots and biological organisms [162]. In another relevant study, a muscular hydrostat system inspired by octopus limbs was investigated and its motion was successfully learned by an ESN-based controller in a simulation study [163] and in an experimental study using a real robot made of silicone rubber [164]. The computational capability of the soft body was demonstrated in nonlinear system approximations and body dynamics control without an external controller [165, 166].

Recently, it has been shown that origami structures can be utilized as physical reservoirs and its computing power can be harnessed for robotic locomotion generation

[167]. Bhovad and Li, via numerical simulations, proved that origami structures provide a foundation for physical reservoir computing that can complete computation tasks like emulation, pattern generation, and output modulation [167].

In this study we investigate the idea of utilizing the computation power of origami structures for sensing and signal processing tasks. In particular, we are interested in using origami structure itself, via harnessing its highly nonlinear dynamics, as a sensor for observing environmental conditions and a signal processing unit that can perform tasks such as filtering without relying on external digital components.

The vision is to advance the state of art and formulate a strategy for constructing mechanically intelligent structures and material systems with balanced versatility and applicability. Structures that can sense the circumstances, learn from the past experiences, and perform cost-benefit analyses. We believe that origami structures offer a suitable framework to obtain a reservoir computing system that can be used to achieve these goals, as the possess the following characteristics:

1) High-dimensionality: Allowing the reservoir to gather as much information as possible from the input data stream, separating its spatio-temporal dependencies and projecting it onto a high-dimensional state-space.

2) Non-linearity: Where the reservoir acts as a nonlinear filter to map the information from the input stream.

3) Fading memory (or short-term memory): Where the reservoir states are dependent on recent past inputs, but not distant past inputs (damping of the origami structures provide this).

4) Separation property: To classify and segregate different response signals correctly, even with small disturbances or fluctuations. Moreover, if two input time series differed in the past, the reservoir should produce different states at subsequent time points [168].

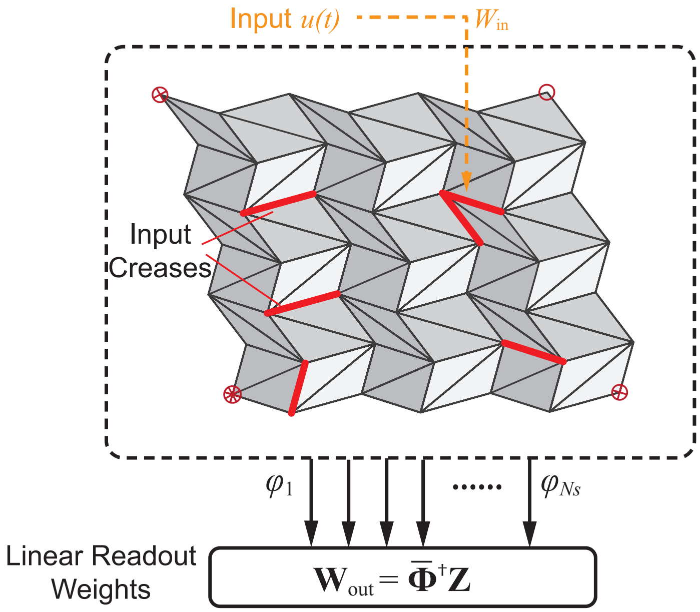

Figure 6.1: The setup of physical reservoir computing with origami. The input creases receive the input signal and the readout weights ($\mathbf{W}_{out}$) are calculated using linear regression after white noise is added to the reservoir state vector $\Phi(t)$.

6.3 The Structure of the Origami Reservoir

In this study, we use the concept of the origami reservoir proposed by Bhovad and Li [167]. The proposed physical reservoir is constructed using the classical Miura-ori sheets. The structure of the reservoir is essentially a periodic tessellation of unit cells, each consisting of four identical quadrilateral facets with crease lengths a and b and an internal sector angle γ (Figure 6.1) [32]. The folded geometry of Miura-ori can be fully defined with a dihedral folding angle $\theta(\in [-\pi/2, \pi/2])$ between the $x-y$ reference plane and its facets. The reservoir size is defined as $n \times m$, where n and m are the number of origami nodes (aka. vertices where crease lines meet) in x and y-directions, respectively. N is the total number of creases in the origami reservoir.

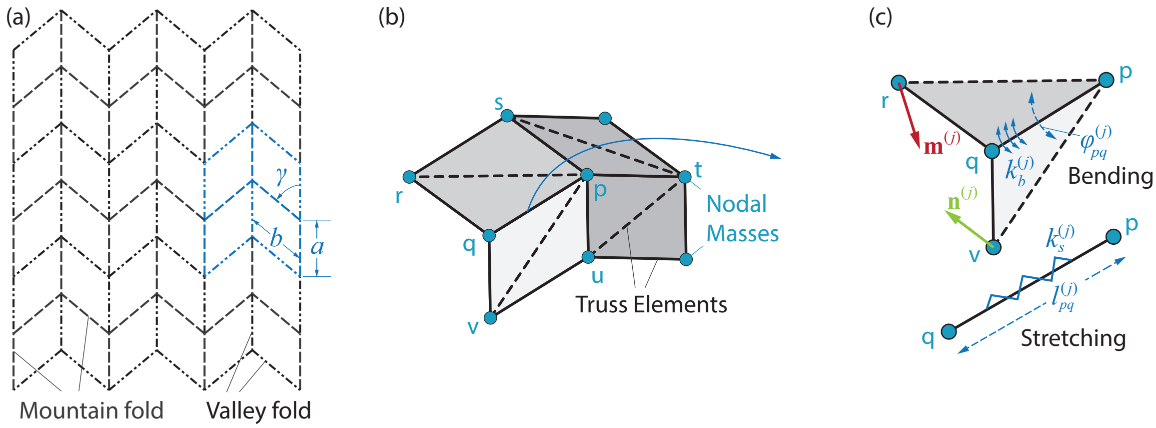

Figure 6.2: The nonlinear truss-frame model for dynamic simulations. (a) The crease pattern of a Miura-Ori origami sheet, with a highlighted unit cell. (b) The distribution of struss elements along the creases and across the facets of a unit cell and the nodal masses at the vertices. (c) Kinematics and mechanics details of the structure required to analyze the bending and stretching along the truss pq. Here, $\mathbf{m}^{(j)}$ and $\mathbf{n}^{(j)}$ are the surface normal vectoes defined by triangles $\triangle pqr$ and $\triangle pqv$ at the current time step, respectively.

6.3.1 Dynamic Model of the Origami Reservoir

In this study, we use the dynamic model of the Miura-ori sheet derived by Bhovad and Li [167]. They adopted and expanded the lattice framework approach to simulate the nonlinear dynamics of the structure. Origami creases of the Miura-ori sheet are represented by pin-jointed stretchable truss elements with prescribed spring coefficient K_s. Folding along the crease line is simulated by assigning torsional spring coefficient K_b (Figure 6.1). The quadrilateral facets are further triangulated with additional truss elements to estimate the facet bending with additional torsional stiffness (typically, the stiffness across the facets is larger than those along the creases). Using this approach allows to discretize the continuous origami sheet into a network of pin-jointed truss elements connected at the nodes [167]. The network of nodes with their interconnections defined by the underlying crease pattern resembles the network of units governed by nonlinear dynamics in a typical reservoir.

The corresponding governing equation of motion of node p can be represented as follows:

$$m_p \ddot{\mathbf{x}}_p{}^{(j)} = \mathbf{F}_p^{(j)}, \tag{6.1}$$

where the superscript (j) refers to the j^{th} time step in the numerical simulation and m_p is the equivalent nodal mass, assuming the mass of the sheet is equally distributed to all its nodes [cite]. $\mathbf{F}_p^{(j)}$ is the summation of all internal and external forces acting on node p and can be represented as follows:

$$\mathbf{F}_p^{(j)} = \sum \mathbf{F}_{s,p}^{(j)} + \sum \mathbf{F}_{b,p}^{(j)} + \mathbf{F}_{d,p}^{(j)} + \mathbf{F}_{a,p}^{(j)} + m_p \mathbf{g}, \tag{6.2}$$

where the five forcing terms on the right hand side represent the forces from truss stretching, crease/facet bending, equivalent damping, external actuation, and gravity, respectively. In what follows we review the formulation of each of the forcing terms developed by Bhovad and Li [167].

Truss stretching forces: Truss elements in the structure can be considered as elastic springs with axial stretching stiffness ($K_s^{(j)} = EA/l^{(j)}$), where EA is the material constant, and $l^{(j)}$ is the length of the truss element at the current time step. The stretching forces from a truss connecting node p and one of its neighbouring nodes q can be represented as follows:

$$\mathbf{F}_{s,p}^{(j)} = -K_s^{(j)} (l_{pq}^{(j)} - l_{pq}^{(0)}) \frac{\mathbf{r}_p^{(j)} - \mathbf{r}_q^{(j)}}{|\mathbf{r}_p^{(j)} - \mathbf{r}_q^{(j)}|}, \tag{6.3}$$

where $l_{pq}^{(0)}$ is the truss length at its initial resting state. $\mathbf{r}_p^{(j)}$ and $\mathbf{r}_p^{(j)}$ are the current position vectors of these two nodes, respectively. Similarly, we can calculate all the stretching forces acting on node p from all the neighbor nodes.

Crease/facet bending forces: The crease folding and facet bending are simulated with torsional spring coefficient ($K_b^{(j)} = k_b l^{(j)}$), where k_b is torsional stiffness per unit length. the force acting on nodes p due to the crease folding along the truss between p and q is:

$$\mathbf{F}_{b,p}^{(j)} = -K_b^{(j)}({}_{pq}^{(j)} - \varphi_{pq}^{(0)})\frac{\partial \varphi_{pq}^{(j)}}{\partial \mathbf{r}_p^{(j)}}, \tag{6.4}$$

where $\varphi_{pq}^{(j)}$ is the current dihedral angle along truss pq (aka. the dihedral angle between the triangles $\triangle pqr$ and $\triangle pqv$ in [fig], and $\varphi_{pq}^{(0)}$ is the corresponding initial value. $\varphi_{pq}^{(j)}$ can be derived as follows:

$$\varphi_{pq}^{(j)} = \eta \arccos\left(\frac{\mathbf{m}^{(j)}.\mathbf{n}^{(j)}}{|\mathbf{m}^{(j)}||\mathbf{n}^{(j)}|}\right) \text{modulo } 2\pi, \tag{6.5}$$

where,

$$\eta = \begin{cases} \text{sign}(\mathbf{m}^{(j)}.\mathbf{r}_{pv}^{(j)}) & \text{if } \mathbf{m}^{(j)}.\mathbf{r}_{pv}^{(j)} \neq 0 \\ 1 & \text{if } \mathbf{m}^{(j)}.\mathbf{r}_{pv}^{(j)} = 0 \end{cases} \tag{6.6}$$

where, $m^{(j)}$ and $n^{(j)}$ are current surface normal vectors of the triangles $\triangle pqr$ and $\triangle pqv$, respectively. It should be noted that to calculate the total crease folding and facet bending forces acting on node q, similar equations apply to trusses connected to this node (e.g., truss pq, pr, ps, pt, pu, and pv in Figure X).

Damping forces: Bhovad and Li have used a formulation developed by Liua and Paulino [125] to calculate the damping forces. The formulation first calculates the average velocity of a node with respect to its neighbor nodes ($\mathbf{v}_{avg}^{(j)}$) to effectively remove the rigid body motion components from the relative velocities and ensures that these components are not damped. Then damping force $\mathbf{F}_{d,p}^{(j)}$ applied on node p

is given by:

$$\mathbf{F}_{d,p}^{(j)} = -c_d^{(j)}(\mathbf{v}_p^{(j)} - \mathbf{v}_{avg}^{(j)}) \tag{6.7}$$

$$c_d^{(j)} = 2\zeta\sqrt{K_s^{(j)} m_p} \tag{6.8}$$

where $c_d^{(j)}$ is the equivalent damping coefficient, and ζ is the damping ratio.

Actuation force: The input creases in the origami reservoir receive input signal $u(t)$, required for emulation, output modulation and sensing tasks. There are many methods to implement actuation to deliver input $u(t)$ to the reservoir. For example, the actuation can take the form of nodal forces on a mass-spring-damper network [161, 162], motor generated base rotation on octopus-inspired soft arm [165], or spring resting length changes in a tensegrity structure [169]. In origami, the actuation can take the form of moments that can fold or unfold the selected creases [167]. Here, it is assumed that the resting angle $\varphi^{(0)}$ of the input creases change, in response to the actuation at every step, to a new equilibrium $\varphi_{a,0}^{(j)}$ in that:

$$\varphi_{a,0}^{(j)} = W_{in} tanh(u^{(j)}) + \varphi^{(0)}, \tag{6.9}$$

where, W_{in} is the input weight associated with the input creases which are assigned before training and remain fixed after that. The magnitude of W_{in} is selected such that $\varphi_{a,0}^{(j)} \in [0, 2\pi]$ and consistent with the folding angle assignment.

In this study, the governing equations of motion are solved using MATLAB's ode45 solver with 10^{-3} second time-steps. Although the governing equations of motion use nodal displacement $\mathbf{x}^{(j)}$ as the independent variables, we use the dihedral crease angles $\varphi^{(j)}$ as the *reservoir state* variables to characterize the reservoir's time response, because measuring crease angles is easier to implement by embedded sensors. The relationship between $\varphi^{(j)}$ and $\mathbf{x}^{(j)}$ can be directly calculated from the governing kinematic relationships.

6.3.2 Training the Origami Reservoir

Similar to the input creases, sensor creases can be designated for measuring the reservoir states. In this study, we denote N_i and N_s as the number of input creases and sensor creases, respectively. Typically, the input creases are a small subset of all origami creases of the reservoir (i.e., $N_i < N$). However, the sensor creases can be all of the origami creases (i.e., $N_s = N$) or a small subset as well (i.e., $N_s < N$). Once the selection of all the input and sensor creases is finalized, we can proceed to the computing. In what follows we discuss the required steps of training the reservoir for sensing and signal processing tasks.

The objective of the training phase is to obtain the readout weights W_i corresponding to every reservoir state (aka. the dihedral angles of the sensor creases). Suppose we want to the train the reservoir to generate a nonlinear time-series $z(t)$ (aka. the reference output). The reservoir states $\varphi^{(j)}$ at every time step are measured and then compiled into a matrix $\mathbf{\Phi}$.

Once the numerical simulation is over, we segregate the reservoir state matrix $\mathbf{\Phi}$ into washout step, training step, and testing step. The washout step data is discarded to eliminate the initial transient responses. We then calculate the output readout weights W_i using the training step data via simple linear regression:

$$\mathbf{W}_{out} = [\mathbf{1}\ \mathbf{\Phi}]^{+}\mathbf{Z} \tag{6.10}$$

where, $[.]^{+}$ refers to the Moore-Penrose pseudo-inverse to accomodate nonsqure matrix. **1** is a column of ones for calculating the bias term $W_{out,0}$. $\mathbf{Z}$ contains the reference signals at each time step, and it is a matrix if more than one reference are present. Finally, we use testing step date to verify reservoir performance. It is worth noting that in the model a white noise of amplitude 10^{-3} is superimposed on the reservoir state matrix during training to ensure the robustness of the readout results against imperfections, external perturbations, and instrument noise in real-world applications [167].

6.4 Sensing and Signal Processing Using Origami Reservoir

In this section, we use the origami reservoir to sense the input signal to the system, and apply a low-pass and a band-pass filter to the input signal. The baseline variables for the origami geometric design, material properties, and reservoir parameters for this study are given in Table 6.1.

6.4.1 Sensing Task

The main objective of the sensing task is to sense or observe the input signal to the origami reservoir. In order to achieve this, we excite the reservoir by sending the input function $u(t)$ to the input creases and train it to find the readout weights via linear regression. Here, $u(t)$ is a single-frequency periodic function of form $Asin(\omega t)$ and the target function is exactly the same. Essentially, we want to train the reservoir using different periodic functions, such that it can reproduce, or sense, any unknown periodic input signal using the readout weights found in the training step. In order to achieve this, we use a 9×9 Miura-Ori reservoir and excite it from zero initial conditions

Table 6.1: Design of a baseline origami reservoir for the sensing and signal processing tasks.

Parameters	**Value**
Nodal Mass	7 g
k_s	100 N/m
k_c	0.2525 N/m.rad
K_f	10 N/m
ζ	0.2
a	16 mm
b	10 mm
γ	60°
θ_0	60°
a	100 N/m
No. of sensors	N
No. of input creases	0.2N

an train it for 50 seconds with a combination of 20 different random amplitudes in which $A \in [1, 100]$ and 25 different random frequencies in which $\omega \in [1, 50]$. The first 25 seconds of the data has been discarded as the washout step and the next 25 seconds has been used to derive the optimum static readout weights. Figure 6.3(a) shows the performance of the origami reservoir in sensing an unknown input signal, where the amplitude and the frequency of excitation are not in the training sets. It is clear that the origami reservoir can successfully capture the input signal and rebuild it using the derived static readout weights. We also analyzed the effect of the size of the origami reservoir on the performance of the reservoir in sensing task in terms of normalized mean square error (NSME) of the predicted signal. Here the size of origami reservoir refers to the number of nodes in x and y direction. One can clearly observe that increasing the size of the reservoir enhances its performance in sensing as the degree of complexity and nonlinearity of the response increases.

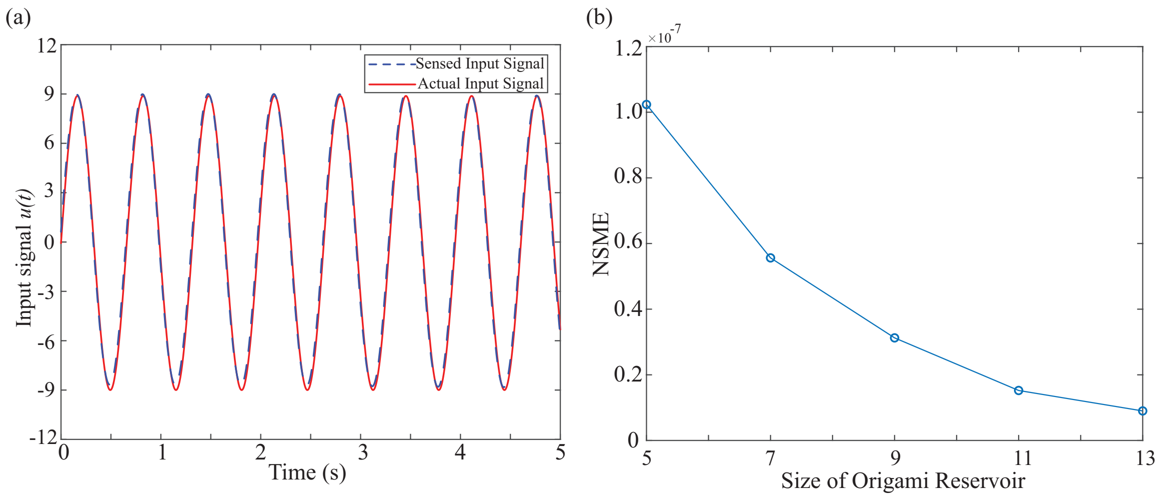

Figure 6.3: Using origami reservoir for sensing the input signal. (a) The performance of a 9×9 origami reservoir in sensing an input signal ($u(t) = 9sin(2\pi(3.8)t)$). The amplitude and the frequency of the input signal are not in the training set. (b) The effect of the size of the reservoir on the normalized mean sqaure error (NSME) of the sensed signal.

6.4.2 Low-Pass Filter Task

In this subsection, we investigate the feasibility of using the origami reservoir as a low-pass filter on the input signals to the reservoir. In order to achieve this, we excite the reservoir by sending the input function $u(t)$ to the input creases and train it to find the readout weights via linear regression. Here, $u(t)$ is a periodic function containing high-frequency white noise of form $u(t) = Asin(\omega t) + HFWN(t)$, where $HFWN(t)$ stands for high frequency white noise and the target function is $LP[u(t)]$, where $LP[\,]$ represents the low-pass filter operation. Essentially, we want to train the reservoir using different periodic functions, such that it can act as a low-pass filter on any unknown periodic input signal using the readout weights found in the training step.

Figure 6.4(a) shows the geometry of a 11×11 origami reservoir used in this task. The input creases of the reservoir are highlighted in red. Figure 6.4(b) and (c)

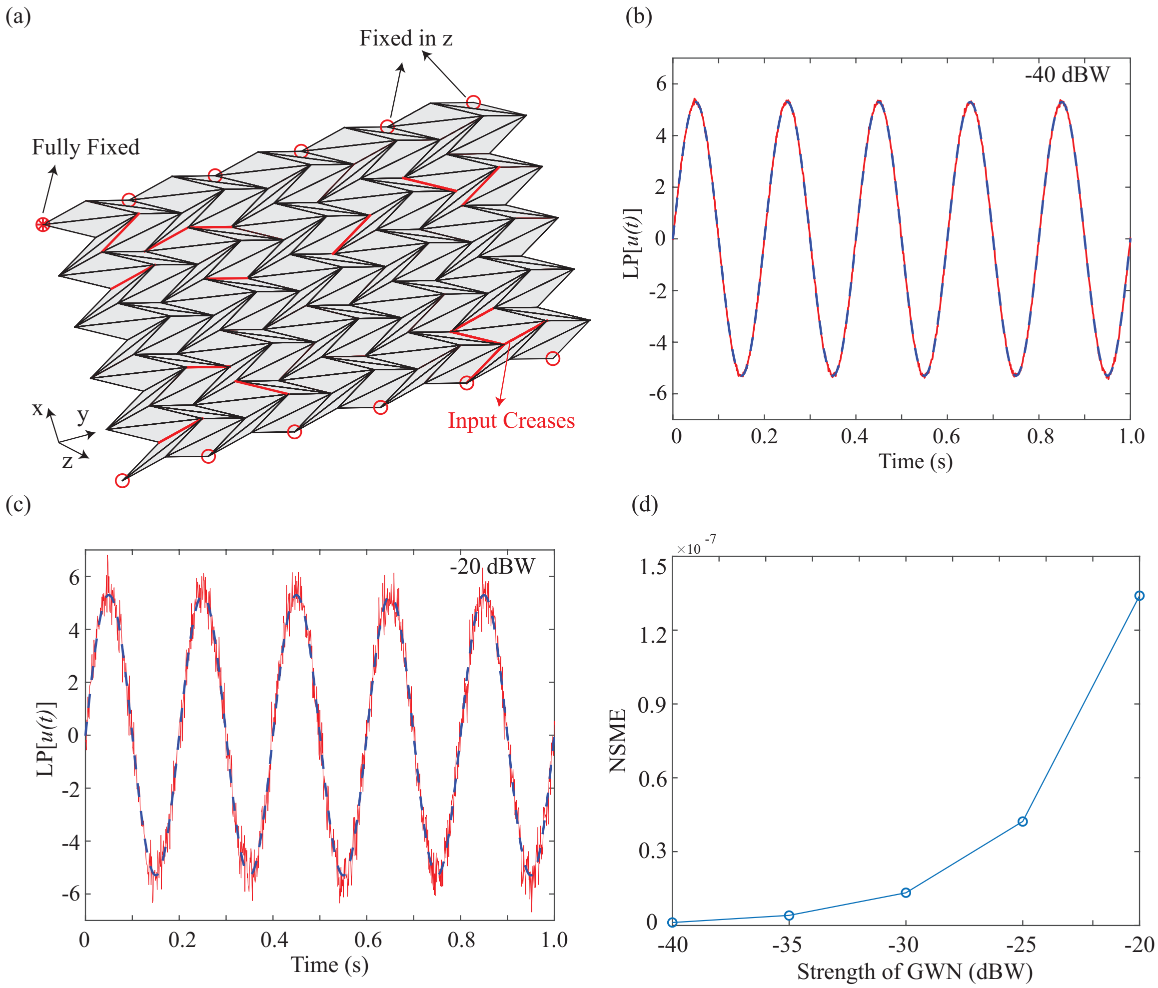

Figure 6.4: Using origami reservoir a low-pass filter on the input signal. (a) The gometry of a 11×11 origami reservoir used in this task. The input creases are highlighted in red. (b) The performance of the origami reservoir in low-pass filter task on the input signal (red), where a high frequency Gaussian white noise of strength -40dBW is injected to the single-periodic input signal. (c) ask. The input creases are highlighted in red. (b) The performance of the origami reservoir in low-pass filter task on the input signal (red), where a high frequency Gaussian white noise of strength -20dBW is injected to the single-periodic input signal. (d) The performance of the origami reservoir as a low-pass filter on noisy signals with different levels of noise.

show the performance of the reservoir as a low-pass filter on a noisy signal constructed as a summation of a single-periodic input signal and high frequency Gaussian white noise of two different levels. We also analyzed the effect of the strength of the noise on

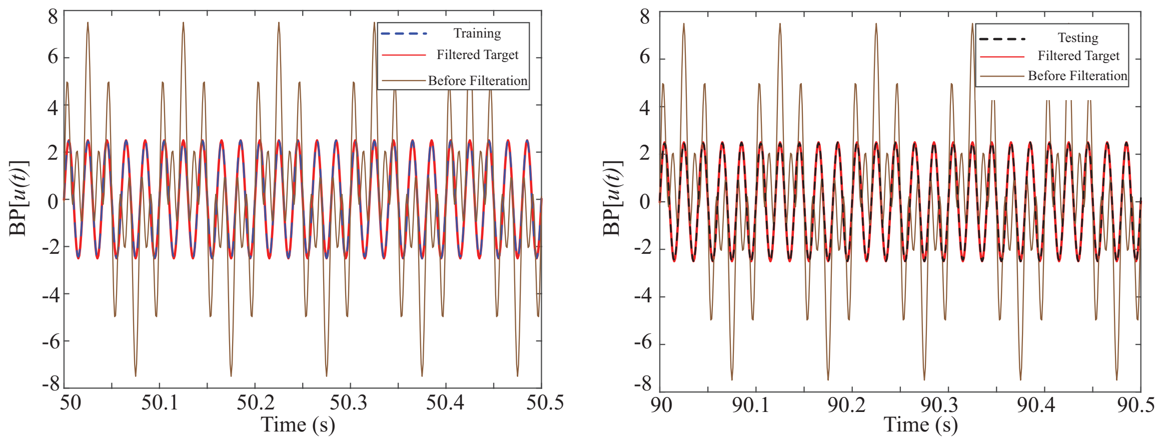

Figure 6.5: Band-pass filter emulation task using origami reservoir. (a) Training the reservoir as a band-pass filter on an input signal consisted of three different ranges of frequencies. (b) Testing the performance of the reservoir in emulating the band-pass filter.

the performance of the reservoir in terms of normalized mean square error (NSME) in figure 6.4(d). Therefore, one can clearly observe that the origami reservoir can be successfully trained to be used as a low-pass filter on the single-periodic input signals.

6.4.3 Band-Pass Filter Task

In this subsection, we investigate the feasibility of using the origami reservoir as a band-pass filter on the input signals to the reservoir. To this end, we use a 11×11 Miura-Ori reservoir and excite it with an input signal consisted of three different frequencies: 1) low frequency, 2) medium frequency and 3) high frequency. The reservoir is excited from zero initial conditions and is trained for 100 seconds. We discard the first 50 seconds of data as the washout step, use the data from the next 40 seconds to calculate the optimum static readout weights, and then use the last 10 seconds of data to assess the performance of the reservoir as a band-pass filter. The objective of this task is to capture the medium-range frequency.

Figures 6.5(a) and (b) clearly show that the origami can be successfully trained to emulate a band-pass filter and capture the medium frequency of an input signal. It should be noted that although this task was an emulation of a band-pass filter, the training procedure for a broader range of frequencies and amplitudes is the same as the sensing and low-pass filter task, but it requires a more comprehensive training data, as the reservoir deals with three different ranges of frequencies here. However, the emulation results are promising and the comprehensive training of the reservoir will be the subject of further studies.

6.5 Discussion and Conclusion

In this study, we investigate the sensing and signal-processing capabilities of physical reservoir computing using origami via numerical simulations and few parametric studies. We demonstrate that the highly nonlinear dynamics and complex behavior of a Miura-Ori origami along with its fading memory property makes it a suitable platform for physical reservoir computing. Nonlinear patterns can be embedded into the origami reservoir, and the resulting pattern generation is robust against external disturbances and recoverable under different initial conditions, proving separation property [167]. We use a dynamic model based on truss-frame discretization approach developed by Bhovad and Li [167] to study the behavior of the origami reservoir and train it for the aforementioned tasks. We show that the origami reservoir successfully performs sensing and signal processing tasks such as low-pass and band-pass filtering on input signals. We also investigated the effect of the size of the origami reservoir on the sensing performance and the performance of the system as a low-pass filter under different levels of noise. Further parametric studies can enrich our vision of the linkage between the design of the physical reservoir and its computing performance.

The outcome of this research can pave the way for a new generation of mechanically intelligent structures or soft robots that don't rely on external digital components for sensing. For example, a soft crawling robot might be able to use its complex dynamics to sense the environment and the terrain which it is crawling on and decide whether it is necessary to change its locomotion gait whenever there is a change in the surface. As another example we might expect a new generation of swimming robots that can use the complex dynamic interaction between their body and the swimming environment to observe the objects in the environment and sense the distance to the external objects and whether it's necessary to maneuver to avoid collision.

The results of this study can advance the state of art and formulate a strategy for constructing mechanically intelligent structures and material systems that can sense the environment, learn from experience and act accordingly, without relying on external controllers and digital components.

Chapter 7

Conclusion

Origami has found various engineering applications, in recent years. Many of these origami-inspired applications have exploited the kinematics of folding. Folding can offer sophisticated shape transformations that are yet programmable which are served as guidelines for many design innovations. In addition, origami structures have tremendous unique advantages including infinite design space, excellent deformability and shape reconfigurability and flat-foldability. The increasingly diverse and vastly expanding applications of origami have encouraged researchers to study the mechanical properties of folded structures as well, over the past decade. This has led to emergence of a new category of metamaterials and meta-structures called *architected origami materials*. The combination of elastic energy in the deformed facets and creases, and their complex spacial distributions, impart the architected origami materials with various programmable and even unorthodox mechanical properties such as multistability or structural auxetic effects.

Despite the significant research progress, most of the previous studies on Origami have mainly focused on kinematics or static/quasi-static characteristics of origami folding. Origami folding, on the other hand, could be a dynamic process.

The intricate nonlinear elastic properties of origami structures can lead to interesting dynamic characteristics and applications. Nevertheless, studying the dynamics of folding is still a nascent field and there are only a few researches conducted in this area.

Dynamics of reciprocal origami folding can be viewed from two different perspectives. In the first perspective, the main objective is to program or create new mechanical properties in the structure, by introducing appropriate folds, to create the desired mechanical properties for a specific dynamic application. The second perspective on the other hand, focuses on studying the behavior of the origami structure under different dynamic excitations. This dissertation sets out to expand our knowledge of the fundamentals of origami folding dynamics by conducting three different studies. We investigate the feasibility of using fluidic origami for low frequency vibration isolation and the effect of utlizing origami folding techniques to enhance the performance of a jumping mechanism as two potential dynamic application of origami folding. In addition, we uncover the underlying dynamic characteristics of a bi-stable origami structure and show that how dynamic excitations can be used to fold the structure between its stable states.

Witnessing the rich and nonlinear dynamic characteristics of origami structures, in this dissertation we introduce the idea of using origami structures as physical reservoir computing systems and investigate their potentials in sensing and signal processing tasks without relying on external digital components and signal processing units. Although this is a preliminary study on potential capabilities of origami structures as physical reservoirs, it can certainly enrich our vision of the smart structures and materials to create a generation of multi-functional structures or metamaterials that can exhibit programmable properties or mechanical intelligence. The long-terms research vision would be to realize mechanical metamaterials that can adapt their properties to the environmental conditions; soft robotic exoskeletons that can perform control tasks without any digital components; or metamaterials and meta-structures that can perform logical operations, store and process information using changes in their morphology.

Results of these studies can open up new avenues in the field of origami folding dynamics and may lead to emergence of a novel category of metamaterials and meta-structures with embedded dynamic functionalities.

References

[1] M. McArthur and R. J. Lang, *Folding paper: The infinite possibilities of Origami*. Tuttle Publishing, 2013.

[2] E. D. Demaine and J. O'Rourke, *Geometric folding algorithms: linkages, origami, polyhedra*. Cambridge university press, 2007.

[3] E. R. Adrover, *Deployable structures*. Laurence King Publishing London, 2015.

[4] M. Buchanan, "Physics under the fold," *Nature Physics*, vol. 13, no. 4, pp. 318–318, 2017.

[5] T. R. Lezon, J. R. Banavar, and A. Maritan, "The origami of life," *Journal of Physics: Condensed Matter*, vol. 18, no. 3, p. 847, 2006.

[6] D. Dureisseix, "An overview of mechanisms and patterns with origami," *International Journal of Space Structures*, vol. 27, no. 1, pp. 1–14, 2012.

[7] E. A. Peraza-Hernandez, D. J. Hartl, R. J. Malak Jr, and D. C. Lagoudas, "Origami-inspired active structures: a synthesis and review," *Smart Materials and Structures*, vol. 23, p. 094001, 9 2014.

[8] A. Lebée, "From folds to structures, a review," *International journal of space structures*, vol. 30, no. 2, pp. 55–74, 2015.

[9] M. J. Harrington, K. Razghandi, F. Ditsch, L. Guiducci, M. Rueggeberg, J. W. C. Dunlop, P. Fratzl, C. Neinhuis, and I. Burgert, "Origami-like unfolding of hydro-actuated ice plant seed capsules," *Nature Communications*, vol. 2, p. 337, 6 2011.

[10] D. De Focatiis and S. Guest, "Deployable membranes designed from folding tree leaves," *Philosophical Transactions of the Royal Society of London. Series A: Mathematical, Physical and Engineering Sciences*, vol. 360, no. 1791, pp. 227–238, 2002.

[11] T. Tachi, "Freeform rigid-foldable structure using bidirectionally flat-foldable planar quadrilateral mesh," in *Advances in Architectural Geometry* (C. Ceccato, L. Hesselgren, M. Pauly, H. Pottmann, and J. Wallner, eds.), pp. 87–102, Vienna, Austria: Springer Vienna, 1 2010.

[12] T. Tachi, "Origamizing polyhedral surfaces," *IEEE Transactions on Visualization and Computer Graphics*, vol. 16, no. 2, pp. 298–311, 2010.

[13] S. Waitukaitis and M. van Hecke, "Origami building blocks: Generic and special four-vertices," *Physical Review E*, vol. 93, p. 023003, 2 2016.

[14] L. Xu, T. C. Shyu, and N. A. Kotov, "Origami and kirigami nanocomposites," *Acs Nano*, vol. 11, no. 8, pp. 7587–7599, 2017.

[15] F. Cavallo and M. G. Lagally, "Nano-origami: Art and function," *Nano Today*, vol. 10, no. 5, pp. 538–541, 2015.

[16] V. B. Shenoy and D. H. Gracias, "Self-folding thin-film materials: From nanopolyhedra to graphene origami," *Mrs Bulletin*, vol. 37, no. 9, pp. 847–854, 2012.

[17] S. Felton, M. Tolley, E. Demaine, D. Rus, and R. Wood, "A method for building self-folding machines," *Science*, vol. 345, pp. 644–646, 8 2014.

[18] A. Firouzeh and J. Paik, "Robogami: A fully integrated low-profile robotic origami," *Journal of Mechanisms and Robotics*, vol. 7, no. 2, 2015.

[19] A. Pagano, T. Yan, B. Chien, A. Wissa, and S. Tawfick, "A crawling robot driven by multi-stable origami," *Smart Materials and Structures*, vol. 26, no. 9, p. 094007, 2017.

[20] H. Fang, Y. Zhang, and K. Wang, "Origami-based earthworm-like locomotion robots," *Bioinspiration & biomimetics*, vol. 12, no. 6, p. 065003, 2017.

[21] C. L. Randall, E. Gultepe, and D. H. Gracias, "Self-folding devices and materials for biomedical applications," *Trends in Biotechnology*, vol. 30, pp. 138–146, 2012.

[22] M. Johnson, Y. Chen, S. Hovet, S. Xu, B. Wood, H. Ren, J. Tokuda, and Z. T. H. Tse, "Fabricating biomedical origami: a state-of-the-art review," *International journal of computer assisted radiology and surgery*, vol. 12, no. 11, pp. 2023–2032, 2017.

[23] M. Schenk, A. D. Viquerat, K. A. Seffen, and S. D. Guest, "Review of inflatable booms for deployable space structures: packing and rigidization," *Journal of Spacecraft and Rockets*, vol. 51, pp. 762–778, 4 2014.

[24] S. A. Zirbel, R. J. Lang, M. W. Thomson, D. A. Sigel, P. E. Walkemeyer, B. P. Trease, S. P. Magleby, and L. L. Howell, "Accommodating thickness in origami-based deployable arrays," *Journal of Mechanical Design*, vol. 135, p. 111005, 10 2013.

[25] I. Ario, M. Nakazawa, Y. Tanaka, I. Tanikura, and S. Ono, "Development of a prototype deployable bridge based on origami skill," *Automation in Construction*, vol. 32, pp. 104–111, 2013.

[26] H. Fang, S. Li, H. Ji, and K. W. Wang, "Dynamics of a bistable miura-origami structure," *Physical Review E*, vol. 95, p. 052211, 5 2017.

[27] S. Li, H. Fang, S. Sadeghi, P. Bhovad, and K.-W. Wang, "Architected origami materials: How folding creates sophisticated mechanical properties," *Advanced Materials*, vol. 31, p. 1805282, 2 2019.

[28] A. A. Evans, J. L. Silverberg, and C. D. Santangelo, "Lattice mechanics of origami tessellations," *Physical Review E*, vol. 92, no. 1, p. 013205, 2015.

[29] V. Brunck, F. Lechenault, A. Reid, and M. Adda-Bedia, "Elastic theory of origami-based metamaterials," *Physical Review E*, vol. 93, no. 3, p. 033005, 2016.

[30] Z. Y. Wei, Z. V. Guo, L. Dudte, H. Y. Liang, and L. Mahadevan, "Geometric mechanics of periodic pleated origami," *Physical review letters*, vol. 110, no. 21, p. 215501, 2013.

[31] F. Lechenault, B. Thiria, and M. Adda-Bedia, "Mechanical response of a creased sheet," *Physical review letters*, vol. 112, no. 24, p. 244301, 2014.

[32] M. Schenk and S. D. Guest, "Geometry of miura-folded metamaterials," *Proceedings of the National Academy of Sciences*, vol. 110, pp. 3276–3281, 2 2013.

[33] H. Yasuda and J. Yang, "Reentrant origami-based metamaterials with negative poisson's ratio and bistability," *Physical Review Letters*, vol. 114, no. 18, pp. 1–5, 2015.

[34] H. Fang, S. Li, H. Ji, and K. W. Wang, "Uncovering the deformation mechanisms of origami metamaterials by introducing generic degree-four vertices," *Physical Review E*, vol. 94, p. 043002, 10 2016.

[35] S. Li and K. W. Wang, "Fluidic origami: a plant-inspired adaptive structure with shape morphing and stiffness tuning," *Smart Materials and Structures*, vol. 24, no. 10, p. 105031, 2015. 74.

[36] H. Yasuda, C. Chong, E. G. Charalampidis, P. G. Kevrekidis, and J. Yang, “Formation of rarefaction waves in origami-based metamaterials,” *Physical Review E*, vol. 93, p. 043004, 4 2016.

[37] S. Ishida, K. Suzuki, and H. Shimosaka, “Design and experimental analysis of origami-inspired vibration isolator with quasi-zero-stiffness characteristic,” *Journal of Vibration and Acoustics*, vol. 139, p. 051004, 6 2017.

[38] S. Ishida, H. Uchida, H. Shimosaka, and I. Hagiwara, “Design and numerical analysis of vibration isolators with quasi-zero-stiffness characteristics using bistable foldable structures,” *Journal of Vibration and Acoustics*, vol. 139, p. 031015, 4 2017.

[39] N. Kidambi and K. Wang, “Dynamics of kresling origami deployment,” *Physical Review E*, vol. 101, no. 6, p. 063003, 2020.

[40] H. Wu, H. Fang, L. Chen, and J. Xu, “Transient dynamics of a miura-origami tube during free deployment,” *arXiv preprint arXiv:2005.07340*, 2020.

[41] C. Liu and S. M. Felton, “Transformation dynamics in origami,” *Physical review letters*, vol. 121, p. 254101, 2018.

[42] S. Li and K. W. Wang, “Fluidic origami with embedded pressure dependent multi-stability: a plant inspired innovation,” *J R Soc Interface*, vol. 12, no. 111, pp. 20150639–, 2015.

[43] E. S. Andersen, M. Dong, M. M. Nielsen, K. Jahn, R. Subramani, W. Mamdouh, M. M. Golas, B. Sander, H. Stark, C. L. P. Oliveira, J. S. Pedersen, V. Birkedal, F. Besenbacher, V. K. Gothelf, and J. Kjems, “Self-assembly of a nanoscale dna box with a controllable lid,” *Nature*, vol. 459, pp. 73–76, 5 2009.

[44] H. Dietz, S. M. Douglas, and W. M. Shih, “Folding dna into twisted and curved nanoscale shapes,” *Science*, vol. 325, no. 5941, pp. 725–730, 2009.

[45] Y. Ke, J. Sharma, M. Liu, K. Jahn, Y. Liu, and H. Yan, “Scaffolded dna origami of a dna tetrahedron molecular container,” *Nano Letters*, vol. 9, no. 6, pp. 2445–2447, 2009.

[46] W. M. Shih and C. Lin, “Knitting complex weaves with dna origami,” *Current Opinion in Structural Biology*, vol. 20, no. 3, pp. 276–282, 2010.

[47] K. Kaino, K. Yajima, and N. Chiba, “Cg image generation of flower arrangement,” *Science*, pp. 207–212, 2000.

[48] T. Street, “Deployable membranes designed,” *Philosophical Transactions of the Royal Society A*, vol. 360, no. 1791, pp. 227–238, 2002.

[49] Y. Yoshimura, "On the mechanism of buckling of a circular cylindrical shell under axial compression," *The reports of the Institute of Science and Technology University of Tokyo*, 1951.

[50] S. Kamrava, D. Mousanezhad, H. Ebrahimi, R. Ghosh, and A. Vaziri, "Origami-based cellular metamaterial with auxetic, bistable, and self-locking properties," *Scientific Reports*, vol. 7, p. 46046, 4 2017. 66.

[51] K. Miura, "Method of packaging and deployment of large membranes in space," *The Institute of Space and Astronautical Science report*, vol. 618, pp. 1–9, 1985.

[52] J. H. Na, A. A. Evans, J. Bae, M. C. Chiappelli, C. D. Santangelo, R. J. Lang, T. C. Hull, and R. C. Hayward, "Programming reversibly self-folding origami with micropatterned photo-crosslinkable polymer trilayers," *Advanced Materials*, vol. 27, pp. 79–85, 1 2015.

[53] K. Kuribayashi, K. Tsuchiya, Z. You, D. Tomus, M. Umemoto, T. Ito, and M. Sasaki, "Self-deployable origami stent grafts as a biomedical application of ni-rich tini shape memory alloy foil," *Materials Science and Engineering: A*, vol. 419, pp. 131–137, 3 2006.

[54] Z. Song, T. Ma, R. Tang, Q. Cheng, X. Wang, D. Krishnaraju, R. Panat, C. K. Chan, H. Yu, and H. Jiang, "Origami lithium-ion batteries," *Nature Communications*, vol. 5, pp. 1–6, 2014.

[55] K. C. Cheung, T. Tachi, S. Calisch, and K. Miura, "Origami interleaved tube cellular materials," *Smart Materials and Structures*, vol. 23, p. 094012, 8 2014. 73.

[56] M. Eidini, "Zigzag-base folded sheet cellular mechanical metamaterials," *Extreme Mechanics Letters*, vol. 6, pp. 96–102, 2016.

[57] T. Tachi, "Rigid foldable thick origami," in *Origami 5* (P. Wang-Iverson, R. J. Lang, and M. Yim, eds.), vol. 5, pp. 253–264, Boca Raton, FL, USA: A K Peters/CRC Press, 1 ed., 1 2011.

[58] M. Eidini and G. H. Paulino, "Unraveling metamaterial properties in zigzag-base folded sheets," *Science advances*, vol. 1, no. 8, p. e1500224, 2015.

[59] H. Fang, S. Li, and K. W. Wang, "Self-locking degree-4 vertex origami structures," *Proceedings of the Royal Society A: Mathematical, Physical and Engineering Science*, vol. 472, p. 20160682, 11 2016. 77.

[60] S. Sengupta and S. Li, "Harnessing the anisotropic multi-stability of stacked-origami mechanical metamaterials for elastic modulus programming," *Journal of Intelligent Materials Systems and Structures*, 2018.

[61] S. Li, H. Fang, and K. W. Wang, "Recoverable and programmable collapse from folding pressurized origami cellular solids," *Physical Review Letters*, vol. 117, no. 11, pp. 1–5, 2016. 70.

[62] K. Inamoto and S. Ishida, "Improved feasible load range and its effect on the frequency response of origami-inspired vibration isolators with quasi-zero-stiffness characteristics [1]," *Journal of Vibration and Acoustics*, vol. 141, no. 2, p. 021004, 2018.

[63] S. Sadeghi and S. Li, "Harnessing the quasi-zero stiffness from fluidic origami for low frequency vibration isolation," in *ASME 2017 Conference on Smart Materials, Adaptive Structures and Intelligent Systems*, American Society of Mechanical Engineers Digital Collection, 2017.

[64] W. Thomson, *Theory of vibration with applications*. CrC Press, 2018.

[65] A. Carrella, M. J. Brennan, and T. P. Waters, "Static analysis of a passive vibration isolator with quasi-zero-stiffness characteristic," *Journal of Sound and Vibration*, vol. 301, no. 3-5, pp. 678–689, 2007.

[66] A. Carrella, *Passive vibration isolators with high-static-low-dynamic-stiffness*. PhD thesis, University of Southampton, 2008.

[67] I. Kovacic, M. J. Brennan, and T. P. Waters, "A study of a nonlinear vibration isolator with a quasi-zero stiffness characteristic," *Journal of Sound and Vibration*, vol. 315, no. 3, pp. 700–711, 2008.

[68] B. A. Fulcher, D. W. Shahan, M. R. Haberman, C. Conner Seepersad, and P. S. Wilson, "Analytical and experimental investigation of buckled beams as negative stiffness elements for passive vibration and shock isolation systems," *Journal of Vibration and Acoustics*, vol. 136, p. 031009, 4 2014.

[69] C. M. Lee, V. N. Goverdovskiy, and A. I. Temnikov, "Design of springs with "negative" stiffness to improve vehicle driver vibration isolation," *Journal of Sound and Vibration*, vol. 302, no. 4-5, pp. 865–874, 2007.

[70] A. Abolfathi, *Nonlinear vibration isolators with asymmetric stiffness*. PhD thesis, University of Southampton, 2012.

[71] B. Gramüller, J. Boblenz, and C. Hühne, "Pacs—realization of an adaptive concept using pressure actuated cellular structures," *Smart Materials and Structures*, vol. 23, no. 11, p. 115006, 2014.

[72] E. T. Filipov, T. Tachi, and G. H. Paulino, "Origami tubes assembled into stiff, yet reconfigurable structures and metamaterials," *Proceedings of the National Academy of Sciences*, vol. 112, pp. 12321–12326, 10 2015. 15.

[73] A. Carrella, M. J. Brennan, T. P. Waters, and V. Lopes, “Force and displacement transmissibility of a nonlinear isolator with high-static-low-dynamic-stiffness,” *International Journal of Mechanical Sciences*, vol. 55, no. 1, pp. 22–29, 2012.

[74] A. Carrella, M. J. Brennan, I. Kovacic, and T. P. Waters, “On the force transmissibility of a vibration isolator with quasi-zero-stiffness,” *Journal of Sound and Vibration*, vol. 322, no. 4-5, pp. 707–717, 2009.

[75] A. Carrella, M. I. Friswell, A. Zotov, D. J. Ewins, and A. Tichonov, “Using nonlinear springs to reduce the whirling of a rotating shaft,” *Mechanical Systems and Signal Processing*, vol. 23, no. 7, pp. 2228–2235, 2009.

[76] J. Zhou, X. Wang, D. Xu, and S. Bishop, “Nonlinear dynamic characteristics of a quasi-zero stiffness vibration isolator with cam-roller-spring mechanisms,” *Journal of Sound and Vibration*, vol. 346, no. 1, pp. 53–69, 2015.

[77] S. A. Neild and D. J. Wagg, “Applying the method of normal forms to second-order nonlinear vibration problems,” *Proceedings of The Royal Society*, vol. 467, no. October 2010, pp. 1141–1163, 2011.

[78] A. D. Shaw, S. A. Neild, and D. J. Wagg, “Dynamic analysis of high static low dynamic stiffness vibration isolation mounts,” *Journal of Sound and Vibration*, vol. 332, no. 6, pp. 1437–1455, 2013.

[79] M. Hamdan and T. Burton, “On the steady state response and stability of non-linear oscillators using harmonic balance,” *Journal of Sound and Vibration*, vol. 166, no. 2, pp. 255–266, 1993.

[80] A. Nayfeh, *Introduction to Perturbation Techniques*. Wiley. New York, 1993.

[81] M. H. Raibert, *Legged robots that balance*. MIT Press, 1986.

[82] P. Aerts, “Vertical jumping in galago senegalensis: the quest for an obligate mechanical power amplifier,” *Philosophical Transactions of the Royal Society B: Biological Sciences*, vol. 353, no. 1375, pp. 1607–1620, 1998.

[83] T. J. Roberts, “Probing the limits to muscle-powered accelerations: lessons from jumping bullfrogs,” *Journal of Experimental Biology*, vol. 206, no. 15, pp. 2567–2580, 2003.

[84] A. Sayyad, B. Seth, and P. Seshu, “Single-legged hopping robotics research - a review,” *Robotica*, vol. 25, no. 5, pp. 587–613, 2007.

[85] S. E. Bergbreiter, “Autonomous jumping microrobots,” *ProQuest Dissertations and Theses*, vol. 3306062, p. 150, 2007.

[86] D. W. Haldane, M. M. Plecnik, J. K. Yim, and R. S. Fearing, “Robotic vertical jumping agility via series-elastic power modulation,” *Science Robotics*, vol. 1, no. 1, p. eaag2048, 2016.

[87] D. W. Haldane, M. Plecnik, J. K. Yim, and R. S. Fearing, “A power modulating leg mechanism for monopedal hopping,” *IEEE International Conference on Intelligent Robots and Systems*, vol. 2016-Novem, pp. 4757–4764, 2016.

[88] M. H. Raibert, H. B. Brown, and M. Chepponis, “Experiments in balance with a 3d one-legged hopping machine,” *The International Journal of Robotics Research*, vol. 3, pp. 75–92, 6 1984.

[89] J. Zhao, J. Xu, B. Gao, N. Xi, F. J. Cintron, M. W. Mutka, and L. Xiao, “Msu jumper: A single-motor-actuated miniature steerable jumping robot,” *IEEE Transactions on Robotics*, vol. 29, no. 3, pp. 602–614, 2013.

[90] J. Albro and J. Bobrow, “Optimal motion primitives for a 5 dof experimental hopper,” *Robotics and Automation, 2001. ...*, pp. 3630–3635, 2001.

[91] D. E. Koditschek and M. Bühler, “Analysis of a simplified hopping robot,” *The International Journal of Robotics Research*, vol. 10, no. 6, pp. 587–605, 1991.

[92] K. D. Maier, “Neural network based control of legged hopping systems,” in *Proceeding of the 2001 IEEE International Symposium on Intelligent Control (ISIC'01)(Cat. No. 01CH37206)*, pp. 115–120, IEEE, 2001.

[93] A. Schammass, G. A. P. Caurin, and C. M. O. Valente, “Control of a one-legged robot with energy savings,” *Journal of the Brazilian Society of Mechanical Sciences*, vol. 23, no. 1, pp. 41–48, 2001.

[94] K. Matsuoka, “A model of repetitive hopping movements in man,” *Proceedings of Fifth World Congress on Theory of Machines and Mechanisms*, p. 1168–1171, 1979.

[95] W. Lee and M. Raibert, “Control of hoof rolling in an articulated leg,” *Proceedings. 1991 IEEE International Conference on Robotics and Automation*, pp. 1386–1391, 1991.

[96] H. Tsukagoshi, M. Sasaki, A. Kitagawa, and T. Tanaka, “Design of a higher jumping rescue robot with the optimized pneumatic drive,” *Proceedings - IEEE International Conference on Robotics and Automation*, vol. 2005, no. April, pp. 1276–1283, 2005.

[97] D. H. Kim, J. H. Lee, I. Kim, S. H. Noh, and S. K. Oho, “Mechanism, control, and visual management of a jumping robot,” *Mechatronics*, vol. 18, no. 10, pp. 591–600, 2008.

[98] S. Dubowsky, S. Kesner, J. Plante, and P. Boston, "Hopping mobility concept for search and rescue robots," *Industrial Robot: An International Journal*, vol. 35, no. 3, pp. 238–245, 2008.

[99] S. Kesner, J. Plante, S. Dubowsky, and P. Boston, "a hopping mobility concept for a rough terrain search and rescue robot," *Advances in Climbing and Walking Robots, Proceedings*, pp. 271–280, 2007.

[100] R. Armour, K. Paskins, A. Bowyer, J. Vincent, and W. Megill, "Jumping robots: A biomimetic solution to locomotion across rough terrain," *Bioinspiration and Biomimetics*, vol. 2, no. 3, 2007.

[101] A. Yamada, H. Mameda, H. Mochiyama, and H. Fujimoto, "A compact jumping robot utilizing snap-through buckling with bend and twist," *IEEE/RSJ 2010 International Conference on Intelligent Robots and Systems, IROS 2010 - Conference Proceedings*, pp. 389–394, 2010.

[102] A. Yamada, M. Watari, H. Mochiyama, and H. Fujimoto, "An asymmetric robotic catapult based on the closed elastica for jumping robot," *2008 IEEE International Conference on Robotics and Automation*, pp. 232–237, 2008.

[103] R. T. M'Closkey and J. W. Burdick, "Periodic motions of a hopping robot with vertical and forward motion," *The International Journal of Robotics Research*, vol. 12, pp. 197–218, 6 1993.

[104] P. Fiorini and J. Burdick, "The development of hopping capabilities for small robots," *Autonomous Robots*, vol. 14, no. 2-3, pp. 239–254, 2003.

[105] S. Sadeghi and S. Li, "Fluidic origami cellular structure with asymmetric quasi-zero stiffness for low-frequency vibration isolation," *Smart Materials and Structures*, vol. 28, p. 065006, 2019.

[106] R. Bogue, "Robots in the nuclear industry: A review of technologies and applications," *Industrial Robot*, vol. 38, no. 2, pp. 113–118, 2011.

[107] P. Y. Chua, T. Ilschner, and D. G. Caldwell, "Robotic manipulation of food products - a review," *Industrial Robot*, vol. 30, no. 4, pp. 345–354, 2003.

[108] A. Shukla and H. Karki, "Application of robotics in onshore oil and gas industry-a review part i," *Robotics and Autonomous Systems*, vol. 75, pp. 490–507, 2016.

[109] A. H. Reddy, B. Kalyan, and C. S. Murthy, "Mine rescue robot system – a review," *Procedia Earth and Planetary Science*, vol. 11, pp. 457–462, 2015.

[110] T. Belpaeme, J. Kennedy, A. Ramachandran, B. Scassellati, and F. Tanaka, "Social robots for education: A review," *Science Robotics*, vol. 3, no. 21, p. eaat5954, 2018.

[111] F. B. V. Benitti, "Exploring the educational potential of robotics in schools: A systematic review," *Computers and Education*, vol. 58, no. 3, pp. 978–988, 2012.

[112] P. K. Jamwal, S. Hussain, and S. Q. Xie, "Review on design and control aspects of ankle rehabilitation robots," *Disability and Rehabilitation: Assistive Technology*, vol. 10, no. 2, pp. 93–101, 2015.

[113] H. Robinson, B. MacDonald, and E. Broadbent, "The role of healthcare robots for older people at home: A review," *International Journal of Social Robotics*, vol. 6, no. 4, pp. 575–591, 2014.

[114] J. Liu, M. Tan, and X. Zhao, "Legged robots — an overview," *Transactions of the Institute of Measurement Control*, vol. 29, no. 2, pp. 185–202, 2007.

[115] H. Zhuang, H. Gao, Z. Deng, L. Ding, and Z. Liu, "A review of heavy-duty legged robots," *Science China Technological Sciences*, vol. 57, no. 2, pp. 298–314, 2014.

[116] S. Dubey, M. Prateek, and M. Saxena, "Robot locomotion – a review," *International Journal of Applied Engineering Research*, vol. 10, no. 3, pp. 7357–7369, 2015.

[117] S. Sadeghi, B. D. Betsill, P. Tallapragada, and S. Li, "The effect of nonlinear springs in jumping mechanisms," in *ASME 2018 Dynamic Systems and Control Conference*, American Society of Mechanical Engineers Digital Collection, 2018.

[118] U. Scarfogliero, C. Stefanini, and P. Dario, "The use of compliant joints and elastic energy storage in bio-inspired legged robots," *Mechanism and Machine Theory*, vol. 44, no. 3, pp. 580–590, 2009.

[119] J. Zhang, G. Song, G. Qiao, T. Meng, and H. Sun, "An indoor security system with a jumping robot as the surveillance terminal," *IEEE Transactions on Consumer Electronics*, vol. 57, no. 4, pp. 1774–1781, 2011.

[120] J. Zhao, N. Xi, B. Gao, M. W. Mutka, and L. Xiao, "Design and testing of a controllable miniature jumping robot," *IEEE/RSJ 2010 International Conference on Intelligent Robots and Systems, IROS 2010 - Conference Proceedings*, no. November, pp. 3346–3351, 2010.

[121] M. Johnson, Y. Chen, S. Hovet, S. Xu, B. Wood, H. Ren, J. Tokuda, and Z. T. H. Tse, "Fabricating biomedical origami: a state-of-the-art review," *International Journal of Computer Assisted Radiology and Surgery*, 2017.

[122] P. Wang, T. A. Meyer, V. Pan, P. K. Dutta, and Y. Ke, "The beauty and utility of dna origami," *Chem*, vol. 2, pp. 359–382, 3 2017.

[123] S. Sadeghi and S. Li, "Fluidic origami cellular structure with asymmetric quasi-zero stiffness for low-frequency vibration isolation," *Smart Materials and Structures*, vol. 28, p. 065006, 6 2019.

[124] S. Sadeghi and S. Li, "Analyzing the bi-directional dynamic morphing of a bi-stable water-bomb base origami," in *Behavior and Mechanics of Multifunctional Materials XIII*, vol. 10968, p. 109680S, International Society for Optics and Photonics, 2019.

[125] K. Liu and G. H. Paulino, "Nonlinear mechanics of non-rigid origami: an efficient computational approach," *Proceedings of the Royal Society A: Mathematical, Physical and Engineering Science*, vol. 473, p. 20170348, 10 2017.

[126] S. Li, H. Fang, S. Sadeghi, P. Bhovad, and K.-W. Wang, "Architected Origami Materials: How Folding Creates Sophisticated Mechanical Properties," *Advanced Materials*, vol. 31, p. 1805282, 2019.

[127] M. Schenk, A. D. Viquerat, K. A. Seffen, and S. D. Guest, "Review of inflatable booms for deployable space structures: packing and rigidization," *Journal of Spacecraft and Rockets*, vol. 51, pp. 762–778, 2014.

[128] Y. Chen, R. Peng, and Z. You, "Origami of thick panels," *Science*, vol. 349, pp. 396–400, 2015.

[129] M. Johnson, Y. Chen, S. Hovet, S. Xu, B. Wood, H. Ren, J. Tokuda, and Z. T. H. Tse, "Fabricating biomedical origami: a state-of-the-art review," *International Journal of Computer Assisted Radiology and Surgery*, 2017.

[130] M. Schenk and S. D. Guest, "Geometry of Miura-folded metamaterials," *Proceedings of the National Academy of Sciences*, vol. 110, pp. 3276–3281, 2013.

[131] H. Fang, S. Li, and K. W. Wang, "Self-locking degree-4 vertex origami structures," *Proceedings of the Royal Society A: Mathematical, Physical and Engineering Science*, vol. 472, p. 20160682, 2016.

[132] S. Cranford, D. Sen, and M. J. Buehler, "Meso-origami: Folding multilayer graphene sheets," *Applied Physics Letters*, vol. 95, pp. 1–4, 2009.

[133] A. Crivaro, R. Sheridan, M. Frecker, T. W. Simpson, and P. Von Lockette, "Bistable compliant mechanism using magneto active elastomer actuation," *Journal of Intelligent Material Systems and Structures*, vol. 27, pp. 2049–2061, 2016.

[134] M. T. Tolley, S. M. Felton, S. Miyashita, D. Aukes, D. Rus, and R. J. Wood, "Self-folding origami: Shape memory composites activated by uniform heating," *Smart Materials and Structures*, vol. 23, 2014.

[135] S. Miyashita, S. Guitron, M. Ludersdorfer, C. R. Sung, and D. Rus, "An untethered miniature origami robot that self-folds, walks, swims, and degrades," *Proceedings - IEEE International Conference on Robotics and Automation*, vol. 2015-June, pp. 1490–1496, 2015.

[136] H. Okuzaki, T. Kuwabara, K. Funasaka, and T. Saido, "Humidity-sensitive polypyrrole films for electro-active polymer actuators," *Advanced Functional Materials*, vol. 23, pp. 4400–4407, 2013.

[137] S. Ahmed, Z. Ounaies, and M. Frecker, "Investigating the performance and properties of dielectric elastomer actuators as a potential means to actuate origami structures," *Smart Materials and Structures*, vol. 23, 2014.

[138] E. Peraza-Hernandez, D. Hartl, and R. Malak, "Simulation-Based Design of a Self-Folding Smart Material System," in *Volume 6B: 37th Mechanisms and Robotics Conference*, p. V06BT07A045, ASME, 2013.

[139] B. H. Hanna, J. M. Lund, R. J. Lang, S. P. Magleby, and L. L. Howell, "Waterbomb base: a symmetric single-vertex bistable origami mechanism," *Smart Materials and Structures*, vol. 23, p. 094009, 2014.

[140] L. Bowen, K. Springsteen, H. Feldstein, M. Frecker, T. W. Simpson, and P. von Lockette, "Development and Validation of a Dynamic Model of Magneto-Active Elastomer Actuation of the Origami Waterbomb Base," *Journal of Mechanisms and Robotics*, vol. 7, p. 011010, 2015.

[141] R. L. Harne and K. Wang, *Harnessing bisatble structural dynamics: for vibration control, energy harvesting and sensing.* John Wiley & Sons., 2017.

[142] N. Nadkarni, C. Daraio, and D. M. Kochmann, "Dynamics of periodic mechanical structures containing bistable elastic elements: From elastic to solitary wave propagation," *Physical Review E - Statistical, Nonlinear, and Soft Matter Physics*, vol. 90, pp. 1–13, 2014.

[143] R. L. Harne and K. W. Wang, "A review of the recent research on vibration energy harvesting via bistable systems," *Smart Materials and Structures*, vol. 22, 2013.

[144] R. L. Harne and K. W. Wang, "A bifurcation-based coupled linear-bistable system for microscale mass sensing," *Journal of Sound and Vibration*, vol. 333, pp. 2241–2252, 2014.

[145] A. F. Arrieta, O. Bilgen, M. I. Friswell, and P. Hagedorn, "Dynamic control for morphing of bi-stable composites," *Journal of Intelligent Material Systems and Structures*, vol. 24, pp. 266–273, 2013.

[146] A. Senba, T. Ikeda, and T. Ueda, "A two-way morphing actuation of bi-stable composites with piezoelectric fibers," *51st AIAA/ASME/ASCE/AHS/ASC Structures, Structural Dynamics, and Materials Conference*, 2013.

[147] S. Sadeghi and S. Li, "Analyzing the bi-directional dynamic morphing of a bi-stable water-bomb base origami," in *Behavior and Mechanics of Multifunctional Materials XIII* (H. E. Naguib, ed.), vol. 10968, pp. 198 – 208, International Society for Optics and Photonics, SPIE, 2019.

[148] S. Sadeghi and S. Li, "Dynamic morphing of a bi-stable water-bomb base origami using an active control strategy (conference presentation)," in *Behavior and Mechanics of Multifunctional Materials IX*, vol. 11377, p. 1137706, International Society for Optics and Photonics, 2020.

[149] H. Fang, K. W. Wang, and S. Li, "Asymmetric energy barrier and mechanical diode effect from folding multi-stable stacked-origami," *Extreme Mechanics Letters*, vol. 17, pp. 7–14, 2017.

[150] C. Jianguo, D. Xiaowei, Z. Ya, F. Jian, T. Yongming, J. Cai, X. Deng, Z. Ya, F. Jiang, and Y. Tu, "Bistable behavior of the cylindrical origami structure with Kresling pattern," *Journal of Mechanical Design*, vol. 137, p. 061406, 2015.

[151] H. Yasuda, Z. Chen, and J. Yang, "Multitransformable leaf-out origami with bistable behavior," *Journal of Mechanisms and Robotics*, vol. 8, p. 031013, 2016.

[152] J. L. Silverberg, J.-H. Na, A. A. Evans, B. Liu, T. C. Hull, C. D. Santangelo, R. J. Lang, R. C. Hayward, and I. Cohen, "Origami structures with a critical transition to bistability arising from hidden degrees of freedom," *Nature materials*, vol. 14, no. 4, pp. 389–393, 2015.

[153] D. Rus and M. T. Tolley, "Design, fabrication and control of origami robots," *Nature Reviews Materials*, vol. 3, no. 6, pp. 101–112, 2018.

[154] A. O'Halloran, F. O'malley, and P. McHugh, "A review on dielectric elastomer actuators, technology, applications, and challenges," *Journal of Applied Physics*, vol. 104, no. 7, p. 9, 2008.

[155] H. Jaeger, "The "echo state" approach to analysing and training recurrent neural networks-with an erratum note," *Bonn, Germany: German National Research Center for Information Technology GMD Technical Report*, vol. 148, no. 34, p. 13, 2001.

[156] W. Maass, T. Natschläger, and H. Markram, "Real-time computing without stable states: A new framework for neural computation based on perturbations," *Neural computation*, vol. 14, no. 11, pp. 2531–2560, 2002.

[157] G. Tanaka, T. Yamane, J. B. Héroux, R. Nakane, N. Kanazawa, S. Takeda, H. Numata, D. Nakano, and A. Hirose, "Recent advances in physical reservoir computing: A review," *Neural Networks*, vol. 115, pp. 100–123, 2019.

[158] M. Lukoševičius and H. Jaeger, "Reservoir computing approaches to recurrent neural network training," *Computer Science Review*, vol. 3, no. 3, pp. 127–149, 2009.

[159] B. Schrauwen, D. Verstraeten, and J. Van Campenhout, "An overview of reservoir computing: theory, applications and implementations," in *Proceedings of the 15th european symposium on artificial neural networks. p. 471-482 2007*, pp. 471–482, 2007.

[160] H. Jaeger, *Tutorial on training recurrent neural networks, covering BPPT, RTRL, EKF and the" echo state network" approach*, vol. 5. GMD-Forschungszentrum Informationstechnik Bonn, 2002.

[161] H. Hauser, A. J. Ijspeert, R. M. Füchslin, R. Pfeifer, and W. Maass, "Towards a theoretical foundation for morphological computation with compliant bodies," *Biological cybernetics*, vol. 105, no. 5-6, pp. 355–370, 2011.

[162] H. Hauser, A. J. Ijspeert, R. M. Füchslin, R. Pfeifer, and W. Maass, "The role of feedback in morphological computation with compliant bodies," *Biological cybernetics*, vol. 106, no. 10, pp. 595–613, 2012.

[163] J. Kuwabara, K. Nakajima, R. Kang, D. T. Branson, E. Guglielmino, D. G. Caldwell, and R. Pfeifer, "Timing-based control via echo state network for soft robotic arm," in *The 2012 International Joint Conference on Neural Networks (IJCNN)*, pp. 1–8, IEEE, 2012.

[164] T. Li, K. Nakajima, M. Cianchetti, C. Laschi, and R. Pfeifer, "Behavior switching using reservoir computing for a soft robotic arm," in *2012 IEEE International Conference on Robotics and Automation*, pp. 4918–4924, IEEE, 2012.

[165] K. Nakajima, H. Hauser, T. Li, and R. Pfeifer, "Information processing via physical soft body," *Scientific reports*, vol. 5, p. 10487, 2015.

[166] K. Nakajima, T. Li, H. Hauser, and R. Pfeifer, "Exploiting short-term memory in soft body dynamics as a computational resource," *Journal of The Royal Society Interface*, vol. 11, no. 100, p. 20140437, 2014.

[167] P. Bhovad and S. Li, "Physical reservoir computing with origami and its application to robotic crawling," *arXiv preprint arXiv:2101.08348*, 2021.

[168] R. Legenstein and W. Maass, "What makes a dynamical system computationally powerful," *New directions in statistical signal processing: From systems to brain*, pp. 127–154, 2007.

[169] K. Caluwaerts and B. Schrauwen, "The body as a reservoir: locomotion and sensing with linear feedback," in *2nd International conference on Morphological Computation (ICMC 2011)*, 2011.